



**Design of a Non-Invasive Device to Measure Bone Strength
Recovery of Distal Radius Fractures for Use with HR-pQCT
Imaging**

A Major Qualifying Project

Submitted to the Faculty of the

WORCESTER POLYTECHNIC INSTITUTE

in partial fulfillment of the requirements

for the degree of

Bachelors of Science in:

Biomedical or Mechanical Engineering

Report Submitted To:

Faculty Advisor, Professor Karen Troy, Ph.D

By

Jennifer Golden, Ahmed Hakim, Hannah Sattler

April 27, 2017

Abstract

Distal radius fractures, specifically Colles' fractures are the most common bone injury in adults, with the majority occurring in postmenopausal women. Often these fractures result in painful healing defects including non-union and delayed union, leading to extended treatment and even surgery. Currently, there is no clinical method to quantify the extent of bone healing beyond the limited capabilities of standard x-rays. The goal of this project is to develop a device which can determine the strength of the healing fracture for both clinical and research applications. This is achieved by applying a known bending load to the distal radius and measuring the displacement of the bone in HR-pQCT images. The elastic modulus of the callus material can then be calculated and correlated to a stage of bone healing. The device created was manufactured via 3D printing with carbon fiber reinforced Onyx (nylon). Validation of device performance was performed using cadaver wrists models.

Acknowledgements

We would like to thank the following individuals and organizations that helped make this project successful:

- Professor Karen Troy and Professor Ara Nazarian for their continued support and guidance throughout this project
- Joshua Johnson and Megan Mancuso for their technical support in the CT imaging lab
- Stephen Okajima for his help in 3D printing the device
- Lisa Wall for her help in coordinating MQP projects and designating usable laboratory space for the team.

Authorship

The authors performed work in their areas of expertise and cross-functionally as needed. Primary contributions of each member are outlined below.

Topics	Primary Contributors
Research	All
Documentation	All
Assembly	All
Test Execution	All
Engineering Design Process	All
Administrative	Ahmed Hakim
Deflection Modeling	Jennifer Golden
CAD Modeling	Jennifer Golden
Materials Reduction	Jennifer Golden
Test Development	Jennifer Golden, Hannah Sattler
Engineering Calculations	Hannah Sattler
CAM/Manufacturing	Hannah Sattler
HR-pQCT Imaging & Processing	Hannah Sattler
Instrumentation	Hannah Sattler

Contents

Chapter 1 : Introduction.....	1
Chapter 2 : Background and Literature Review.....	5
2.1 Distal Radius Fractures	5
2.1.1 Classification of Distal Radius Fractures	5
2.1.2 Colles' Fractures	6
2.1.3 Smith's Fractures	7
2.1.4 Complex Distal Radius Fractures	8
2.2 Fracture Healing.....	10
2.2.1 Biology of Fracture Healing	10
2.2.2 Mechanical Properties of Healing Fractures	11
2.2.3 Distraction osteogenesis	12
2.2.4 Frequency and population for this project.....	13
2.3 Fracture Treatment.....	14
2.3.2 Fracture Healing Complications	14
2.4 Imaging Techniques	17
2.4.2 Mechanical Considerations in Loading-Response Distal Radius Imaging.....	19
2.5 Loading Devices for Imaging Technologies	20
2.5.1 Similar Devices	20
Chapter 3 : Project Strategy.....	23
3.1 Client Statement.....	23
3.1.1 Initial Client Statement	23
3.2 Client Statement Development	23
3.2.1 Need Statement	24
3.2.2 Stakeholder Analysis.....	24
3.3 Client Statement Revisions.....	25
3.3.1 Revised Client Statement.....	26
3.4 Project Objectives.....	26
3.5 Project Constraints	27
3.6 Project Approach.....	28
Chapter 4 : Alternative Designs.....	29

4.1 Needs Analysis.....	29
4.2 Function Specifications.....	30
4.3 Conceptual Designs	31
4.3.1 Determining the optimal loading type(s)	32
4.3.2 Overview of Loading Mechanisms for the Tensile Device.....	33
4.3.3 Design evaluation for tension design.....	36
4.3.4 Grasping considerations.....	39
4.3.5 Hand grasping methods	40
4.3.6 Hand grasping component design evaluation.....	41
4.3.7 Elbow grasping component design evaluation.....	43
4.3.8 Initial Tensile Design	44
4.3.9 Updated Tension Design.....	48
4.3.10 Previous Iteration of Project, Side-Application Bending Design	50
4.3.11 Design evaluation for the bending design.....	52
4.3.13 Optimizing the Configuration of the Bending Design	61
4.3.14 Evaluating Devices to Measure the Applied Force	69
4.4 Design Calculations.....	73
4.4.5 Bending Design Force-Displacement Calculations	77
4.5 Design Conclusions.....	78
4.5.1 Material Selection.....	79
4.5.2 Manufacturing Technique Selection	82
4.6 Optimization	83
4.6.1 Drive Mechanism Resolution Improvement.....	84
Chapter 5 : Design Verification.....	86
5.1 Experimental Testing Phase.....	86
5.2 Testing Procedures for the Hand and Elbow Gripping Mechanisms.....	88
5.2.1 Testing procedure for the hand	88
5.2.2 Testing Data for the hand.....	90
5.2.3 Testing Procedure for the Elbow Mechanisms	93
5.2.4 Testing Data for the Elbow Mechanisms	94
5.3 Validating the Load Cell Circuit.....	97
5.4 Load Cell Calibration	99
5.4.1 Loading Mechanism Testing.....	102

5.5 Field of View (FOV) and Scanning Size Validation	106
5.6 Device Ergonomics Testing	109
5.7 Avian Bone Imaging Validation Testing	109
5.8 Third Quarter Design Changes	111
Bending portion for testing production	111
5.9 Pressure Testing	112
5.10 Pressure Point Comfort Testing	113
5.11 Instrumentation	114
Chapter 6 : Design Verification – Discussion	115
Economics	115
Environmental impact	116
Societal Impact	116
Political Ramifications	117
Ethical concern	117
Health and safety issues	118
Manufacturability	119
Sustainability	120
Chapter 7 : Final Design and Validation	121
7.1 Overview of Final Design	121
7.2 Device Manufacturing	127
7.3 Device Operation	128
7.4 Future Recommendations to Improve the Design	129
7.5 Design Validation	129
Chapter 8 Conclusion and Recommendations	133
Citations	135
Appendix	139

Figures

Figure 2-1 X-ray image of a normal bone and a broken distal radius [12].....	6
Figure 2-2 Colles' Fracture [14].....	7
Figure 2-3 Smith's Fracture [12].....	7
Figure 2-4 Osteochondral Fracture [16]	8
Figure 2-5 Compression Fracture of the Distal Radius [17].....	9
Figure 2-6 Fracture Dislocation of the Distal Radius [18].....	9
Figure 2-7 Complex Fracture of the Distal Radius [19].....	10
Figure 2-8 Stages of fracture repair [21].....	11
Figure 2-9 A torque-angle graph of six bones representative of the entire healing period. The numbers on the graph indicate days of healing time. As the healing progresses, there is an increase in the strength of union shown by changes in the torque-angle graphs.	12
Figure 2-10 Hypertrophic non-union [20].....	16
Figure 2-11 Image of a CT beam and a patient in a CT Imaging System [27]	18
Figure 2-12 Device that can apply a mechanical load during imaging [30]	21
Figure 4-1 Product function flowchart that outlines how the device will be used.	31
Figure 4-2 Schematic that depicts how a worm screw works [39].....	33
Figure 4-3 Image of a screw drive [48].....	34
Figure 4-4 Components of a Rack and Pinion device [40].....	34
Figure 4-5 The two types of springs: a coil spring (on the left) and wave spring (on the right) [42]	35
Figure 4-6 Schematic of how a pulley is able to generate a force [43].....	36
Figure 4-7 Image of the hook and loop finger brace developed with the foam padding, plastic supports, and hook and loop tape labeled.....	40
Figure 4-8 Image of an elbow brace that we purchased for testing.....	43
Figure 4-9 Sequence of steps followed in developing the bony contacts.....	44
Figure 4-10 Isometric View of the Initial Tensile Loading Design with the Majorred Parts Numbered	45
Figure 4-11 Top and Isometric Views of the Base (Numbered as 1) and worm screw (Numbered as 2) of the Tensile Loading Design.....	46
Figure 4-12 Isometric View of the Hand Peg of the Tensile Loading Design	46
Figure 4-13 Isometric and front 2D view of the Elbow Support.....	47
Figure 4-14 Image of the prototype for the tensile design that we built via 3D printing.	47
Figure 4-15 Schematic of a screw drive mechanism.	48
Figure 4-16 CAD model of the tension design with the major components labeled	48
Figure 4-17 Updated tension design prototype fabricated out of wood with the components labeled	49
Figure 4-18 Updated tension design including the gripping mechanisms	50
Figure 4-19 Previously completed design utilizing bending with the major parts labeled	50
Figure 4-20 Bending design that will utilize a lever.....	53
Figure 4-21 Schematic of a Class I Lever that can be used in the bending design [46].....	53
Figure 4-22 Side view image of the bending design that will apply a load from above the point of application. In this image, the patient's right hand is facing down.....	54

Figure 4-23 Drawing and schematic of the screw drive design to apply a bending force with the distal radius and screw drive labeled.....	54
Figure 4-24 Various views of the round bending design with single drive screw.....	58
Figure 4-25 CAD Model of the Updated Bending Design with the major components labeled ...	59
Figure 4-26 Pressure point piece of bending design to apply force to the wrist in a focused and repeatable location.....	60
Figure 4-27 Bending Design Prototype with the components labeled.....	61
Figure 4-28 (a) Map of the stresses that occur in the base of the model (b) Map of the displacements that occur in the base of the model.....	62
Figure 4-29 (a) Map of the stresses that occur in the pressure point piece (b) Map of the displacements that occur in the pressure point piece	63
Figure 4-30 (a) The left image shows a pressure point with a full round surface. (b) The right image point that has a chamfered tapering	64
Figure 4-31 Image of pressure point with dimensions labeled. PL represents the pressure point length and ML represents the styloid process marker length.....	64
Figure 4-32 CAD models of material reductions in the force application piece.	66
Figure 4-33 Image depicting the length of a cellular solid to thickness of the material in between cells	68
Figure 4-34 Schematic of a digital strain gauge [47].....	69
Figure 4-35 Piezo resistive Force Sensor [49].....	70
Figure 4-36 Image of a beam load cell. [51]	71
Figure 4-37 Image of the radius of bone and soft tissue.....	74
Figure 4-38 Bearing ratio of a sliding mechanism.....	84
Figure 5-1 Image showing how hook and loop is applied to the hand.....	89
Figure 5-2 Image showing how hook and loop is applied to the hand.....	90
Figure 5-3 Image showing how hook and loop is applied to the hand.....	90
Figure 5-4 Image of the Athletic Tape Finger Brace taken during testing with the components labeled	91
Figure 5-5 Schematic and image for testing the elbow gripping mechanisms.....	93
Figure 5-6 Experimental images for testing the A) Elbow Brace, B) Blood Pressure Cuff, and C) Bony Contact Brace	95
Figure 5-7 Circuit block diagram for load cell data acquisition.	97
Figure 5-8 Image of the circuit with each component (including the Arduino Circuit Board, Strain Gauge Unit, and Load Cell) labeled	98
Figure 5-9 Image that depicts how the load cell is placed on the Instron Testing Machine	100
Figure 5-10 Graph that depicts the line of best fit and the coefficient of determination for the Average Voltage (in volts) and the Applied Load (in pounds) for Trial 1.	101
Figure 5-11 Calibration of the Phidgets model 3137 button load cell for Trial 1	102
Figure 5-12 Image of the force application piece with the signal amplifying and conditioning unit and Arduino board	103
Figure 5-13 Image of the force application piece on the table	103
Figure 5-14 Graph of the Average Force Generated vs. the Linear Distance traveled downward for the force application piece	104

Figure 5-15 Graph of the Average Force Generated vs. the number of degrees each rod is turned for the force application piece	105
Figure 5-16 Line of best fit for applied force vs. screw setting in the button load cell	106
Figure 5-17 Image that displays specifications of the scanner including imaging resolution and max scan size	107
Figure 5-18 Image that depicts the scale bar the team set	107
Figure 5-19 Image that displays the diameter that we measured	108
Figure 5-20 Image that displays the height that was measured	108
Figure 5-21 Loading region model sliced for prototyping (left) and prototype with load cell (right).	111
Figure 5-22 Graph of Comfort Testing results comparing various pressure point designs	113
Figure 7.1 (a) Top image displaying the front plane view of the device. (b) Bottom image displaying the right view.	122
Figure 7.1 (c) device with the major parts numbered.....	123
Figure 7.8 Graph displaying the applied force per degree turned	130
Figure 7-9 Validation testing using avian specimens	130
Figure 7-10 (a) shows the specimen loaded in the device (b) shows the device loaded into the CT scanner	131
Figure 7-11 (a) shows the specimen loaded in the device (b) shows the device loaded into the CT scanner	132

Chapter 1 : Introduction

Distal radius fractures are the most common bone fracture, accounting for 8-15% of all bone injuries to adults [1]. The radius is the larger of the two long bones in the forearm and is lateral when in the anatomical position. These fractures typically occur on the distal end of the long bone, 1 to 2 inches proximal of the radiocarpal joint [2]. The most common type of distal radius fracture is the Colles' fracture; this is a transverse fracture of the metaphyseal region of the radius occurring 25 to 40 mm away from the radiocarpal joint [3]. These fractures are caused by impact when the hand is in dorsiflexion and exhibit "characteristic dorsal tilt, dorsal shift, radial tilt, radial shift, supination and impaction" [4]. 70% of Colles' fractures occur in postmenopausal women. These individuals are prone to fragility fractures from forward falls due to both a lowered bone density caused by lower estrogen levels and decreased balance. Because of the lowered bone density, the low energy impact of falling forward onto an outstretched palm from standing (to break the fall with the hand) applies sufficient force to yield the bone and cause fracture. The less common sister fracture to the Colles' fracture is the Smith fracture which occurs when the individual falls backwards onto the wrist in dorsiflexion and there is palmar tilt of the distal fragment [5].

While this fracture can also occur in men, it is most prevalent in women; Caucasian females aged 45 – 50 have a 15-30% lifetime chance of having a Colles' fracture compared to a 2-3% lifetime chance of having Colles' fracture in males [6]. The second most common instigation of Colles' fractures is by a high-energy impact with the wrist in dorsiflexion, which is common in younger individuals; these fractures are typically found to be sports-related injuries. Furthermore, treating distal radius fractures accounts for a significant medical cost. In the pediatric population alone, the cost of treating distal radius fractures has been cited to be in upwards of \$2 billion per year [7]. There are also other personal and societal costs, including temporary disability, lost time from work, and costs for prescription drugs.

The most common treatment method for the Colles' fracture is through the application of a plaster or fiberglass cast, which is worn for a relatively short period of 4-8 weeks. Unstable, complete fractures often require surgeries and the use of more advanced internal or external fixation devices, including pins and plates. Currently, no technology exists which allows physicians to analyze how a fracture is healing during the casted period. Bone healing time is typically 6-8 weeks in a healthy individual [8]. Due to a physician's inability to determine extent of healing, casts are often removed prematurely when the bone has not been fully healed (known

as delayed union) leading to pain and risk of fracture re-injury and healing complications. Alternatively, an improperly or incompletely healed bone may be discovered when there is continuing pain after removal of the cast; both delayed and improper healing can result in further treatment up to and including surgery to correct the healing defect.

Another major healing defect is non-union, which typically occurs with wide separation between bone ends and happens in one of two ways. Hypertrophic non-union results in the space between the bone ends being filled with cartilage and fibrous tissue. Alternatively, atrophic non-union results in the bone ends being rounded and reabsorbed with no attempt at healing occurring [9]. In unstable fractures, a bone fragment may also become displaced leading to incorrect or incomplete alignment during healing.

This project aims to help detect healing defects earlier and to prevent premature cast removal in patients with distal radius fractures. This will be accomplished through the design and manufacture of a device, which applies a known mechanical load to the fracture to produce a small displacement. The displacement will allow the healing process to be seen on a CT scan, something that is not possible in an unloaded bone. Bone strain can then be measured and correlated to a stage of the healing process through standard elastic displacement models commonly used in materials engineering applications. Bone strain will also enable the measurement of strength recovery in the fracture callus. By creating the first measurement tool for bone strength recovery, the device will also aid in early detection of healing defects, and the testing and development of fracture healing therapies. In summary, the device will allow doctors to know how much a bone has healed, if it is healing properly, when the bone has finished healing, and to decide on further treatment for the patient if necessary. Furthermore, the project is to be completed under the guidance of Primary Advisor Karen Troy, Ph.D. and in conjunction with Ara Nazarian, Ph.D., of the Center for Advanced Orthopedic Studies, Beth Israel Deaconess Medical Center and Harvard School of Orthopedics.

Additionally, this device will be: non-damaging to the healing fracture, radiolucent to not obstruct the CT scan image, and will constrain the wrist and forearm to stabilize the arm for the duration of the scan. Ideally, this device will work without the removal of the cast and will be compatible with both right and left arms for a range of body sizes. The device is to be completed within the time constraints of the project and within the available budget of \$1,000.

This project began with a literature review to obtain background knowledge. Areas of research included bone mechanics (i.e. the strength of bone), disease state fundamentals (i.e.

fracture healing states), CT scanner function, similar technologies that exist, and mathematical models that are important to the project. We conducted a state-of-the-art search for any similar devices currently available on the market, or in development.

The next stage entailed identifying requirements and key functions of the design (i.e. left and right compatibility) as well as a list of additional features desired in the device (i.e. ergonomics). In the development of mandatory features and supplementary features, we consulted with the Project Advisor (Professor Karen Troy), the Project Sponsor (Professor Ara Nazarian), and with physicians who may use the device. The literature review aids in identifying features crucial to the design, and documentation of relevant developments.

After performing the literature review and development considerations for the design, we developed alternative designs for the project. To do this, we will meet in a group setting to generate multiple designs, including features and functions of each design. Throughout this process, we will evaluate whether the proposed devices meet the list of requirements and features in the wish list. Furthermore, we will also receive feedback from stakeholders in the project (including Professor Troy and Professor Nazarian) to gain a range of perspectives.

From these alternative designs, we selected a design that will best fit the need statement, and generated a prototype and performed experimental tests on the design. The prototype was generated via a computer aided design (CAD) model of the design in SolidWorks, and manufactured using a combination of 3D printed and purchased hardware.

The experimental testing involved measuring the amount of force that is applied to the distal radius of the wrist and correlating this force to a quantitative measurement of fracture healing. Other aspects of the design, such as user comfort and visibility in a CT scan, were assessed as well. The process of generating alternative designs and testing the designs was iterative in nature.

After performing experimental tests, we determined improvements needed to meet the client statement and the device requirements. These changes were based off from experiments. A full outline of the design process can be found in Chapters 3-4.

This report is divided into eight chapters, and this first chapter provides an overview of the process followed during the project. Chapter 2 presents background literature, which provides resources to help solve the problem we are working on and provides a clinical framework for the project. Chapter 3 details the client statement, constraints and goals given to us in the initial phase

of the project, and our interpretation of the problem. Chapter 4 provides an overview of the design options that we considered and the reasoning that we followed in selecting designs. Chapter 5 displays data collected from experimental testing to verify that components of the device are working properly, and to guide design development. Chapter 6 discusses non-technical considerations (such as economic and societal impacts) that were made. Finally, Chapter 7 highlights the final design and Chapter 8 discusses conclusions and future recommendations that were formulated.

Chapter 2 : Background and Literature Review

This chapter presents the clinical and technical background which lays the foundation for the fracture-healing measurement device. Several topics covered in this chapter include: the epidemiology and classification of distal radius fractures with a focus on Colles' fractures, the biology and biomechanics of fracture healing, and healing complications and treatment techniques for distal radius fractures. Additional topics include a section on orthopedic imaging techniques with a focus on the HR-pQCT imaging technique used in this project. This chapter concludes with a state of the art review of similar devices for applying a mechanical load in medical imaging.

2.1 Distal Radius Fractures

Fractures of the distal radius are exceptionally common, with 640,000 occurring per year in the United States [9]. These fractures are four times more common in women over 35 years of age than in men over 35. Due to several factors associated with aging that cause bone weakening in women, 70 percent of distal radius fractures occur in postmenopausal women, the target population for the proposed device [10]. The radius is the larger of the two forearm bones linking the hand to the elbow, on the thumb side. The radius is uniquely designed to allow wrist motion and forearm rotation. The end closest to the hand (distal) is especially susceptible to fracture because it comprises approximately 80% of the wrist joint surface and bears nearly the full force from a fall onto the outstretched hand [10]. It is important to note that complication rates can vary widely in distal radius fractures. Overall, distal radius fracture complications have been found to occur in as few as 6% of patients and as many as 80% of patients, depending on the definition of complication with an incidence of 23% when identifying distal radius complications was the primary purpose of study.

2.1.1 Classification of Distal Radius Fractures

Distal radius fractures are classified per fracture pattern, fracture cause, and severity of fracture. There are two common variants of distal radius fractures that are characterized by the direction of forces applied to the wrist during a fall. First, Colles' fractures, the most common type

of distal radius fracture, occurs when falling on an outstretched hand, where the hand is flexed backward towards the wrist. Second, Smith's fractures are caused by the opposite mechanism, a fall onto the top of an outstretched arm in which the hand is flexed forward under the wrist from backwards fall onto the hand. The common distal radius fracture patterns are presented below.

2.1.2 Colles' Fractures

The most common type of distal radius fracture is the Colles' fracture, shown in Figure 2.1. A Colles' fracture is a fracture of the distal radius caused by a bending force to the outstretched palm while the wrist is positioned in dorsiflexion. These fractures are typically transverse across the metaphyseal region of the distal radius and located 25 to 40 mm proximal of the radiocarpal joint. Colles' fractures exhibit a characteristic failure pattern with the crack initiating from the anterior surface of the radius (in anatomical position). These fractures are typically caused by one of two different modes. The first is a low-energy impact, usually the result of falling forward from standing onto one's hand, with the palm outstretched to break the fall. These are usually seen in postmenopausal women due to fragility from decreased bone density. The other common method of obtaining a Colles' fracture is a high-energy impact, typically a sports related injury in children and young adults [11]. The Colles' Fracture can be seen in the image on the right of Figure 2.1. The image depicts a complex fracture with fragment movement.

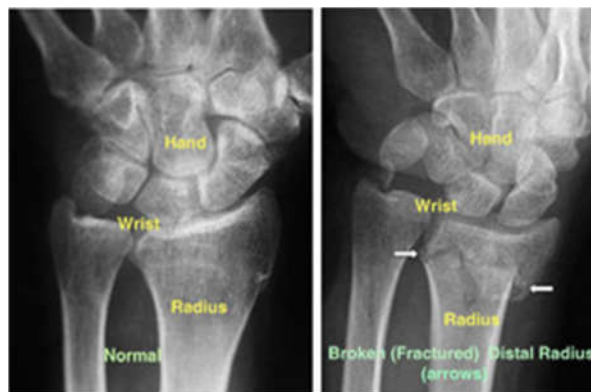


Figure 2-1 X-ray image of a normal bone and a broken distal radius [12].

Five distinct fracture patterns have been described by D.L. Fernandez, MD, based on the direction and degree of force applied to the radius in the fall; this categorization is known as the Fernandez Classification [13]. Several fracture patterns are characterized by bending. Figure 2.2 depicts a Colles' fracture caused by a bending of the bone when the hand is extended backward on the wrist.



Figure 2-2 Colles' Fracture [14]

2.1.3 Smith's Fractures

Smith's fractures are the less common sister fracture to the Colles' fracture. Figure 2.3 depicts a Smith's (volar) fracture, which is caused by "bending" in the opposite direction, with the hand flexed forward under the wrist.



Figure 2-3 Smith's Fracture [12]

2.1.4 Complex Distal Radius Fractures

The third fracture pattern, shown in Figure 2.4, is characterized by shearing stress, and can take many forms. In this fracture, one end of the bone moves in one direction while the other moves in the opposite direction, like a highway being sheared by an earthquake. In osteochondral fractures, the entire joint cartilage is sheared from the end of the radius with its underlying support bone. This is a highly unstable fracture, and treatment is difficult because of the small size of the fractured fragments and attached joint cartilage. Stabilization often requires internal or external fixation to achieve reduction and permit healing.



Figure 2-4 Osteochondral Fracture [16]

Another type of fracture is based on compression, shown in Figure 2.5. This fracture can be caused by falls from a height or other high-energy injuries, in which the hand and wrist bones can be compressed against the flat surface of the distal radius which yields under the significant applied load. This compressive injury impacts the smaller wrist (carpal) bones into the joint surface of the radius, which alters the lattice framework of the inside of the bone and smashes fragments of the joint surface into the radius itself.



Figure 2-5 Compression Fracture of the Distal Radius [17]

A fracture-dislocation is a high-energy injury, in which the carpal bones are dislocated from the end of the radius (as shown in Figure 2.6). Along with injury to the supporting ligaments of the wrist, this may result in fragmentation of a portion or all the joint surface.



Figure 2-6 Fracture Dislocation of the Distal Radius [18]

The final fracture pattern is a complex injury to the distal radius, as shown in Figure 2.7 below. This is a catastrophic injury which causes extensive damage to the joint surface, fragmentation of the widened flare (metaphysis) of the distal radius, and damage to the shaft of the radius and/or the neighboring ulna. Often, these combination injuries require complex treatments to successfully reconstruct the damaged elements.



Figure 2-7 Complex Fracture of the Distal Radius [19]

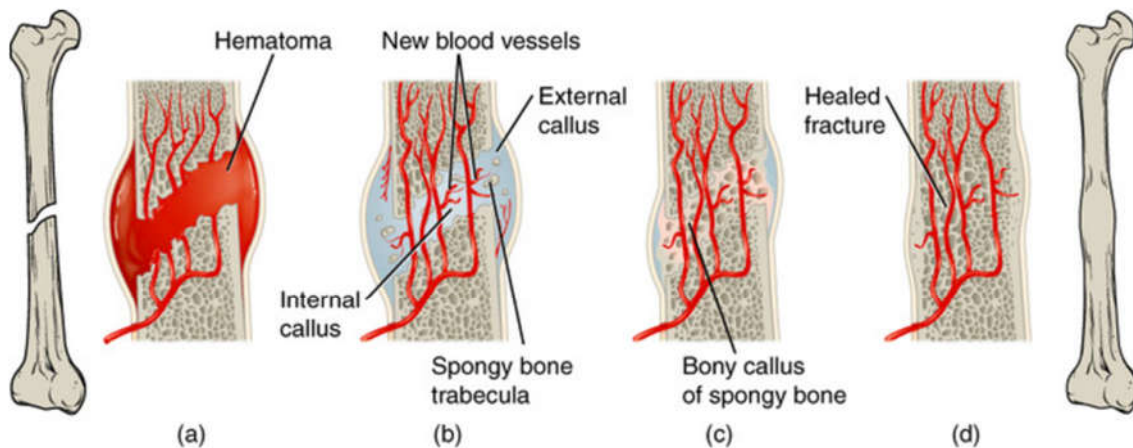
2.2 Fracture Healing

Skeletal remodeling is continuously occurring in the bones of healthy individuals, breaking down and resorbing old bone that may contain micro damage, and laying down new bone in its place. Normally, a remodeling cycle will take around four months to complete, with 10% of bone being turned over every year. Fracture healing is a normal biological response to bone trauma, characterized by Regional Acceleratory Phenomenon (RAP) where the normal remodeling rate experiences a sudden increase. In healthy adults, a fracture will normally heal in 6-12 weeks with proper care, depending on the bone [20].

2.2.1 Biology of Fracture Healing

A fractured bone will tear vascular structures which results in the formation of clotted blood (also known as a hematoma) at the site of the break (shown in Figure 2.9a). After the blood vessels are sealed, capillaries grow into the hematoma and phagocytic cells remove the dead bone cells. Fibroblasts produce collagen fibers that connect the ends of the broken bone and osteoblast (also known as bone-forming cells) start to form woven bone. Woven bone is characterized by layers of aligned fibers at rotating angles, and can be quickly laid down to provide stabilization (Figure 2.9b). This region, known as the callus, can achieve mechanical stability despite reduced material properties by increasing its cross-sectional area compared to the healthy bone resulting in lower stress conditions. The next step involves the formation of a bony callus. In this phase, the fibrocartilaginous callus is converted into the callus of spongy bone and the broken ends of the bone are bridged (Figure 2.9c). The last step is the bone-remodeling phase; in this stage, the bony callus is remodeled via osteoclasts (bone cells that degrade bone) followed by osteoblasts. Remodeling replaces woven bone with normal lamellar bone in the cortices, and trabecular or spongy bone near the ends of long bones and in flat bones (Figure 2.9d). The bone-remodeling phase can take many months to return to normal dimensions, and the bone can

remain uneven for years, in both long bones and flat bones (Figure 2.9d).



Stages of fracture repair

The healing of a bone fracture follows a series of progressive steps: (a) A fracture hematoma forms. (b) Internal and external calli form. (c) Cartilage of the calli is replaced by trabecular bone. (d) Remodeling occurs.

Figure 2-8 Stages of fracture repair [21]

2.2.2 Mechanical Properties of Healing Fractures

The biomechanics of healing bones are described in a foundational study using rabbit femurs. Bone exhibits four biomechanical stages of fracture healing [22]. Identifying the stages of fracture repair is important because it provides an objective method to predict delayed unions and nonunion, and to determine the level of activity that is safe for patients with a fracture. In this study, rabbit bones at various stages of healing were subjected to destructive torsional testing. Four mechanical classifications maximum torque, torsion angle, energy absorption, and stiffness were determined to identify the stage of fracture healing and indicate degree of mineralization.

Experimental testing on tibia fractures in rabbits show that in the first stage of repair, there is a low stiffness rubbery failure pattern at the fracture site. Low torque leading to large angular deformation in the 21-day curve, shown in Figure 2.10, indicates this rubbery behavior. In the second stage, the bone fails with a high stiffness and hard-tissue pattern at the fracture site, depicted as the 27-day curve in Figure 2.10.

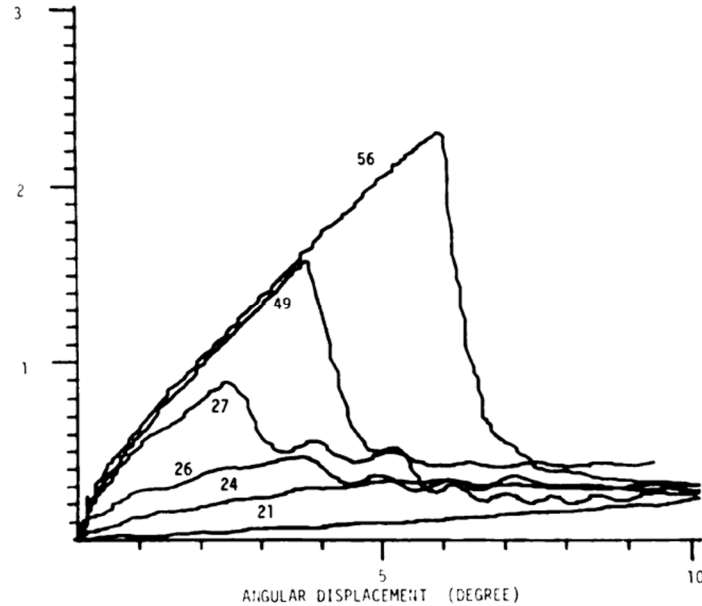


Figure 2-9 A torque-angle graph of six bones representative of the entire healing period. The numbers on the graph indicate days of healing time. As the healing progresses, there is an increase in the strength of union shown by changes in the torque-angle graphs.

In the third stage, the bone fails partially through the fracture site and partially through the intact bone indicating mineralization and mechanical property continuity extending through the fracture site. Like the second stage, the third stage is characterized with a high-stiffness, hard-tissue pattern shown in the 49-day curve in Figure 2.10. Finally, in the fourth stage of healing, the site of the failure fracture is not related to the original healing fracture, and the bone fails with a high-stiffness pattern like the 56-day curve in Figure 2.10. A notable result of this study is that there is a distinct change in the load-deformation curve at 26-27 days from a rubbery quality to a much stiffer, hard tissue pattern. It is in this transition from the elastic, low stiffness resistance to the more rigid, high stiffness resistance that postmenopausal women with healing distal radius fractures often remain without sufficient progress. This background in the biomechanical stages of fracture healing is important to the project because it indicates a quantifiable mechanical property, stiffness, that permits determination of the healing stage of a distal radius fracture through standard, mechanical testing methods [22].

2.2.3 Distraction osteogenesis

Stiffness determination by mechanical testing requires applying a force sufficient to produce displacement in a healing bone callus, a proposition which may seem detrimental to bone

healing at first consideration. All tissues have a preferred degree of mechanical loading, which promotes normal, healthy function, and may prompt healing after injury. It has been established that a small degree of motion, on the order of 0.2 to 1.0 mm, is beneficial to bone healing [23]. Bone healing can be influenced using controlled loading environments. This process is known as loading/distraction osteogenesis. In this method, distraction of the bone on a routine schedule is accomplished with a stable external fixation of the fracture. This method can correct bone deformities and achieve healing in complex fractures via an Ilizarov device. Distraction rates in literature are typically around 1 mm per day. Distraction is split into four increments a day for ten days to improve bone healing. The distraction is incremented due to better relaxation of the soft tissue [24]. Distraction increases bone healing due to the increased blood flow and metabolic activation of the tissue in that area when placed in a loaded environment. A study in sheep compared distraction rates of 0.3 mm/day, 1 mm/day and 2 mm/day. The 0.3 mm/day rate resulted in rapid healing at first and slower healing in the later stages. The 1 mm/day rate was found to be ideal with healing beginning slower at first but healing more rapidly as the loading was continued. The 2 mm/day rate was found to be too rapid and risked impeding the healing process due to the formation of fibrous tissue in the gap between bone ends as days of the distraction process increased. This distraction for all cases was daily for 40 days [25].

Distraction osteogenesis provides important clinical evidence that displacement produced by mechanical testing is not harmful to healing bones when performed at a slow, controlled rate and within small ranges. Furthermore, the loading associated with the proposed testing may even prove beneficial to fracture healing. Once established, the fracture strength test device will permit the quantification of fracture healing through stiffness recovery, thus permitting the assessment of fracture healing interventions.

2.2.4 Frequency and population for this project

Bone mass decreases as part of the natural aging process, beginning around age 15 for both men and women. For women, however, this bone loss is more pronounced, leading to an increased risk of fracture and a compromised healing environment in the bones [26]. Following menopause, there is a decrease in estradiol, which in turn causes an increase in osteoclast

differentiation. Osteoclasts are bone cells that absorb bone tissue, and so a decrease in estradiol results in increased bone resorption and net bone loss. In severe cases, this often leads to osteoporosis, a condition where the bones develop voids and decreased density. The risk and severity of a fracture is inversely proportional to the cortical area, thickness, and volume density of the bone. This combined with an increased difficulty in maintaining balance while walking makes it extremely likely for postmenopausal women to fall and fracture the distal radius. Thus, the population most likely to incur distal radius fractures is also the population least equipped to heal them. The proposed measurement device will permit monitoring and quantification of healing, allowing physicians to better treat patients.

2.3 Fracture Treatment

Colles' fractures can be treated in many ways depending upon the severity of the fracture and the extent of soft tissue injuries. Most stable distal radius fractures are treated by a traditional plaster or fiberglass forearm cast following reduction, when bone fragments are returned to anatomical position. A fracture is considered stable if the fragments are unlikely to displace from reduced position. These are typically fractures seeing less than 2 mm of displacement, less than 5 degrees change in radial inclination and less than 10 degrees in dorsal angulation. Casts prevent angulation and mal-rotation, provide relative stability for the healing fracture, and are suitable for transverse Colles' fractures. Typically, a fracture is first casted with plaster when the limb is still swollen, and is later replaced with a more durable fiberglass cast [20]. Colles' fractures typically heal in 6-8 weeks with a fiberglass or plaster cast in a healthy individual. In elderly patients, 2 or more out of every 3 stable fractures will displace prior to fully healing when treated only with a plaster cast [20]. This can result in nonunion, and/or delay normal healing, and usually requires surgical intervention to provide external or internal fixation to maintain fragment reduction. The device to be designed will aid in the early identification of healing defects to improve physician information and treatment outcomes for patients.

2.3.2 Fracture Healing Complications

A fracture is considered reduced when the fragments have been placed in contact with each other and in their anatomical position. Proper reduction and stability is crucial to healing rate

and completeness. However, some movement is both beneficial and required for proper callus formation and healing. A fracture is deemed unstable if there is not sufficient immobilization of the fragments relative to one another, which may result in fragment displacement, excessive movement, or loss of anatomical reduction. Stable reduction with an appropriate amount of movement must be maintained to promote healing. When this is not the case, or when the biological healing environment is compromised due to other factors, (such as disease, malnutrition, or hormonal changes) healing can fail to proceed normally, leading to healing complications.

Fracture healing complications fall into two categories: delayed union and nonunion. A fracture is a delayed union if healing is still progressing in the appropriate stages, but more slowly than expected in a normal, healthy bone. A fracture is a non-union if the fragments fail to heal and produce a rigid, bony connection. Of significant clinical importance, the hormonal changes that occur during menopause cause the remodeling equilibrium between resorption and deposition in healthy bone to be shifted towards resorption. This results in a net loss of bone mass, often leading to osteoporosis in postmenopausal women and placing them at significant risk for fracture healing complications due to a lack of robust osteogenic response.

Proper immobilization usually promotes the completion of healing. Even with good immobilization, at risk populations can experience healing malfunctions. Delayed union can occur when there is limited blood supply to the area, infection, or fixation that is too rigid [20]. With delayed union, it is not possible to predict degree of healing or the point of sufficient healing to uncast a patient based solely on time since injury, necessitating a measurement tool.

The other bone healing defect is non-union, which occurs when the bone does not fully heal, but instead maintains a soft cartilaginous connection. Non-union occurs if the bone ends are much too far apart, lack adequate stability, or if the individual's body does not have the resources necessary to grow bone as in osteoporotic women. In more serious cases, hypertrophic nonunion is caused by inadequate fracture stability during healing, which promotes excess callus formation resulting in the fracture space filling with cartilage and soft tissue. Hypertrophic non-union is visible in bone x-rays because it results in flared edges on the bone fragments, as seen

in Figure 2.8. Most seriously, atrophic non-union occurs when the bone ends are reabsorbed and rounded resulting in no attempt at healing evident; the fracture space fills with fibrous tissue [20]. Often, surgery with fixation is required to correct non-union and promote proper bone healing. Excessive motion and nonunion can occur due to poor cast fit resulting from limb volume change due to swelling reduction and loss of muscle mass during casting. These effects may not be identified by the physician until after the normal healing time has passed as there is currently no monitoring technique available.



Figure 2-10 Hypertrophic non-union [20]

Other complications of Colles' fractures include compressive neuropathies, tendon rupture or damage, complications from fixation, shoulder-hand syndrome, stiff hands and arthrosis after fracture. Compressive neuropathies and complications from fixation usually occur from the cast or pins used for healings. It is possible for pins to become infected, break or fall out of proper positioning. A condition called "stiff hands" occurs when the proximal interphalangeal joints become inflamed usually due to improper cast application. Less common complications, such as arthrosis and shoulder-hand syndrome typically occur when the bone fragments are not healing in proper alignment. Tendon damage is possible when the displaced bone fragments abrade the tendons. For these reasons, extreme care must be taken in casting distal radius fractures, and it is desirable to promote optimal healing to prevent excessive casting time.

2.4 Imaging Techniques

There are several methods for the medical imaging and evaluation of the structural integrity of bones. These include X-ray radiographs, MRI, CT, and sonographic methods. The imaging techniques presented here differ in mode of acquisition and sensitivity to tissue properties. Also presented is the proposed imaging and interpretation method for the fracture-healing measurement device.

2.4.1 Orthopedic Imaging Techniques

X-ray

An X-ray radiograph is an image produced by passing X-ray radiation through a part of the body onto a radiosensitive film. This produces the familiar black and white images of bones and internal structures where radio dense structures (such as bones) appear white, and radiolucent structures (such as muscle) appear dark grey to black. Radio density is denoted in Hounsfield units, Hu, which correspond to gray scale values in which a higher Hu value indicates higher radio density. Depending on the region imaged, peripheral X-rays have a moderately low radiation dose equivalent to about 3 hours of background radiation.

MRI

Magnetic Resonance Imaging (MRI) is a non-invasive technique which uses magnetic fields to polarize the spin direction of atoms in the body. The radio frequency emitted by these atoms permits the determination of location of structures in the body. These images are taken in 2D slices and digitally stacked to create a 3D image of the region of interest. MRI technology does not involve the use of radiation; however, it is best suited for soft tissue applications and therefore not usually used for bone imaging.

CT

The term “computed tomography”, or CT, refers to a computerized x-ray imaging procedure in which a narrow beam of x-rays is aimed at a patient. In a CT scanner, an X-ray source and a detector assembly rotate around the patient. CT scanners use special digital x-ray detectors, which are located directly opposite to the x-ray source. As the x-rays pass through the patient, they are picked up by the detectors and transmitted to a computer. The x-rays are quickly rotated around the body, producing signals that are processed by the machine’s computer to generate cross-sectional images—or “slices”—of the body [27]. One rotation typically takes a second or less, and during a rotation, the x-ray source produces a beam of x-rays that pass through a section of the patient’s body as shown in Figure 2.11.

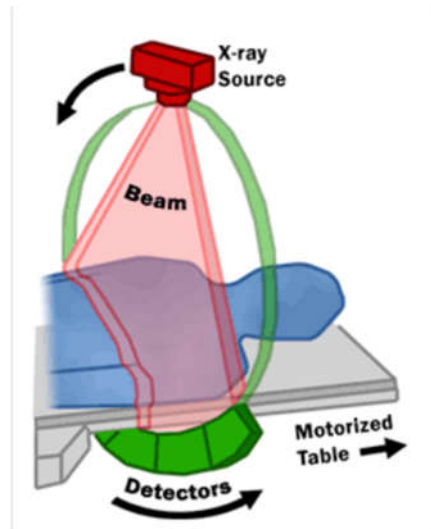


Figure 2-11 Image of a CT beam and a patient in a CT Imaging System [27]

Once several successive slices are collected by the machine’s computer, they can be digitally “stacked” together to form a three-dimensional image of the patient that allows for easier identification and location of basic structures as well as possible tumors or abnormalities. A CT scan is particularly useful when imaging bone fractures, joints, cartilage, or tendons since it produces more detail than would be possible with a conventional x-ray. In a conventional x-ray and a CT scan, dense structures within the body—such as bone—are easily imaged, whereas soft tissues vary in their ability to stop x-rays and, thus, may be faint or difficult to visualize. For this reason, contrast agents have been developed that are highly visible in an x-ray or CT scan [28]. Although a CT scan offers advanced imaging abilities, the amount of radiation exposed to the patient is considerable because the torso must be exposed to image the arm. The radiation dose associated with CT scans that image the abdomen are high, about 10 millisieverts (mSv) or 10 year’s background radiation per measurement [29].

HR-pQCT

This project utilizes High Resolution Peripheral Quantitative Computed Tomography (HR-pQCT) to take high resolution CT scans of only the distal radius (XtremeCT, Scanco, Switzerland). For this application, the radiation associated with imaging an extremity is significantly lower than a whole-body CT scan (less than 5 μ Sv per measurement) and is equivalent to about 1-3 days of normal background radiation [29]. This technique permits imaging resolution down to 82 micrometers, approximately the thickness of human trabeculae. Therefore, this technique permits the imaging of a bone’s internal microarchitecture. The CT scanner takes a series of sequential, 82 micrometer-thick, 2D images over a range of about 1 cm in a high-resolution image. These

images are then stacked to create a 3D representation of the imaged region of the forearm. Through a variety of custom software and imaging processing techniques, the bone's morphology and density can be analyzed, leading to the most comprehensive structural picture of a bone currently available. The main advantage of this imaging technique is that it permits 3D, high resolution imaging of the callus region, which is not possible in the other methods.

2.4.2 Mechanical Considerations in Loading-Response Distal Radius Imaging

Fractures are commonly diagnosed by doctors and radiologists by observing X-ray radiographs. The X-rays traverse the imaged region, producing a 2D image of the underlying anatomy. This method limits fracture assessment in that it 'flattens' structures, which occur throughout the thickness of the imaged region, to one plane, removing vertical positioning information. On such images, a fracture typically appears as a set of lines or discontinuities in the surrounding bone. This information is sufficient to diagnose presence and position of a new or healing fracture, but insufficient to diagnose the strength of the healing region.

The insufficiency of X-ray radiographs has several factors. First, a well-stabilized fracture typically has close placement of fragment edges, producing insufficient inter-fragment space to observe the radio density of the callus. Furthermore, the callus edges become blurred as they are reabsorbed in the healing process, leading to an inability to view the exact edges of the callus region. Second, bone derives its strength both from tissue density and tissue morphology so a radio density measurement of the callus region cannot alone provide a complete description of mechanical properties.

The principle of mechanical testing to determine quantitative mechanical properties of a material is reasonably straightforward, commonly practiced, and well standardized in the engineering fields. To this effect, the goal of measuring the mechanical properties of a bone is a straightforward and familiar task. In mechanical testing, a known load and loading type is applied to a standardized specimen in a standardized fixture. Various behaviors such as displacement, force, torque, and failure load are recorded, and desired properties are calculated. The technical challenge of mechanical testing of a healing human distal radius fracture arises in doing so in the context of variable patient anatomy, in a non-damaging fashion.

The proposed solution is to apply mechanical loading to produce a displacement of the healing bone that is measurable using a high-resolution imaging technique. This permits the calculation of elastic modulus of the bone callus, a measure of stiffness and strength recovery in a healing bone. Distal radius fractures occur primarily in postmenopausal women, for whom the

healing period and rate is not readily predictable in an individual. This leads to failure of early detection of healing complications such as delayed union or nonunion, conditions which may lead to excessive casting times, and require monitoring or intervention for optimal patient outcomes. Clinically, the ability to measure stiffness in a healing fracture provides valuable information to healthcare providers.

This device is designed for use with HR-pQCT imaging, which has a voxel (3D pixel) resolution of 82 micrometers. This means that the minimum measurable displacement would traverse two voxels, 164 micrometers. A semi-automatic process called 'contouring' is applied to separate the bony tissue from the surrounding soft tissue based on the grayscale value of the images. In this application, displacement can be measured by voxel position of the edge of the bone in the direction of loading in the field of view in the unloaded vs. the loaded state. Knowing the force applied and the bone's cross sectional geometry, the elastic modulus of the bone can be computed using standard stress-strain models and used as a clinical measure of healing extent.

2.5 Loading Devices for Imaging Technologies

It is unusual to perform medical imaging on humans in a loaded state due to a variety of factors including injury, motion artifact, and impracticality. Presented here is a state of the art review of loading devices for medical imaging.

2.5.1 Similar Devices

Through extensive review of the background literature and patent searches in the United States, Canada, Europe, and Asia, it was found that there was only one patent application for a device for mechanical loading during medical imaging.

In this device, a mechanical force is applied to a portion of the patient's body during imaging [30]. The purpose of applying a mechanical force is that during imaging, the severity of an injury is not always apparent because the person's body weight has been removed from the affected area. In this apparatus, a load is being applied to the patient's body while the patient is lying prone on a flat surface during the imaging procedure. A spring-loaded mechanism applies a compressive force indirectly to the thorax through the lower limbs, shoulders, and head. The patent also includes a device for placing a portion of the patient's body in traction to remove all loads during the imaging procedure. The patent application provides a method for applying a load to the patient's body during imaging procedures, and includes methods to engage the thorax

portion of the patient's body for stability while the imaging procedure is performed. Figure 2.12 shows a simple schematic of the design.

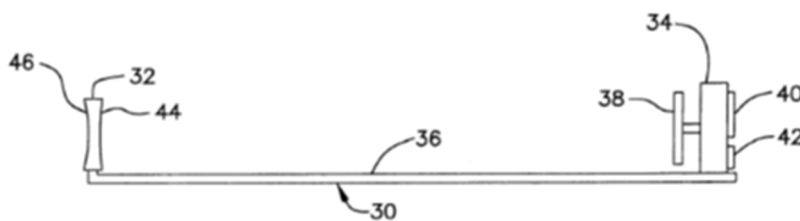


Figure 2-12 Device that can apply a mechanical load during imaging [30]

This device is not considered a relevant competitor since it focuses primarily on the thorax and lower extremities. Furthermore, it is a diagnostic tool, and is not used specifically to measure bone strength recovery in healing fractures. Of note, no other devices were found which provided loading for in vivo imaging of humans. The device developed in this project represents a novel contribution to the field of fracture healing measurement and diagnostics.

One study utilized micro-computed tomography (μ CT) to analyze fracture calluses. The goal of this study was to identify changes in fracture callus structure and composition that occur over time. Standard metrics that were quantified included the total callus volume (TV), mineralized callus volume (BV), callus mineralized volume fraction (BV/TV), bone mineral content (BMC), tissue mineral density (TMD), and the standard deviation of mineral density (SD_{TMD}) [31]. The rationale behind performing the study is that bone strength and stiffness are fundamental qualities that define healing. Although these properties are difficult to measure in a clinical setting, computed tomography provides quantitative as well as 3D measurements of the structure and mineralization of a fracture callus; these metrics may be related to callus stiffness and strength. Therefore, CT-based analysis of callus structure and composition may lead to the development of reliable and noninvasive metrics of healing. One key goal of this study was to determine which quantitative measures are most predictive of callus stiffness and strength.

To achieve this experimental objective, μ CT was utilized to study bone healing in 188 mice samples. Furthermore, regression analysis was implemented to test for the dependence of callus mechanical properties on the μ CT outcome measures, and principal components analysis (PCA) was used to describe the variability in callus structure and composition among all specimens. Based on this experimental study, tissue mineral density (TMD) was the measure that discriminated most strongly among changes in callus structure. Similarly, the variation in callus structure and composition was also largely captured by mineralized callus volume (BV), bone

mineral content (BMC), and callus mineralized volume fraction (BV/TV). These factors explained 51.2% of the total variation in bone healing [31].

In summary, most the variability in callus structure and composition among specimens was captured by outcome measures that quantify the absolute and relative amounts of mineralized tissue in the callus. Taken together, the results relate the relationship of bone stiffness and strength to quantitative computed tomography measurements. These measures provide quantitative methods of assessing bone integrity in the HR-pQCT imaging portion of the proposed fracture strength measurement technique.

Presented above is the relevant clinical and technical background necessary to understand the proposed healing fracture strength measurement device. The device is also situated in the context of similar loading devices and its novelty and clinical need is demonstrated.

Chapter 3 : Project Strategy

Documented below is the process and justification used to refine the project goals, generate and compare design options, and arrive at the final designs. Throughout, this process follows the engineering design approach to guide project development. This process begins with the initial client statement. The need statement stems from the initial client statement, background research, discussions with project sponsors and stakeholders, and internal group discussions. Stakeholders, also known as individuals or groups who will benefit from the project, are also identified. The final client statement is presented using the Problem, Process, Population, Outcome identification approach. The project objectives and constraints are identified to inform the technical parameters of the device. Finally, the project approach is highlighted in Section 3.6 of this chapter.

3.1 Client Statement

In the initial stages of the project, we formulated the client statement shown below. It is important to note that we continued to revise the client statement during the first quarter of the project to clearly define the project goals. The initial client statement begins with the project description provided by the advisors Ara Nazarian, PhD and Karen Troy, PhD. The statement is further revised based upon information gathered in background research and the insight of the team to achieve a refined, final project statement.

3.1.1 Initial Client Statement

The goal of this project is to design and fabricate a radiolucent in-scanner device that applies a known mechanical load to a fractured radius to observe bone displacement and measures the strength of healing distal radius fractures in High Resolution Peripheral Quantitative Computed Tomography (HR-pQCT) imaging. By measuring the strength and bone displacement, the device can help prevent premature cast removal and allow for early identification of healing complications.

3.2 Client Statement Development

The need statement and a stakeholder analysis presented below are used to ensure that the final client statement accurately identifies the problem to be addressed and the needs of the stakeholders to be served by the project.

3.2.1 Need Statement

The need statement specifically identifies the area of need that the project is to address for the client. Physicians currently have no method to measure the extent of healing in distal radius fractures leading to premature cast removal and late detection of healing complications. There is a need for a fracture-healing test device for use in a High Resolution Peripheral Quantitative Computed Tomography (HR-pQCT) scanner to allow physicians to measure bone healing in patients with Colles' fractures. The tangible result of this project is to develop a device that can be used to quantitatively measure bone strength recovery in healing distal radius fractures. The greater impact of the device is to improve patient outcomes by allowing physicians to assess bone healing stage, provide a framework for the design of similar devices for other common fracture sites, and create a device that can be used to assess the effectiveness of new interventional drugs and therapies.

3.2.2 Stakeholder Analysis

There are several parties affected by this project. To guide a maximally useful design, we identified and analyzed the effects of this project on all stakeholders. The stakeholders are listed below.

1. **Project Team** - Our team benefits from this design project because its successful completion is necessary to receive our undergraduate degrees. Successful realization of project goals and device design may also lead to patents or publications, and enhances our knowledge and competencies in our chosen fields of Biomedical and Mechanical Engineering.
2. **Karen Troy, PhD.** - Professor Troy is investing time into advising the project team, and the project will benefit Professor Troy because it may lead to additional publications, patents, and other intellectual property. Additionally, a fully functional fracture-strength test device would aid in her lab research to understand bone healing.
3. **WPI** - The outcome of this project reflects upon WPI and its reputation as an educational and research institution. WPI also invests monetarily through the project budget.
4. **Ara Nazarian, PhD** - Professor Nazarian and his lab is invested in the success of this project as it will allow them to better understand fracture healing and to improve the treatment of patients with distal radius fractures. Professor Nazarian also stands to enhance his professional reputation by sponsoring this project. Additional funding from his lab may also support the project.

5. **Orthopedic / trauma doctors and surgeons** - Any doctor or surgeon will be able to better treat and advise patients with distal radius fractures using this device to measure the extent of fracture healing. This device can also support knowledge and development of treatment for other fracture sites.
6. **Hospitals** - With this device, hospitals may see improved ratings due to increased patient outcomes and satisfaction. The device could also increase the hospital's treatment efficiency and reduce healthcare costs related to previously unidentified healing complications.
7. **Patients** - Patients with distal radius fractures will benefit from early detection of healing defects, and improved estimates of personal healing timelines. The device can help reduce costs spent on interventions, such as surgery to correct healing defects, as well as reduce casting and recovery time.
8. **Imaging centers** - Imaging centers will benefit from the business of providing this service, and the device may also help reduce imaging time.
9. **Society at large** - This device may help decrease the cost of healthcare costs to society, and improve quality of life in patients.
10. **Researchers** - This device can help advance research to understand fracture healing and preferred cellular loading environments.

3.3 Client Statement Revisions

The revised client statement is a refined version of the initial client statement based upon the need statement and stakeholder analysis. The revised client statement identifies the problem presented, the process for addressing this problem, the target population, and the intended outcome. The motivations for revisions to the final client statement are presented below.

Problem: Doctors cannot see the extent of healing in Colles' fractures during the healing period using currently available imaging techniques. This can result in premature cast removal and healing complications such as failure to detect healing defects (including delayed or nonunion defects) early enough to most effectively treat them.

Process: This project will evaluate the needed technical performance parameters, propose, and design a device to apply a known mechanical load to healing distal radius fractures to produce a detectable strain in an HR-pQCT scan. This measurement will be correlated with the extent of healing to inform proper treatment and to evaluate healing processes.

Population: The distal radius fracture is the most common bone injury in adults [30]. Patient populations that are affected by distal radius fractures include: children, athletes, and adults (particularly postmenopausal women). This project will focus primarily on postmenopausal women because 70% of Colles' fractures occur in this population.

Outcome: Design and fabricate a device for use in HR-pQCT scanners that allows physicians to evaluate the degree to which fracture healing has occurred. The design should aid physicians in making accurate treatment decisions.

3.3.1 Revised Client Statement

Design a device that will allow physicians to quantify the extent of strength recovery and bone healing in distal radius (wrist) fractures, which occur primarily in postmenopausal women, to permit early detection of common healing complications, and inform treatment to improve patient outcomes. The device will be used in a HR-pQCT scanner to permit the calculation of callus stiffness by using a known load to produce a visible displacement.

3.4 Project Objectives

Through discussions and advisor meetings, we identified four guiding objectives for the project and device. These project objectives are shown below.

1. **The device should produce a displacement visible in an HR-pQCT image (~164 microns minimum):** A displacement that is visible in the scanner begins at a size of 82 microns, the voxel (cubic pixel) resolution of the scanner. Displacement can most reliably be seen when it spans two or more voxels, about 164 microns. Ideally, the device will achieve highly visible displacements of 1-2 mm.

2. **Permit the testing of callus strength in a healing distal radius fracture:** The device is to apply a mechanical load to test the recovery of strength in fracture calluses in the distal radius. This mechanical load should correlate with degree of fracture healing (the greater the applied load, the more the fracture has healed).

3. **Position and restrain the patient to ensure image quality:** It is important to ensure patient comfort, to secure the hand and forearm to limit movement during the scan, and to reduce the risk of motion artifact in the HR-pQCT images.

4. **Provide a summary and presentation of similar devices and relevant work in the field of fracture strength testing and imaging:** This project is to be situated in the context of relevant medical treatment and literature to support its utility and validity.

3.5 Project Constraints

Similarly, we identified the project constraints through group and advisor meetings during the first quarter of the project. The constraints of the device and the project are presented in this section.

1. **The device should apply a non-damaging force and displacement:** The device must apply a sufficient force to produce a detectable displacement of the bone at the fracture site; however, the force should not cause damage or disrupt healing in the fracture callus throughout the full healing process. The device will need to be able to produce both small and larger forces, depending on the degree of healing. Based on the literature, it is believed that a maximum displacement of 1-2 mm is non-damaging and may be beneficial to bone callus formation [31].

2. **Repeatability:** The device must apply a repeatable force and displacement to patients independent of varying muscle and bone geometries.

3. **Tolerable pain/discomfort associated with the procedure:** Use of the device must not produce a degree of discomfort or pain that is intolerable to most patients. We assume that a reasonable amount of discomfort is no more than 4-5 on the Self-Rated Pain Assessment Scale of 1-10 as shown in Appendix A [32].

4. **Appropriate dimensions:** the device must fit inside the HR-pQCT scanner imaging area, and these dimensions are 5.5" wide by 5.5" tall by 13" deep.

5. **Radiolucency:** The device must be radiolucent within the imaging zone to provide a minimum image artifact in the HR-pQCT scan image.

6. **Device rigidity:** The device must be sufficiently rigid to restrain and apply the needed forces to the patient without itself displacing to ensure measurement quality and repeatability.

7. **Right/Left compatibility:** The device solution must be right/left compatible or should include modules for both sides.

8. **Sizing:** The device is designed to fit the average postmenopausal woman; this patient population represents over 70% of Colles' fractures.

9. **Ergonomics:** Standard ergonomic principles will be implemented in the device to assure patient comfort and device performance.

10. **Manufacturability:** the device must be designed so as to ensure manufacturability with the materials and facilities available.

11. **Cleanability:** the device must be able to be cleaned using standard medical cleaning procedures.

12. **Timeliness:** The device is to be designed and delivered within the project timeline, shown in Table 3.1. Notable dates to respect include paper submission, poster submission, and presentation deadlines.

13. **Cost-effectiveness:** the device must be cost effective to produce and maintain, and project expenses need to be within \$1,000.

3.6 Project Approach

The approach that was taken in this project involved generating a list of design alternatives based upon background research and suggestions from the project advisors. Tension and bending designs were initially prototyped and evaluated.

Each group member generated a variety of designs for both categories. During a group meeting, each member discussed ideas and which designs he/she thought would best meet the objectives of the project. To narrow down the list of designs, we addressed which features were most important in the device. The ideas were then evaluated through the use of a design matrix to determine which designs would best meet the project objectives and constraints. Advisor feedback was obtained and integrated. We developed 3D CAD (computer aided design) models of each design by using SolidWorks, and preliminary designs were prototyped. We then performed prototyping, device testing, and final design verification. We also performed experimental testing with individual components of the design, and as a whole. Finally, we developed future recommendations for the project, and documentation was compiled and finalized in the form of a lab notebook, a presentation, and this report.

Chapter 4 : Alternative Designs

This chapter highlights the process we followed in generating and evaluating designs. In this chapter, there are six main sections including: needs analysis, function specifications, conceptual designs, calculations, decisions, and optimization. Throughout this chapter, tools such as design matrices, CAD models, and drawings, are used to illustrate the design process.

4.1 Needs Analysis

In this section, physical characteristics implemented in the device are further discussed. As previously indicated, the device needs to: apply a non-damaging force and displacement, apply a repeatable and a tolerable level of force, have appropriate dimensions, be radiolucent, and be sufficiently rigid to ensure measurement quality. Additionally, the device should be right and left arm compatible, fit an average postmenopausal woman, be ergonomically friendly, easily manufacturable and cleanable, and cost-effective.

The device should apply a non-damaging force and displacement. This is important because a broken bone that is in early union typically has a Young's modulus (or stiffness coefficient) of 5-10 MPa, while a fully healed bone has a Young's modulus of 15-20 GPa [33]. Based on calculations that are presented later in this chapter, a lower amount of force will cause a damaging displacement to a bone that has partially healed than to a fully healed bone. It is believed that a displacement of 1 mm is actually beneficial to bone callus formation through a process called distraction osteogenesis [34]. A maximum distraction of 2 mm begins to slow the bone healing process if the distraction is performed repeatedly throughout the healing process. A callus distraction greater than 2 mm can begin to damage the healing fracture. Calculations are presented in section 4.4 to determine the amount of force required to displace soft tissue and bone during different stages of healing.

The device is required to produce a tolerable amount of pain or discomfort, corresponding to no more than a 4 or 5 on the standard medical Self-Rated Pain Assessment Scale of 1-10 to permit good patient stillness during imaging. The device should fully restrain the imaged portion of the arm, so that there is sufficient image clarity and repeatability.

An additional need is that the device should fit within the CT scanner. The device may extend somewhat beyond the scanner in length. The device must be highly radiolucent, transparent to X-rays. Materials that are radiolucent include plastics and several types of metals, such as aluminum, stainless steel, and titanium [35]. We decided to incorporate plastic materials into the design because they are more radiolucent in comparison to metals.

The device should be right and left compatible, such that the device can test distal radius fracture healing for both the left and right arms. The device should also accommodate a range of wrist sizes. Literature indicates that the typical wrist size (~ 6.5-7.5 inches in diameter) for postmenopausal women who are the patient cohort that is most affected by distal radius fractures [36]. The device should also be comfortable to patients and should be cleanable via standard medical procedures.

The device should be easily manufacturable via standard manufacturing techniques, such as 3D printing and machining. Initially, we considered developing the device via injection molding. Injection molding combined with carbon fiber mats provide the excellent flexural modulus needed to prevent device deflection. Due to long lead times, the first full size prototype was 3D printed with a Markforged Mark Two with glass fiber and ONYX, a glass fiber reinforced nylon filament. This technique allows for a high flexural modulus for 3D printed materials and fast production times as it is available in one of our advisor's labs. We also considered using Carbon Fiber Reinforced PLA to 3D print the device, which also offers a high flexural modulus.

There is a list of supplementary features that we would like to include in the design. It would be beneficial if the device was applicable to not only Colles' fractures, but also to Smith fractures, which account for 10% of wrist fractures [37]. It would be advantageous if the device can be utilized while the patient is still wearing his/her cast. Additionally, the device should be able to distinguish between partial and complete fracture healing strength. Finally, it would be useful if the device can be utilized in other patient populations (i.e. children, adolescents, and men with distal radius fractures).

The final requirement considered was whether the loading device would be cost effective. We rated this need as a 1 because it was of lesser importance in comparison to the other needs and because of the relatively low anticipated costs and good availability of funds. The prescribed cost of the device is \$1000. For product development, the standard MQP budget was available and supplemented by outside funding from the Center of Advanced Orthopedic Studies, BIDMC. During the second quarter of the project, the sponsoring lab for this project received a significant grant from the Stepping Strong Foundation to develop this device.

4.2 Function Specifications

During the project, we pursued two methods of applying a force: one method uses a tensile load while the second uses a bending force. In both methods, the device restrains the hand and forearm during the scan to provide stability and ensure a clear image. There are several key

functions that are required in both designs. Preliminary designs for both loading methods were evaluated and a bending design was selected for the final design.

A strain gauge measures the force that is applied to the distal radius fracture. Through the drive rods to the distal radius to two decimal places and this metric will be read electronically to the technician. Once the force is measured, a CT image of the distal radius under the mechanical load will be generated.

A process flowchart, shown in Figure 4.1, explains how both of these devices would be used in a clinical setting. It walks through the steps the Physician will take when using this device, from left to right.

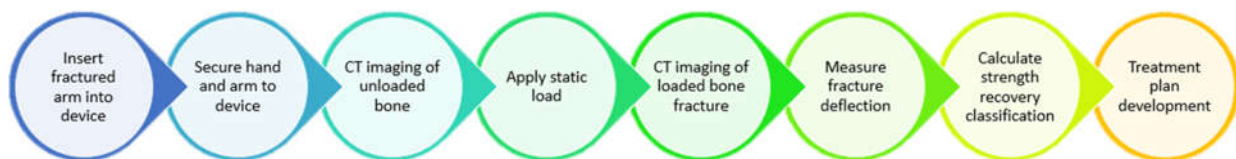


Figure 4-1 Product function flowchart that outlines how the device will be used.

The arm will be secured in the device, and a mage of the unloaded bone will be scanned. Then A Physician/Technician will take a CT image of the loaded bone fracture and measure the amount of force that is applied to the fracture. From the CT image, we will be able to determine the stage of recovery that the fracture is in by performing stress analysis calculations. Then, a Physician can develop a treatment plan for the patient. Physician/Technician will take a CT image of the loaded bone fracture and measure the amount of force that is applied to the fracture. From the CT image, we will be able to determine the stage of recovery that the fracture is in by performing stress analysis calculations. Then, a Physician can develop a treatment plan for the patient.

4.3 Conceptual Designs

We brainstormed to determine what possible designs existed. The design was split up into three major components: including force application, gripping, and force measurement. Force application included what type of force would be applied, and by what methods. Gripping included how the device will interface with the patient's elbow, wrist, and hand in order to apply the force to the bone in a repeatable manner, which was primarily evaluated in relation to the tensile loading designs. The instrument used to measure the load will allow us to determine the force being applied to the bone.

4.3.1 Determining the optimal loading type(s)

The loading type impacts all other aspects of the design and all of the loading types including compression, tension, bending, and torsion were considered. The four types of loading were evaluated on the following criteria, which are essential to the function of the device:

- Ability to open up the healing fracture enough to produce a detectable displacement in order to evaluate how much the fracture has healed.
- Ability to apply a repeatable load to the healing bone.
- Method of loading used which is non-damaging to the healing bone. It is imperative that the device does not further damage or deter healing of the patient, and that the device supports complete and quicker fracture healing.

Table 4.1 illustrates a design matrix that we utilized to compare the various types of loading. The three loading criteria were weighted equally, and the method of loading was rated on a scale of 1-3. In this scale, 1 indicates that the loading type is unable to meet the requirement, 2 indicates that the loading type adequately meets the loading requirement, and 3 means that the loading type fully meets the requirement. The rubric for this design matrix is shown in Appendix B.

Table 4-1 Design matrix to evaluate the methods of loading

Criteria	Compression	Torsion	Tension	Bending
Ability to open the healing fracture	1	2	3	3
Ability to apply a non-damaging force	3	1	3	3
Ability to apply a repeatable force	3	3	3	3
Totals	7	6	9	9

The first loading type considered was compression loading. Compression loading is a safe method to apply a repeatable mechanical load to a patient since the load would be non-damaging to a healing bone. However, compression loading was eliminated because it was determined that loading in compression would not open up the healing fracture, and therefore this method of loading might not produce a sufficient displacement. In order to measure healing, the fracture would need to be further opened, and a compressive force would press the fractured edges together. Torsional loading was also eliminated due to the high likelihood that it would further

injure the healing fracture because most materials are weakest in torsion. Additionally, torsion would not apply a direct, opening load to transverse fractures, the most common type of Colles' fractures. Thus, we decided to further pursue designs using both tension and bending since these loading types meet the criteria described above. Both methods of loading should be able to open the fracture enough to detect a displacement and apply a repeatable load to healing bone. Since bones are stronger in tension and bending in comparison to torsion, a higher force could be applied without damaging a healing bone. Furthermore, tension and bending loading types would be able to apply a direct load to a transverse fracture, the most common type of Colles' fracture.

As seen in Table 4.1, the loading types with the highest total scores were Tension and Bending, and they had received a 3 for each requirement. The compression loading type received a 1 for its ability to open a healing fracture, and torsion received a 1 for its ability to apply a non-damaging force.

Preliminary designs for tension and bending design aspects are considered in this chapter. Based upon preliminary testing and other design aspects presented below a bending design was selected for the final design.

4.3.2 Overview of Loading Mechanisms for the Tensile Device

Various potential loading mechanisms were considered. The most feasible mechanisms were a worm screw, a rack and pinion, a linear spring, a wave spring and a pulley.

A worm screw works by rotating on a 90-degree angle on a shaft as shown in Figure 4.2, and this mechanism transmits motion and power at various speeds and speed ratios. Advantages of worm screws include: they operate smoothly, occupy little space, and can produce a high amount of torque [38].

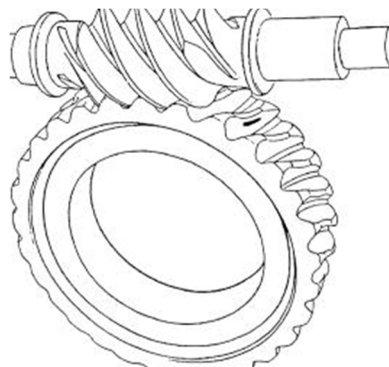


Figure 4-2 Schematic that depicts how a worm screw works [39]

Worm screws are also easy to make non-back drivable, which means that the mechanism can be loaded and the resulting internal forces will not cause the mechanism to return to the initial

state. This is important for maintaining static loading and mechanism stillness during imaging. Disadvantages of worm screws include: they can have high power losses, and can have a lower efficiency due to considerable sliding action and friction from surface area contacts. These disadvantages are not problematic for this project because the goal is not to transmit power efficiently but to reliably apply static loading. A screw drive operates similarly to a worm screw, and it works by translating rotational motion of the threaded rod into linear motion of the threaded nut, as seen in Figure 4.3. It provides the same advantages and disadvantages as a worm screw.

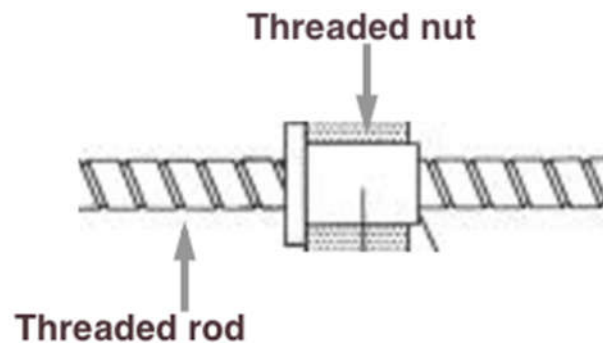


Figure 4-3 Image of a screw drive [48]

A device that is similar to a worm screw, though usually less stable and fine in adjustment, is a rack and pinion. Figure 4.4 shows how a rack and pinion device works. In this device, the pinion (circular component) is spun and the rack is moved side-to-side.

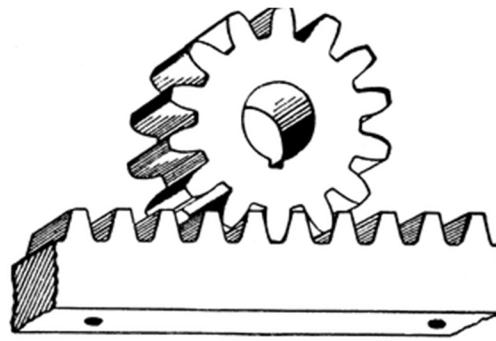


Figure 4-4 Components of a Rack and Pinion device [40]

Some advantages that a rack and pinion mechanism offer are that they are compact, robust, and provide good control over the amount of force that is applied. Disadvantages of a rack and pinion mechanism are that a rack and pinion can only work properly only under certain levels of friction, and a high wear in a rack and pinion device. For example, when the friction is too high, a high rack pinion device will require high forces to operate. This device also relies on creating a

significant force between the two components which can be challenging in light-weight mechanisms.

Another device that can be utilized to generate a tensile force is a spring. In a spring, an object is deformed by a force and it can return to its original shape after the force is removed. Types of springs include wave springs and coil springs, which are shown in Figure 4.5. Wave springs offer several key advantages, which include: they offer space savings by reducing the spring height, can apply a wide range of forces and are cost effective [41].

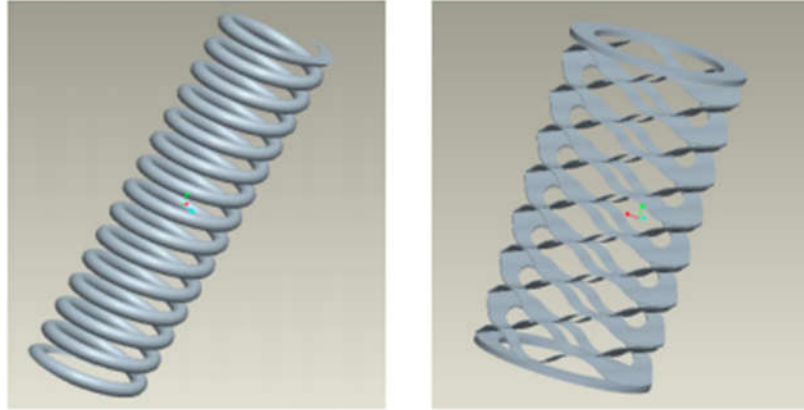


Figure 4-5 The two types of springs: a coil spring (on the left) and wave spring (on the right) [42]

A disadvantage of wave springs is that they do not produce a uniform load distribution and must be used with a force spreader plate. Advantages of coil springs are that they are inexpensive, since they are made of steel and other low-cost metals, and offer a more uniform load distribution in comparison to wave springs. However, they have the disadvantage of not offering the same space savings as wave springs.

A final device that can be utilized to produce a tensile load is a pulley, which allows a cord to transmit force around a wheel's circumference, as shown in Figure 4.6.

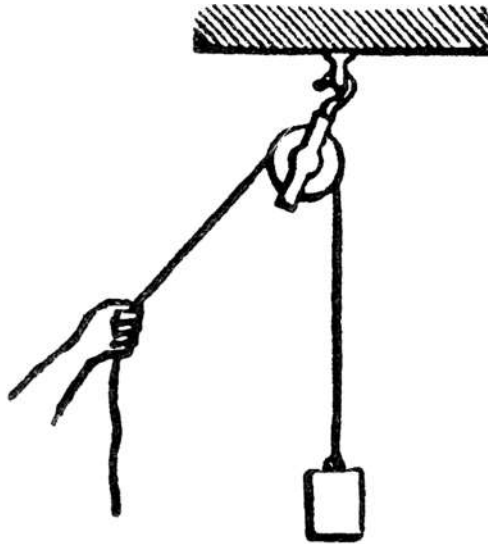


Figure 4-6 Schematic of how a pulley is able to generate a force [43]

An advantage of a pulley is that it can be used to apply a tensile force in any direction [44]. Disadvantages of pulleys include: there can be energy losses due to friction they can have high mechanical advantage, and a high amount of force can be required to move the load a relatively short distance. The main disadvantages of pulleys for this project is that they can have a significant amount of compliance when loaded, especially compared to the other methods presented. They are also only able to provide a pulling force, not pushing and pulling as the other devices presented.

4.3.3 Design evaluation for tension design

A design matrix was created by following the Pugh Analysis form to evaluate all of the potential tension designs [45]. Design requirements were ranked in terms of importance on a scale of 1-4 with 1 being least important and 4 being most important. The possible designs were given a rating from 1-3, which detailed how well the design met each requirement, with 1 being does not meet the requirement and 3 being meets the requirement completely. Each design was given a total point value incorporating the weighted ranking system. This matrix can be seen in Table 4.2 and the rubric for the design matrix can be seen in Appendix C.

Table 4-2 Design matrix to evaluate the methods to apply a tensile load

	Importance of Measurement (1-4)	Linear Spring & guide	Wave Spring	Rack & Pinion	Screw Drive	Pulley
Reliability	4	3	2	3	3	2
Space Constraints	4	3	3	2	3	2
Range of Force	3	3	2	3	3	2
Ease of use	3	3	2	2	3	2
Fine adjustment	2	2	1	2	3	2
Rigidity	2	2	2	2	3	2
Cast Compatibility	1	3	3	2	3	3
Cost Effectiveness	1	3	3	1	2	3
Totals		56	44	46	59	42

One device requirement is reliability, which indicates the effectiveness of the device in applying a repeatable load to the bone. As seen in Table 4.2, this measure was rated as a 4 because it is crucial that the device is able to apply an accurate and sufficient load to the patient so that the fracture is opened. We decided that a linear spring, rack and pinion, and a screw drive would be rated as a 3 because these mechanisms provide good control over the amount of force that is applied. The wave springs and pulleys were rated as a 2 because they are somewhat less reliable in applying a mechanical load.

The second requirement considered for the loading mechanism is the space constraints. The device needs to fit within the CT scanner, which has a height of 5.5", a length of 13", and a width of 5.5". We rated space constraints as a 4 since it is crucial that the device fits within the dimensions of the CT scanner. The linear spring, wave spring, and screw drive were rated as a 3 because these mechanisms occupy less space and will fit within the CT scanner without difficulty. We rated a rack and pinion and a pulley as a 2 because these mechanisms will result in a bulkier design that may have some difficulty fitting within the constraints.

Another measure considered in evaluating the loading mechanisms was the range of force, which was ranked as a 3 because the device needs to apply a range of forces to quantify the degree of healing. Based on calculations performed later in this chapter, the range of force required is between a few Newtons to 550 Newtons. A linear spring, rack and pinion, and screw drive were ranked as a 3 because these mechanisms will be able to produce tensile loads within the entire force range for early and intermediate fracture healing. The wave spring and pulley mechanisms were rated as a 2 because these loading devices offer a more limited range of forces and may have difficulty in providing the range of forces needed for intermediate fracture healing.

The ease of use of the loading mechanism was considered in the design matrix. The ease of use was rated as a 3, and it is a relatively important factor for the technician or physician who will be operating the device. For example, physicians/technicians need to be able to operate the device without too much difficulty, and learn how to use the device in a reasonable amount of time. As seen in Table 4.2, the linear spring and screw drive mechanisms were ranked as a 3 because they operate smoothly and would require less effort to operate. In comparison, the rack and pinion, wave spring, and pulley were ranked as a 2 because it is more difficult for the technician to apply the same amount of force during operation.

Another requirement considered is that the loading mechanism should allow for fine adjustment, which means that the technician or physician who is using the device should be able to change the force in reasonably small intervals. In the tension loading design, it is not crucial that the device has good fine adjustment because of the large range of forces provided and this need was rated as a 2. Furthermore, we ranked a screw drive as 3 because this mechanism allows the user to have good control over the amount of force that is applied. The pulley, linear spring, and a rack and pinion were ranked as a 2 because these mechanisms offer moderate fine adjustment abilities. Finally, a wave spring was rated as a 1 because in this device it is difficult to apply a uniform load distribution, and a wave spring will likely not have good fine adjustment abilities.

The next requirement considered was rigidity, which refers to whether the device is able to remain still and dimensionally stable when a mechanical load is applied. This metric is fairly important because the device must remain rigid enough to be stable and motionless during loading to prevent motion artifact in the scanner image. This need was ranked as a 2 since it is less important in comparison to higher level requirements (i.e. ease of use, range of force that is applied, space constraints). For device rigidity, the worm screw and wave spring mechanisms were rated as a 3 because they help maintain static loading and stillness during imaging. However, the pulley, rack and pinion, and linear spring mechanisms were ranked as a 2 because

they will make the device moderately rigid and will provide a stable platform for the arm to be placed upon during imaging.

An additional need is whether the loading mechanism will allow the device to be cast compatible. This criteria is considered as a beneficial item to have and not a “must have” for a successful design. While it would be useful, it is not necessary for the device to successfully function, and this need was ranked as a 1. The pulley mechanism, linear spring, wave spring, and worm screw were ranked as 3 in terms of cast compatibility because they will easily allow for a tensile force to be applied while a cast remains on the patient. Additionally, a rack and pinion was a 2 because it would be more difficult to utilize this mechanism while a cast remains on a patient. While a rack and pinion generally provides good control over the amount of force applied, this mechanism can only work under certain levels of friction. Therefore, it may be more difficult to generate a sufficient force in patients who are wearing a cast.

As seen in Table 4.2, we ranked the linear spring, wave spring, and pulley mechanisms as a 3. However, the worm screw was ranked as a 2 and the rack and pinion was ranked as a 1. A linear spring and a wave spring cost between \$20-50, and a pulley system can cost between \$25-60. Investing in one of these affordable mechanisms would allow us to stay within budget. Similarly, a worm screw costs between \$50-80, while a rack and pinion is more expensive (\$100-250).

As seen in Table 4.2, the worm screw had the highest total score of 59 and the linear spring had the second highest score of 56. Advantages that the worm screw mechanism offers include: good control over the amount of force applied, smooth operation, and ability to apply a range of tensile forces. This mechanism also helps maintain static loading and stillness during imaging, is able to fit in a limited space, and is moderately inexpensive.

4.3.4 Grasping considerations

Grasping considerations are largely specific to the tension loading design, though the general principles presented below continue to be pertinent in the bending design. In addition to evaluating a suitable loading mechanism, we evaluated methods that can be used to grasp the hand and the distal and proximal ends of the elbow during tensile loading. Under ideal, laboratory settings, the distal and proximal ends of the radius would be potted in resin and the bone would be subjected to tensile loading in an Instron machine to apply easily measurable forces and determine the strength in the fractured region. Recreating this loading environment *in vivo* in an injured, human patient presents specific challenges. It is necessary to apply loads to the radius through the patient’s skin, soft tissue, surrounding bones, and joints. These tissues have a large

degree of variability in geometry, movability, compliance, and pain tolerance, which must be considered.

4.3.5 Hand grasping methods

It is more difficult to grasp the hand than the elbow because the cast may be present, and the fingers and metacarpals have a large degree of movability. It is desirable to apply force through as few joint capsules as possible to minimize the risk of injury and reduce slop in the loading environment, which can negatively impact loading repeatability.

For the tension design, we will need to grasp the hand and/or fingers and apply a degree of connection sufficient to securely transmit high forces (550 N), but not sufficient to cause harm to the patient. The designs considered for grasping the hand in tensile loading are presented below. These methods include using a hook and loop brace on the fingers, athletic tape on the fingers, or an under-cast tightenable grasper.

Hook and Loop Finger Brace:

A hook and loop finger brace uses hook and loop as a fastening method to secure a brace made from soft/elastic fabric, such as felt or neoprene, around the fingers and/or hand. Advantages of the hook and loop finger brace is that it provides ease of use, high adjustability, and good patient comfort. This presents some challenges with reproducibility of loading due to the mobility of the fingers and the need to load through multiple joint capsules in the fingers, hand, and wrist. An image of the hook and loop finger brace can be seen in Figure 4.7. It was determined that this method would not be sufficiently secure without rigid portions.

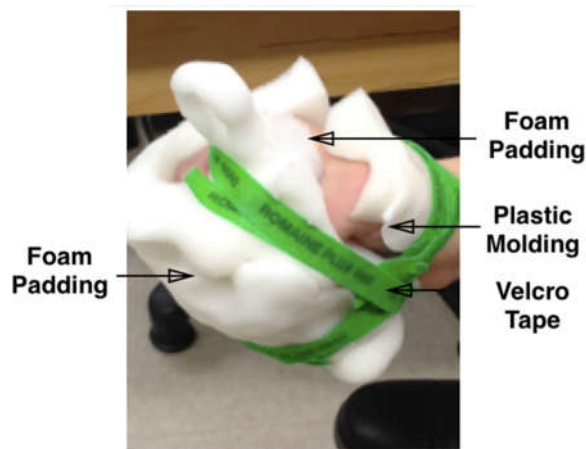


Figure 4-7 Image of the hook and loop finger brace developed with the foam padding, plastic supports, and hook and loop tape labeled

We further developed this brace by adding soft foam and plastic supports to the inner and outer portions of the hand, as seen in the figure. We molded the plastic supports by using Thermomorph Plastic Pellets.

Under-cast tightenable grasper

An under-cast tightenable grasper is a proposed device with thin plastic staves, connected by cording, that are inserted under the cast along the skin. The cord can be tightened in order to produce circumferential compression on the hand. This technique relies on producing sufficient compression to prevent the grasper from slipping off the hand in tensile loading. An advantage of the under-cast tightenable grasper is that it will be able to apply a load through joint capsules in the hand and wrist. However, this method presents challenges with force reproducibility due to differing patient anatomy and casting techniques. Therefore, we decided not to pursue this design past the conceptual phase.

4.3.6 Hand grasping component design evaluation

A design matrix is utilized following the same format to evaluate how potential gripping options will meet the design requirements. We will perform experimental tests in order to evaluate which hand gripping components will work the best with the design. The matrix can be seen below in Table 4.3.

We considered three different hand gripping components: a hook and loop finger brace, under-cast grasper, and an athletic tape finger brace. As mentioned above, we decided not to pursue the cast gripper because it would likely have poor reproducibility.

A hook and loop brace consists of two hook and loop strips, which adhere when pressed together. The advantages of using a hook and loop brace include: its strength, ease of use, and low maintenance. For example, a two-inch sheet of hook and loop is able to hold up to 79.4 kg (778.6 N) and hook and loop does not require replacements very often. Additionally, once the two plastic sheets of hook and loop have been pressed together, the hook and loop can remain together with little continued effort. A disadvantage of hook and loop is that the hook portion can gather particles. In addition, a hook and loop finger brace presents some challenges with reproducibility of loading due to the mobility of the fingers and the need to load through multiple joint capsules.

The second method for securing the hand is to use the athletic tape finger brace. The advantages of athletic tape include that it is light and inexpensive, and it provides support to the patient when applied properly. Athletic tape is also porous and breathable and can allow for a

controlled range of motion. However, disadvantages include: it needs to be applied and removed for each patient, it can be uncomfortable when applied incorrectly to the patient, and it has a lower strength in comparison to hook and loop. The adhesive on athletic tape could be an irritant to skin, particularly for elderly women.

We will consider six requirements in device testing for evaluating the hand gripping mechanisms including: security, patient compatibility, ease of use, cast compatibility, cleanability, and cost effectiveness. Security refers to the effectiveness of the gripping device in properly restraining the hand; this requirement is rated as a 3 because the gripping mechanism needs to keep the hand in place while an external load is applied to the fracture. Additionally, patient compatibility refers to the level of comfort of the hand gripping mechanism. This requirement is rated as a 3 since it is important that the patient is comfortable enough to remain still during the procedure.

The third requirement considered was the ease of use of the hand gripping mechanism. This requirement is rated as a 2, since physicians/technicians who are using the device need to be able to apply the gripping mechanism to the patient in a reasonable amount of time. However, this metric is less important in comparison to “must haves” in the hand gripping mechanism, which include security and patient compatibility.

Another requirement is the cast compatibility, and this criterion is considered as a “nice to have” for a successful design. We rated this criterion as a 2 because it would be beneficial for the gripping mechanism to be able to restrain the hand.

The next requirement is cleanability, which refers to whether the hand gripping mechanism is easy to clean. This design consideration is rated as a 1 because the device does not require sterilization (since the gripping mechanism is used externally on the patient). It is important to note that sterilization would involve removing all microorganisms from the gripping mechanism, while cleaning the gripping mechanism would simply involve reducing the number of microorganisms. This could be accomplished with standard wipe-down procedures.

Finally, the last design criteria for the hand gripping component is cost effectiveness. This requirement is rated as a 1, because there is outside funding available in addition to the budget of \$1000. While it would be helpful if the gripping mechanism is lower in cost, this factor is of lesser importance in comparison to other requirements. An example of the matrix is presented in Table 4.3.

Table 4-3 Design matrix to evaluate potential hand grasping options

	Importance of Measurement (1-3)	Hook and loop Finger Brace	Athletic Tape Finger Brace
Security	3		
Patient Compatibility	3		
Cast Compatibility	2		
Ease of use	2		
Cleanability	1		
Cost Effectiveness	1		
Totals			

4.3.7 Elbow grasping component design evaluation

To evaluate the elbow grasping mechanisms, we considered several devices including: an elbow brace, blood pressure cuff, and bony contacts for the elbow. We used a Pugh matrix during testing to systematically compare the elbow grasping mechanisms.

A padded elbow brace applies force to the proximal end of the radius through circumferential pressure on the medial and lateral surfaces. Advantages that these braces provide include they are: easy to fit and comfortable, are easily cleanable, and skin friendly. Furthermore, elbow braces, such as the brace shown in Figure 4.8, can come with adjustable straps, which allow for a custom fit.



Figure 4-8 Image of an elbow brace that we purchased for testing

However, a disadvantage of using an elbow brace includes that it may not provide enough security while a mechanical load is being applied to the patient's fracture. The level of security needs to be evaluated during device testing.

A second elbow gripping mechanism that we considered using is a blood pressure cuff. An advantage of a blood pressure cuff is that it is relatively comfortable and easily cleanable. Furthermore, blood pressure cuffs are relatively affordable (~ \$15), and they can fit a variety of elbow sizes (like an elbow brace). A potential disadvantage is whether a blood pressure cuff can restrain/secure the elbow when a mechanical load is applied to a distal radius fracture.

Finally, we evaluated whether bony contacts can be utilized to restrain the elbow. To develop bony contacts, group member's elbow using the guide of an articulated skeleton to provide extra pressure near where the bones were palpable from the skin's surface. The pieces were then held together using athletic tape to make a brace insert.

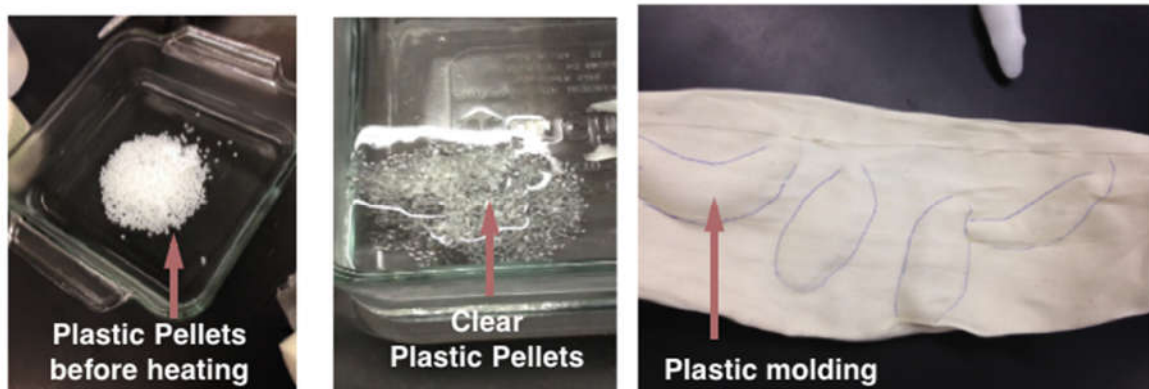


Figure 4-9 Sequence of steps followed in developing the bony contacts

Several advantages that bony contacts (plastic molding) can offer include improved comfort and security to the patient, while a mechanical load is being applied to the fracture. The goal is to apply loading more directly to the skeletal structure. Localized pressure points also reduce the cutoff of circulation and other compression points that caused tingling and cold fingers in other designs. However, a disadvantage is that the bony contacts can make it more difficult to clean the elbow gripping mechanism. The benefits and drawbacks of bony elbow contacts were explored via testing.

4.3.8 Initial Tensile Design

An initial tensile design was created using Solidworks CAD modeling, as seen in Figure 4.10 below. This design uses a worm screw for loading, which fixes the hand and moves the elbow. The basis of the design allows for interchangeable gripping options.

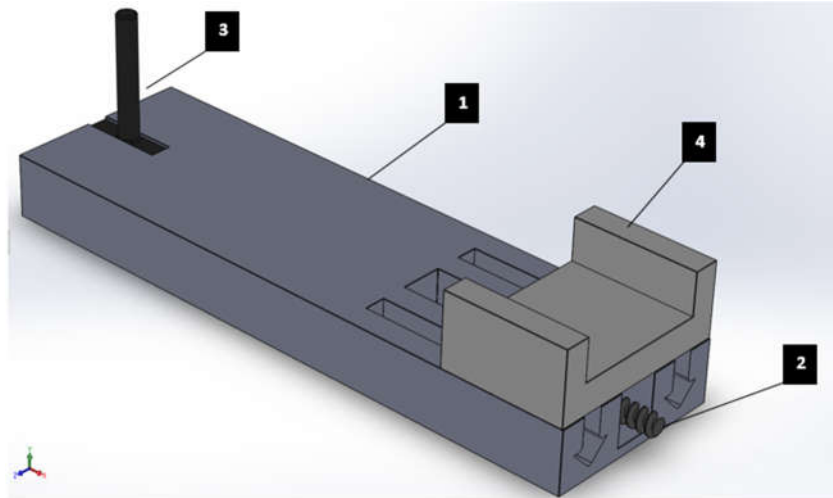


Figure 4-10 Isometric View of the Initial Tensile Loading Design with the Major Parts Numbered

This design consists of four major parts, which are labeled above in the isometric view of the model.

1. Base: The first part is the base, which is 15 inches in length by 4.5 inches in width and 1.5 inches in height. It is a rigid rectangular platform that will house support for the arm and loading mechanism. The other end of the base contains a large rectangular cut out in the middle, which allows for the worm screw to pass through. On either side of the worm screw are two T-slotted tubing slots, which use an arrow-shaped design to allow

for better stability. On the distal end, there is a slit for insertion of the hand restraint peg. Figure 4.11 depicts the top and isometric views of the base.

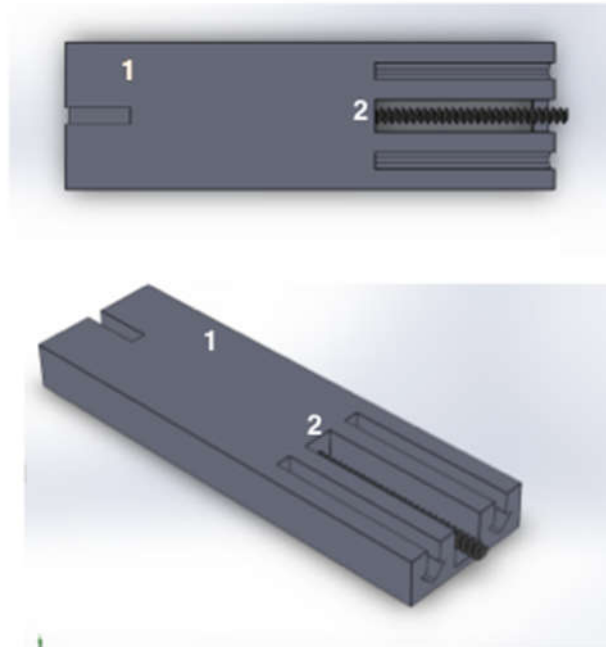


Figure 4-11 Top and Isometric Views of the Base (Numbered as 1) and worm screw (Numbered as 2) of the Tensile Loading Design

2. **Worm Screw:** The worm screw can be seen (in black) inserted into the base in Figure 4.11. The worm screw will be attached to the base inside the hole on the inner side of the cutout, and will fit within the cutout.
3. **Hand Peg:** The third major part is the hand peg, which is shown in Figure 4.12. This is a cylinder that is 1 inch in diameter and 3 inches in height.



Figure 4-12 Isometric View of the Hand Peg of the Tensile Loading Design

The peg will be covered in a thin padding to allow for the fingers to comfortably wrap around, which will aid in gripping the hand in a repeatable manner and location. So far, the hand peg is removable to allow for adjustability. As this design is in an early prototyping stage, the removable peg will aid in ease of preliminary printing and could allow for an interchangeable gripping mechanism if desired. The hand will likely be secured to this peg using a hook and loop finger or athletic tape strapping as explained in earlier sections.

4. Elbow Support: The next part is the elbow support slide, which is shown in Figure 4.13 and the forearm/ elbow will rest within this piece.

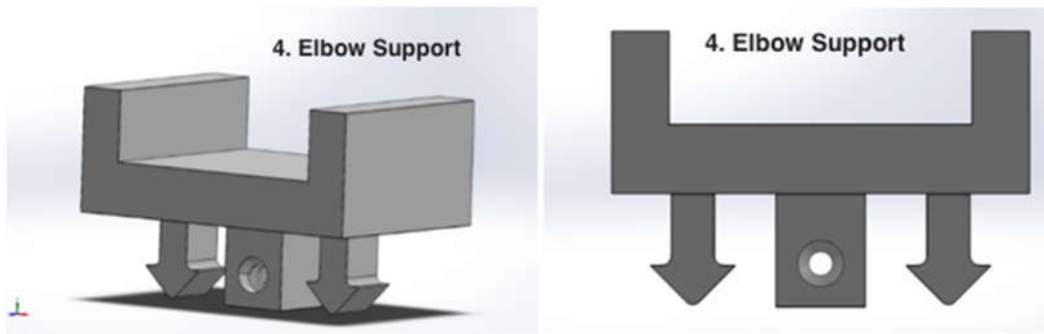


Figure 4-13 Isometric and front 2D view of the Elbow Support

The bottom side of this piece contains the T-slotted tubing inspired arrow shaped sliders, which will fit snugly into the slides. The middle rectangular extrusion contains a threaded hole, which is where the worm screw will be fed. This will allow the elbow support to be moved via the worm screw within the sliders. The elbow will likely be affixed to the slider through the attachment of a semi-rigid elbow brace to the top of this piece. Figure 4.14 displays an image of the tensile loading mechanism that we could 3D print.

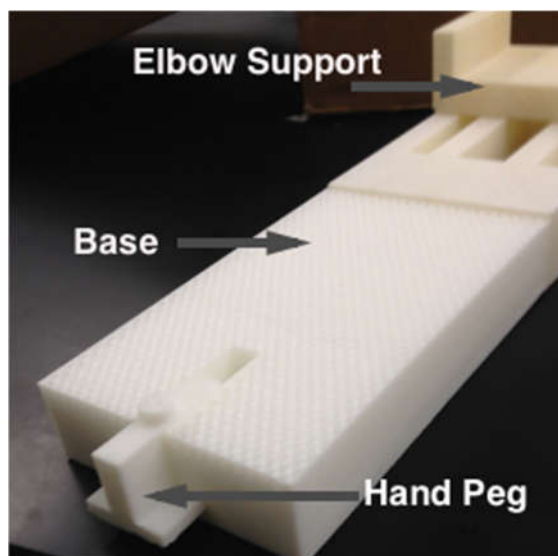


Figure 4-14 Image of the prototype for the tensile design that we built via 3D printing.

This prototype was 3D printed with ABS (Acrylonitrile Butadiene Styrene), which is a commonly used thermoplastic material. One problem that we encountered when 3D printing this model is that the worm screw did not fit into the elbow support slide due to printing resolution. In later stages of the prototyping process, we will use standard machining practices and a material known as PLA with carbon fiber reinforcement. This material offers improved flexural strength in comparison to ABS, and is radiolucent and easily manufacturable.

4.3.9 Updated Tension Design

In the tension design, the device needs to apply an adequate tensile force to sufficiently displace the bone. To achieve this force, the loading mechanism utilizes a screw drive, composed of a rotating threaded rod and a translating threaded nut, like the one shown in Figure 4.15.



Figure 4-15 Schematic of a screw drive mechanism.

This mechanism works by rotating on a shaft to produce linear translation. A screw drive allows for both high force and high precision tensile loading to be applied to the patient's distal radius fracture. An updated CAD model of the design is shown Figure 4.16a. As seen in the figure, the design consists of four components including: 1) Base, 2) Elbow/forearm Support, 3) Hand Peg, and 4) Worm Screw.

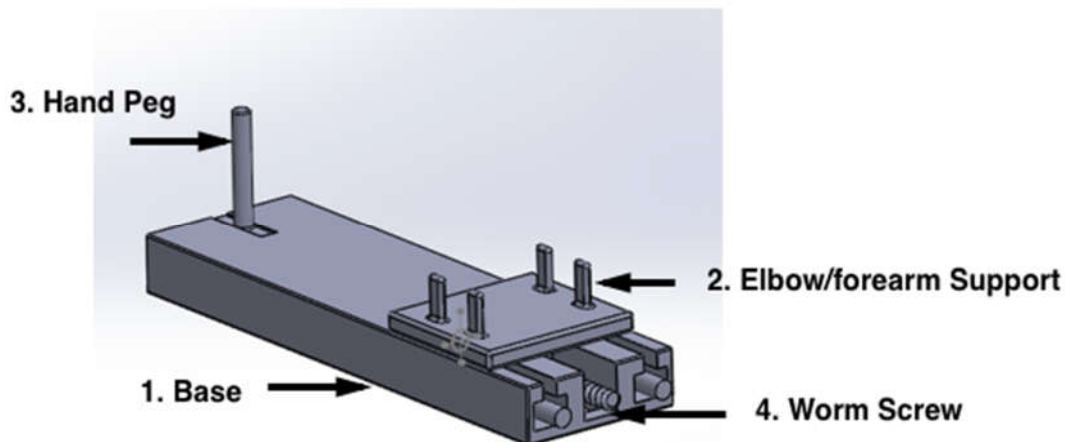


Figure 4-16 CAD model of the tension design with the major components labeled

In the tension design, the base keeps the device stable and houses the elbow support, hand peg, and worm screw. The elbow support allows the patient to rest his/her elbow, and the support is moveable via the worm screw. A feature added in this updated design is the addition of attachment pegs onto the elbow support, which allow an elbow gripping mechanism to be attached. Similarly, the hand peg is the location where the patient can comfortably secure his/her hand while the screw drive will apply the tensile force.

A different version of this design was built as a prototype, and can be seen in Figure 4.17 below.

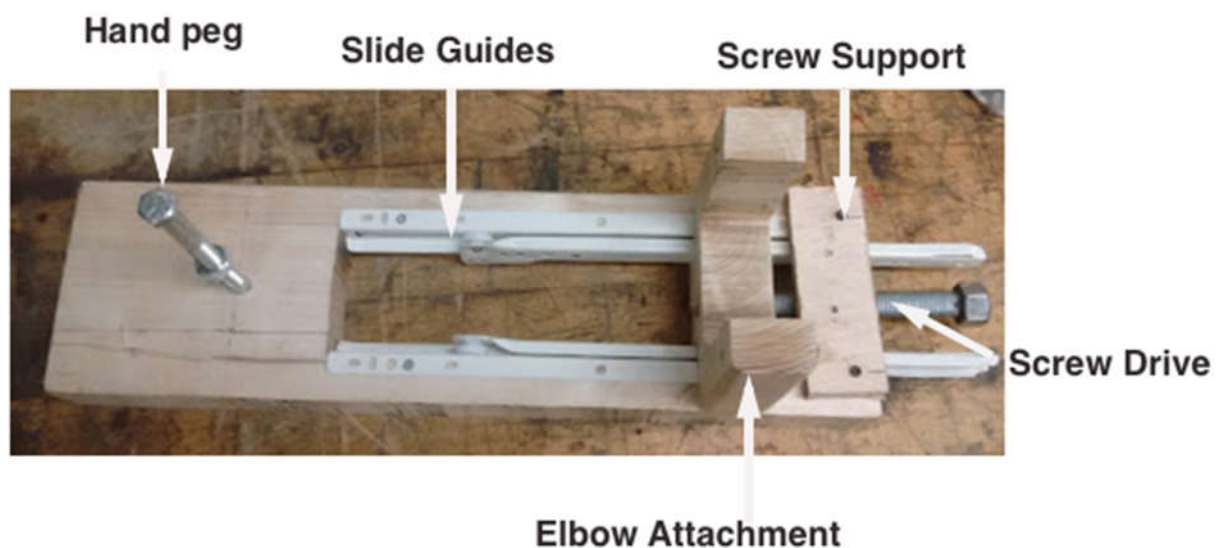


Figure 4-17 Updated tension design prototype fabricated out of wood with the components labeled

The design was changed slightly and utilized drawer slides instead of the guide rods for ease of manufacturing and known reliability. The design was manufactured out of wood because it is strong, cheap and easily manufacturable without lead time. The loading mechanism functions, although it is not yet in a condition to be used in the CT scanner. One drawback of this design that we noticed after building was the difficulty to operate the screw drive in between the drawer slides. The elbow slide contains screws to serve as the gripping mechanism attachment peg. Figure 4.18 below is an image of the built tension design, including the elbow brace containing the bony contacts along with the hand gripper mechanism that was tested.



Figure 4-18 Updated tension design including the gripping mechanisms

4.3.10 Previous Iteration of Project, Side-Application Bending Design

Before the WPI MQP team taking over the project, it was developed by another student. This design was a bending application. In addition to pursuing a design loading the bone in tension, a design loading the bone in bending was evaluated. This design worked off the preliminary device design from a student previously working on the project, named Magdalena Fernandez. The bending design uses a mechanical advantage to apply higher internal bone forces and higher fracture displacement than the tension design without damaging soft tissue. This permits the imaging of incomplete and complex fractures that would otherwise not be feasible to load.

An image of the CAD model of the design can be found in Figure 4.19. This design functions through the force application by a spring of a known stiffness constant k , and the force is applied through a rod to the styloid process and head region of the radius. Furthermore, a platform holds the forearm, and side walls and strapping slots are designed to stabilize the arm.

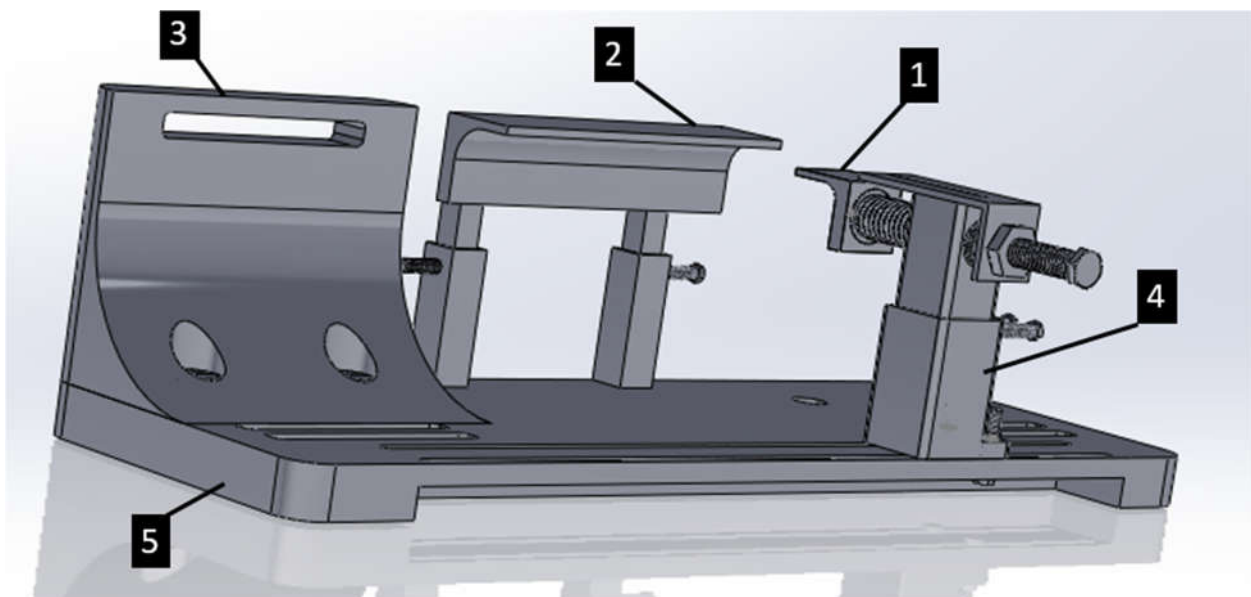


Figure 4-19 Previously completed design utilizing bending with the major parts labeled: 1. Force Application Piece, 2. Arm Alignment Piece, 3. Forearm Support Piece, 4. Spring Attachment Piece, 5. Device base

This device is currently right/left compatible through a process of switching the force application and arm restraint pieces to the opposite side and reattaching them to the base with screws. This change-over process is not quick however, and its ease of use can be improved.

The major aspects of the device are numbered in Figure 4.19:

1. This part applies the force to the fractured radius by pressing against it using a spring of a known constant K . The wrist is lined up with the edge to ensure force application is in the same location every time.

2. The arm is held in place with this piece and it is adjustable for multiple arm sizes through vertical movement. The ledge is pressed down onto the exposed radius portion of the arm to hold it in place.

3. This is a support for the most proximal end of the forearm. The slit on the top allows for a strap to be attached to better secure the arm in place.

4. This is a base for the force application spring, which is adjustable on all three axes.

5. This is the base of the device, which increases device rigidity, and serves as a resting spot for the arm and wrist. The various slots allow for the three moveable parts (parts 1-3) to be moved along the slots to adjust for different arm sizes. The pieces can also be switched to the opposite side for right and left compatibility.

For this device, the spring stiffness was not designated using calculations so more work needs to be done to determine the appropriate spring or springs. Ergonomics and patient comfort are an additional set of improvements for the bending design. To improve the device, padding and hook and loop strapping will be added, as well as adjustments to sharp corners and straight lines. This will allow the device to better accommodate the organic shape of the forearm and improve the user experience. User comfort is also important to maintaining stillness and image clarity in the CT scan. An ergonomic design leads to a clearer image and better information for the physician to guide treatment.

Design aspects in need of further development include:

1. **Ergonomics** - This device currently is not very comfortable due to the presence of sharp edges. It is also not very conducive to varied arm sizes. This could be improved by rounding out some of the rectangular aspects, removing sharp corners, and adding padding to the design.

2. **Slack/Deflection** - This design currently has a lot of slack in the components. One way this will likely be improved is by machining the device, which would also make the design more rigid.

3. **Slow right/left changeover** - This device is slow and cumbersome to change from

the right to left arm setup because many parts need to be moved and screwed into place while keeping all pieces together. Having two separate devices would remedy this problem but would also require higher costs to buy and manufacture materials. Decreasing the amount of moving parts by changing the forearm restraint to be conducive to both right and left arms without alteration would make this changeover more time efficient.

4. **Spring constant determination** - The spring currently in this model is a radiolucent ceramic spring, which was used as a proof of concept design. The spring will need to be replaced by a different mechanism or by a spring that has an appropriate spring constant.

5. **Arm security** - Currently, this device does have slots which could be used to add a forearm strap, but otherwise the device does not restrain the arm in place very securely or repeatedly. An elbow brace, inflatable pressure cuff, or a similar method could be used to restrain the forearm. A strap will likely be added to restrain the hand as well. Motion must be limited to avoid having motion artifact in the CT scanner image.

As mentioned above, limitations in the previous bending design include: ergonomics, slack in measurements, slow right/left changeover, spring constant determination, and arm security. In the updated bending design, described in the next section, we will go through the process of selecting alternative mechanisms that can applying a bending force, including using a lever, 3-point bending, and a screw drive.

4.3.11 Design evaluation for the bending design

We generated three major alternative designs that can apply a bending force. Advantages of using bending as a method to apply a mechanical load include: this method can open a healing fracture and can apply a repeatable and non-damaging force. A disadvantage of applying a mechanical load through bending is that the device will not be compatible for patients that are wearing a cast. Figure 4.20 displays a potential bending design that utilizes a lever.

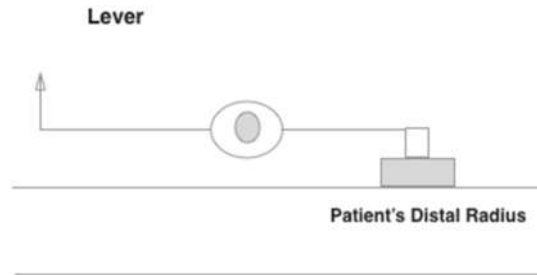


Figure 4-20 Bending design that will utilize a lever

A lever is a mechanism that consists of a rigid bar that rotates about a fixed point (known as the fulcrum). Figure 4.21 depicts an image of a Class I Lever, and in a lever mechanism, force is applied to one end of the lever, and the object to be moved is usually located at the other end.

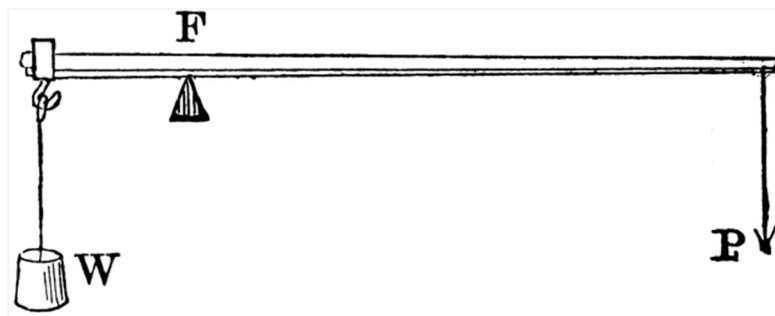


Figure 4-21 Schematic of a Class I Lever that can be used in the bending design [46]

An advantage of using a lever system in the bending design is that it is an effective method to reduce the amount of force needed to move a load. However, disadvantages of lever systems include: there can be significant wear near the fulcrum point (which reduces the mechanical advantage and leads to inefficiencies in the system), and lever systems involve quite a bit of moving parts (which can reduce the reliability of the applied load).

The next bending design that we developed is shown in Figure 4.22. This design would apply a bending force from above the distal radius fracture.

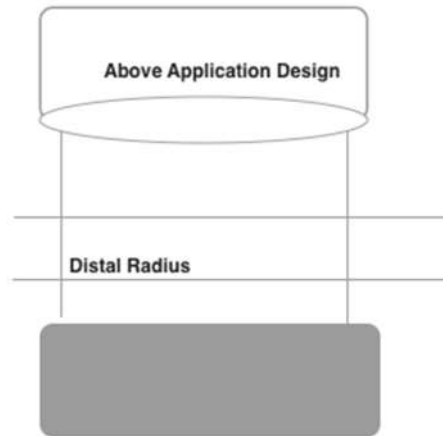


Figure 4-22 Side view image of the bending design that will apply a load from above the point of application. In this image, the patient's right hand is facing down.

Like the other bending designs, an advantage of this design is that it will use a mechanical advantage to apply higher internal bone forces than the tension design without damaging soft tissue. Additionally, this loading mechanism would be able to apply repeatable bending forces, would occupy less space, and would maintain stillness during loading. A screw drive, shown in Figure 4.23, is quite like a worm screw, and it operates by translating rotational motion into linear motion.

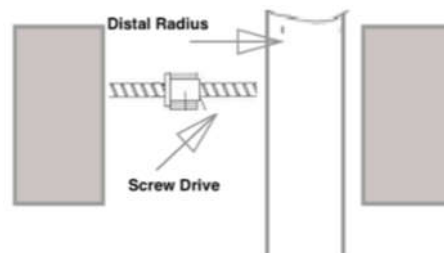


Figure 4-23 Drawing and schematic of the screw drive design to apply a bending force with the distal radius and screw drive labeled

Like a worm screw, advantages that screw drives provide include: they occupy less space, are cost effective, and operate smoothly and quietly. Furthermore, they can produce a wide range of forces and apply a repeatable force. However, disadvantages of screw drives include: they are less efficient and need to be replaced somewhat frequently. Careful material selection can reduce these problems.

A design matrix was developed to determine the optimal bending design. Like the tension design, design requirements were ranked in terms of importance on a scale of 1-4, and possible designs were given a rating from 1-3. Each design was given a total point value incorporating the weighted ranking system, and this matrix can be seen in Table 4.4.

Device requirements that were taken into consideration included the repeatability of the loading mechanism, ability to fit in a limited space, and ability to apply a sufficient range of forces. Additionally, we considered the ease of use and ergonomics, and the ability of the device to change in reasonable force intervals, the device rigidity, radiolucency, and cost effectiveness.

Table 4-4 Pugh Matrix to evaluate the bending designs

	Importance of Measurement (1-4)	Magdalena's Design	Lever	Screw Drive	Above Application
Reliability/ Repeatability	4	1	1	3	3
Space Constraints	4	3	2	2	3
Range of Force	3	2	2	3	3
Ease of use	3	3	3	3	2
Ergonomics	3	1	1	2	3
Fine Adjustment	2	1	2	3	2
Rigidity	2	1	2	3	3
Radiolucency	1	3	2	2	2
Cost Effectiveness	1	3	2	2	2
Total		44	42	60	62

Like the tension design, repeatability and the ability of the design to fit in the CT scanner were ranked as a 4 in terms of importance. The same ranking scheme was followed for the range of forces the design can apply and the ease of use of the design (ranked as a 3) as well as the fine adjustment abilities of the device and the ability of the device to remain still during imaging (ranked as a 2). Finally, we kept the same ranking for the cost effectiveness of the design, which was ranked as a 1.

We added two design requirements, including ergonomics and the design's radiolucency. We added ergonomics as a design requirement because this is an area that can be improved upon in Magdalena's design, and this requirement was ranked as a 3 because it is important that the design is comfortable. We also added the radiolucency as a design requirement since it is important that the device is transparent to X-rays, and this requirement was rated as a 1 because only a portion of the device would need to be transparent to x-rays. The rubric for this design matrix can be seen in Appendix D, and it is quite like the rubric for the tension design.

In terms of reliability/repeatability, we decided to rate the screw drive and design that applies a bending force from above as a 3 because these designs provide good control over the amount of force that is applied. Magdalena's design was given a 1 because it would be difficult to apply a known force consistently, and the lever was given a 1 because there are quite a few moving parts.

Magdalena's design was rated as a 3 for space constraints since it can fit inside the CT scanner without any difficulty. However, we rated the screw drive, above application, and lever designs as a 2 because they would be somewhat more sizeable in comparison to Magdalena's design but would still be able to fit within the CT scanner.

The next design requirement is the range of force each design can apply. We decided to rate the above application design as a 3 since it would be able to provide a mechanical advantage to apply higher internal bone forces. We rated the lever, screw drive, and Magdalena's design as a 2 since these designs will likely provide the necessary range of forces for early and intermediate fracture healing. They might not be able to extend beyond the necessary force range for a healing fracture.

For the ease of use, we ranked Magdalena's design as a 3 since it is relatively easy for Physicians/Technicians to use. We rated the lever and screw drive designs as a 3 because they are like Magdalena's design in terms of how they operate. The above application design was rated as a 2 since this design would be somewhat more difficult to use.

We also considered the ergonomics of each bending design, and we rated the above application design as a 3 since it would likely be comfortable to the patient. We rated the screw drive design as a 2 because this loading mechanism may cause a slight degree of pain. We decided to rate Magdalena's design as a 1 because it contained sharp corners and would likely be uncomfortable to the patient. The lever design is a 1 because it would likely be uncomfortable to the patient.

The loading mechanism should allow for fine adjustment (meaning the technician should be able to change the force in reasonable intervals). We rated the screw drive design as a 3 since

this design provides good control over the amount of force that is applied. The lever and above application designs are a 2 because these designs have moderate fine adjustment abilities. Magdalena's design is a 1 because in this design it can be difficult to apply specific forces.

For device rigidity, we rated the screw drive and above application designs as a 3 because these designs would help maintain stillness during imaging and would promote good stability. The lever design was rated as a 2 because it is less rigid due to moving parts in the mechanism, and Magdalena's design was rated as a 1 because it would not remain rigid when a force is applied.

For radiolucency, Magdalena's design was rated as a 3 because it is completely transparent to X-rays. We rated the lever, screw drive, and above application designs as a 2 because these designs would likely only be partially radiolucent, rather than entirely radiolucent without special materials.

For cost-effectiveness, the lever, screw drive, and above application designs are all a 2 since these designs would likely be adequately cost effective and cost around the same amount. Magdalena's design is a 3 because it seems to be cost effective based on the materials and manufacturing processes that were used.

Based on the design matrix, we selected the above application design because it received the highest matrix score of 62. Advantages that this design provides include: the ability to apply a repeatable load and to fit in a limited space, and the ability to maintain stillness during imaging. Furthermore, this design can provide a mechanical advantage to apply higher internal bone forces than the tension design. Areas of the design that would need to be validated during testing include: the ease of use and the fine adjustment abilities of this design.

Bending Design with Round Frame

A briefly considered design change to better accommodate the imaging region of the scanner was the bending design with a round frame shown in Figure 4.24. This design is visually more elegant and offers significant materials reductions, however it does not allow for accurate force measurement and experiences significant device deflections in loading.

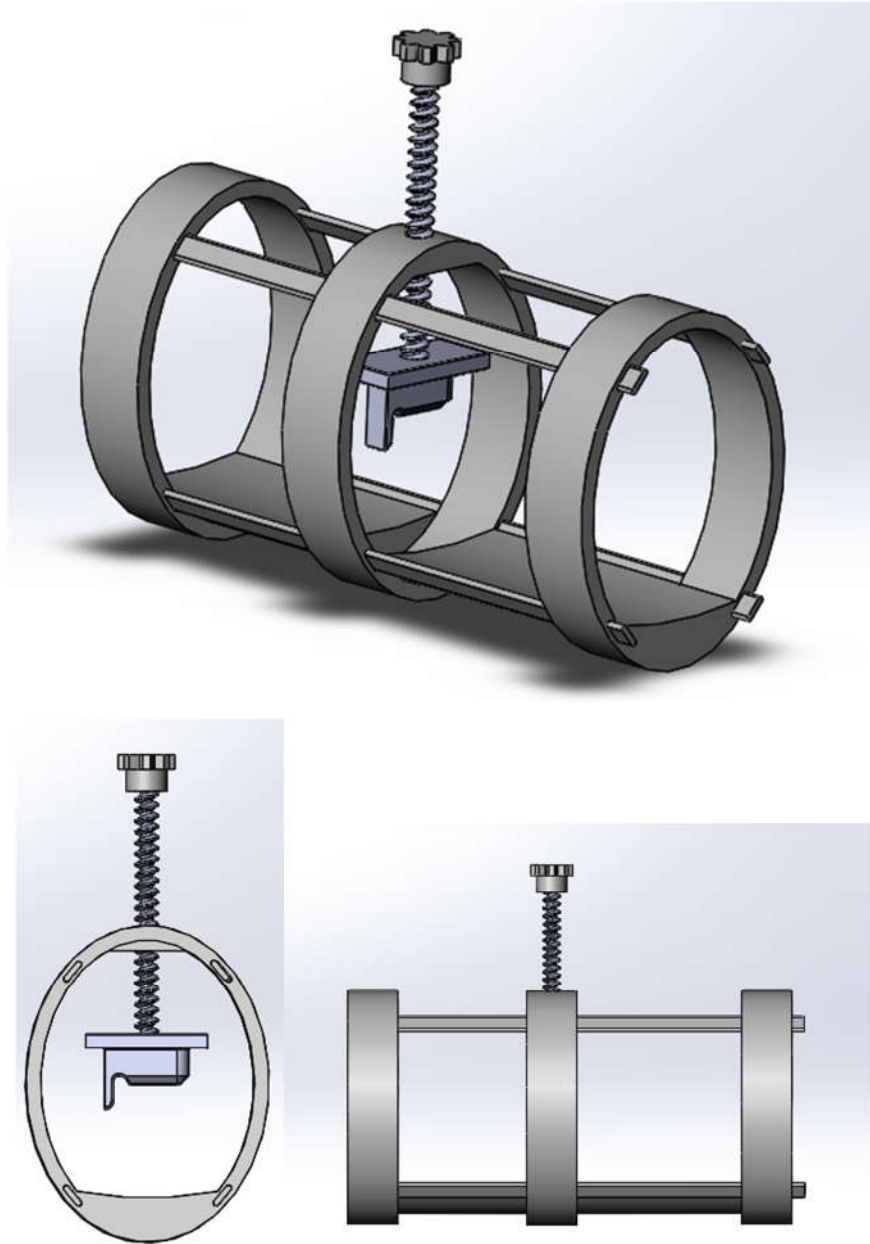


Figure 4-24 Various views of the round bending design with single drive screw

4.3.12 Palm Down 3-pt Bending Design

The basics of the bending design were built off a design that was completed by another undergraduate student, Magdalena Fernandez. In her design, a bending force is applied to the distal radius to measure the extent of fracture healing.

In our design, a 3-point bending force will be applied to the patient's distal radius, as shown in Figure 4.25. The major components of the bending design include: 1) Base, 2) Elbow Support Padding, 3) Hand Support Padding, 4) Force Application Component, 5) Hole, and 6) Screws. This CAD model was sized by using dimensions of the CT bore. This design consists of a base

that holds the elbow and hand supports, and applies a 3-point bending moment to the patient via the force application component.

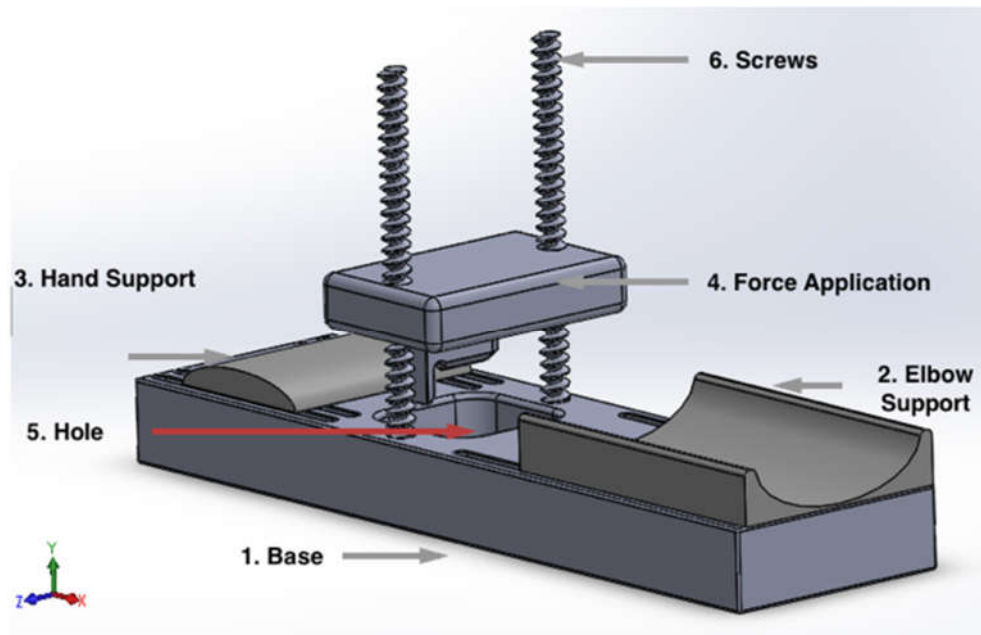


Figure 4-25 CAD Model of the Updated Bending Design with the major components labeled

The main advantage of this design over the previous bending design is that the instability of the forearm caused by resting the forearm sideways with the thumb facing up is eliminated (by rotating the arm to rest on the palmar surface). The hole is the location over which the patient places his/her distal radius. This design provides the mechanical advantage of reducing the load borne by the screw (by splitting the force between two screws), effectively halving the force and torque needed in operation. During later stages of the design process, we will test whether the device can apply sufficiently high internal bone forces to produce the needed fracture displacement. And if the elbow and hand support padding are comfortable and stable for the patient to rest his/her arm upon. Restraining hook and loop will be added to secure the arm to the base in an adjustable manner.

A description of each component of the design is given below.

1. **Base:** The base is a rigid platform that will house support for the arm, elbow, and loading mechanism. The middle portion of the base consists of a cut-out, which is where the bending moment will be applied above. Allowing the force application to follow a three-point bend model effectively while maintaining the structural integrity of the device. The slots cut out along the edges of the base allow for the attachment of adjustable hook and loop (not pictured) to hold the forearm securely in place.

2. **Elbow Support Padding:** This piece has a circular shape and it allows the patient to rest his/her forearm and elbow. This is meant to increase comfort and ergonomics of the device.
3. **Hand Support Padding:** This piece has a curved shape and it will provide support to the hand. It fits the natural curve of the hand to increase comfort.
4. **Force Application Piece:** This piece is attached to the base via screw drives. The rectangular support is moved via the screw drives to increase and release the force on the arm. The rectangular boss houses a pressure point piece. A close-up of the pressure point piece can be seen below in Figure 4.26.

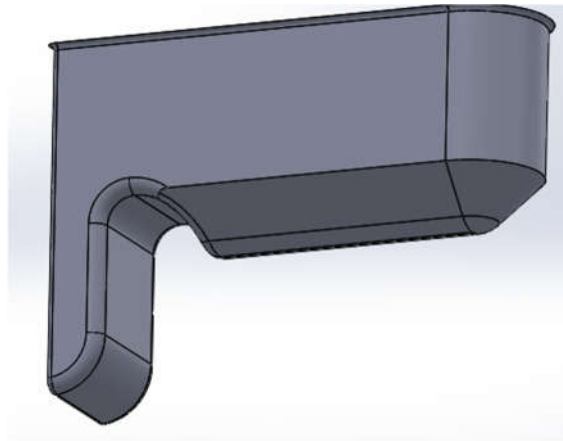


Figure 4-26 Pressure point piece of bending design to apply force to the wrist in a focused and repeatable location

This pressure point contains the longer horizontal extrusion with a rounded edge meant to apply force to the radius. Dimensioning for this is based on average sizes of wrists and radius bones and will require more research to verify that the force will not be applied to the ulna directly. The side of the pressure piece consists of a flat piece to be lined up with the styloid process on the side of the wrist to ensure that the load is applied to the same location of the radius every time.

5. **Hole:** This cut out is the location where the 3-point bending moment is applied to the patient's distal radius.
6. **Screws:** The screws allow the force application piece to move up and down in a measurable manner.

The bending design offers promising improvements over the tension design, which will be further discussed in Section 4.5. A preliminary prototype, visible in the figure below, Figure 4.27

of the bending design was built using wood for the base and rectangular portion of the force application mechanism.

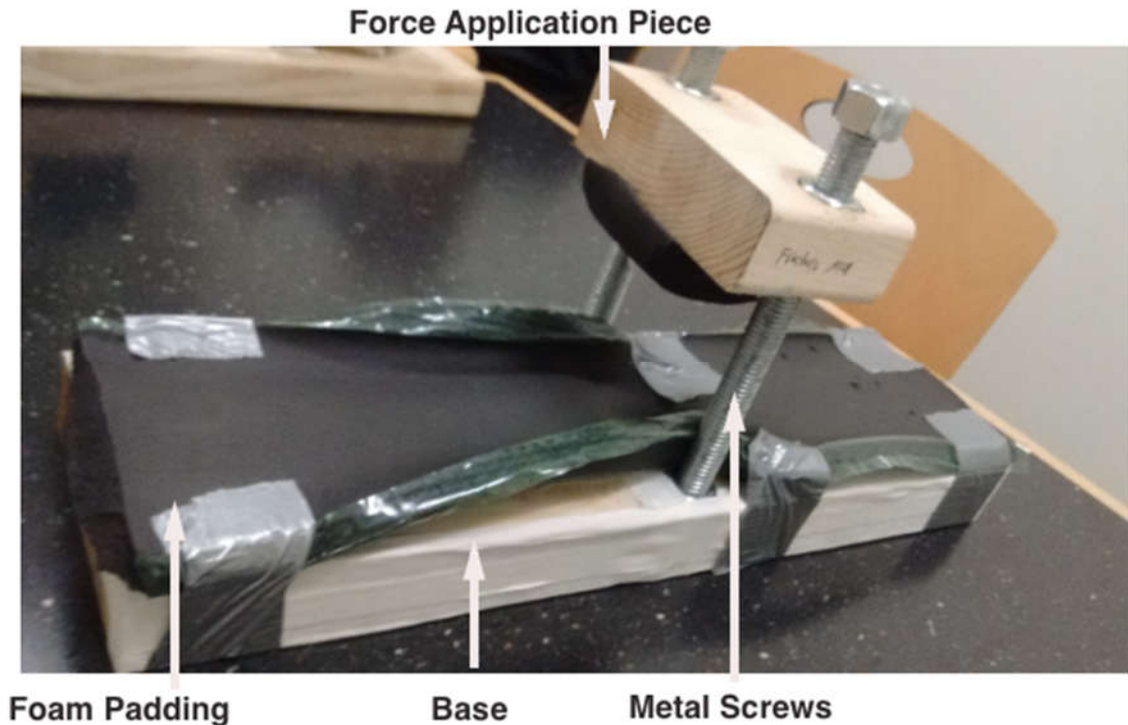


Figure 4-27 Bending Design Prototype with the components labeled

The screws are metal, the padding is foam pipe insulation and the pressure point piece was made from moldable thermoplastic. The finalized bending design will be machined out of PLA with carbon fiber reinforcement to ensure radiolucency.

4.3.13 Optimizing the Configuration of the Bending Design

To analyze the strength and anticipated deformation of the design, Solidworks Simulation software was used. Stress analysis was run on the parts along with varying geometry. For these simulations, the threaded rod holes were fixed in all three axes. The simulations were run with a force of 550 N because this was the max force anticipated to achieve the necessary displacement to diagnose fracture healing levels. Some simulations were run with a force of 550 N total applied while others were run with 550 N applied per face. The further descriptions of simulations describe the force levels applied. Applying 500 N per face is not an accurate representation of the stress values which will be seen but still allows for comparison between designs. Resulting images from the simulations on the standard design of the base piece are shown in Figures 4.28a and 4.28b below. Figure a show the map of the Von Mises stress on the part and Figure b shows the displacement of the part.

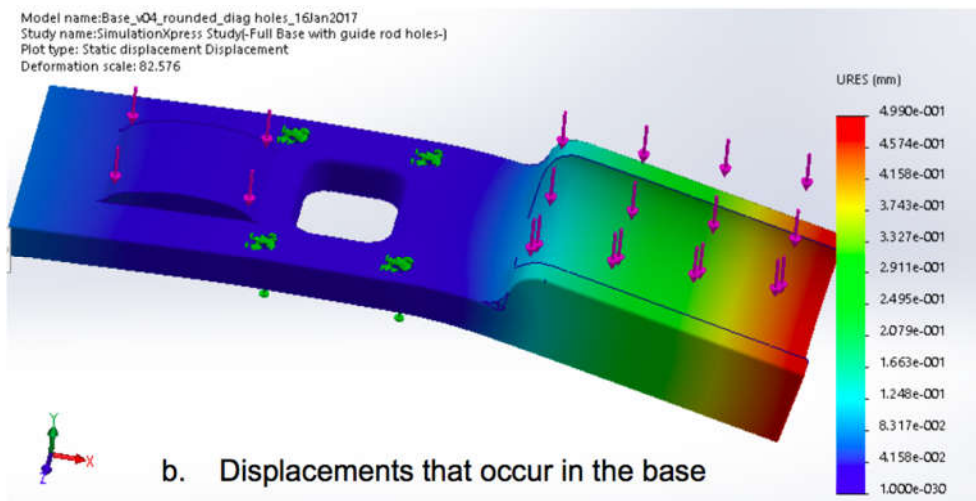
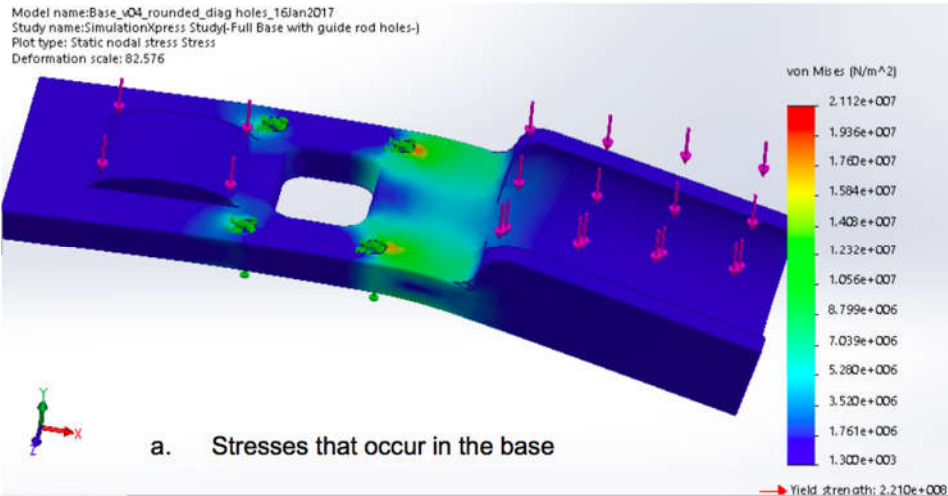


Figure 4-28 (a) Map of the stresses that occur in the base of the model (b) Map of the displacements that occur in the base of the model

The deformation shown in these images is not to scale, as can be seen on the top left corner of the images; this deformation has a scale factor of 82. Some minimal changes on the thickness of the base piece were made, along with comparing simulations of the piece with and without the arm supports. These simulations were found to not be an accurate representation of the behavior expected in the top piece because they did not consider forces applied from design additions such as the connection clips to the machine and the hook and loop for the arms and the guide rods. Focus on stresses in the device were on the geometry of the pressure point piece primarily. Design changes made on the top piece were on the geometry of the pressure point and on the volume of material. Figure 4.29a and b below show the stress and

displacement values of the pressure point piece.

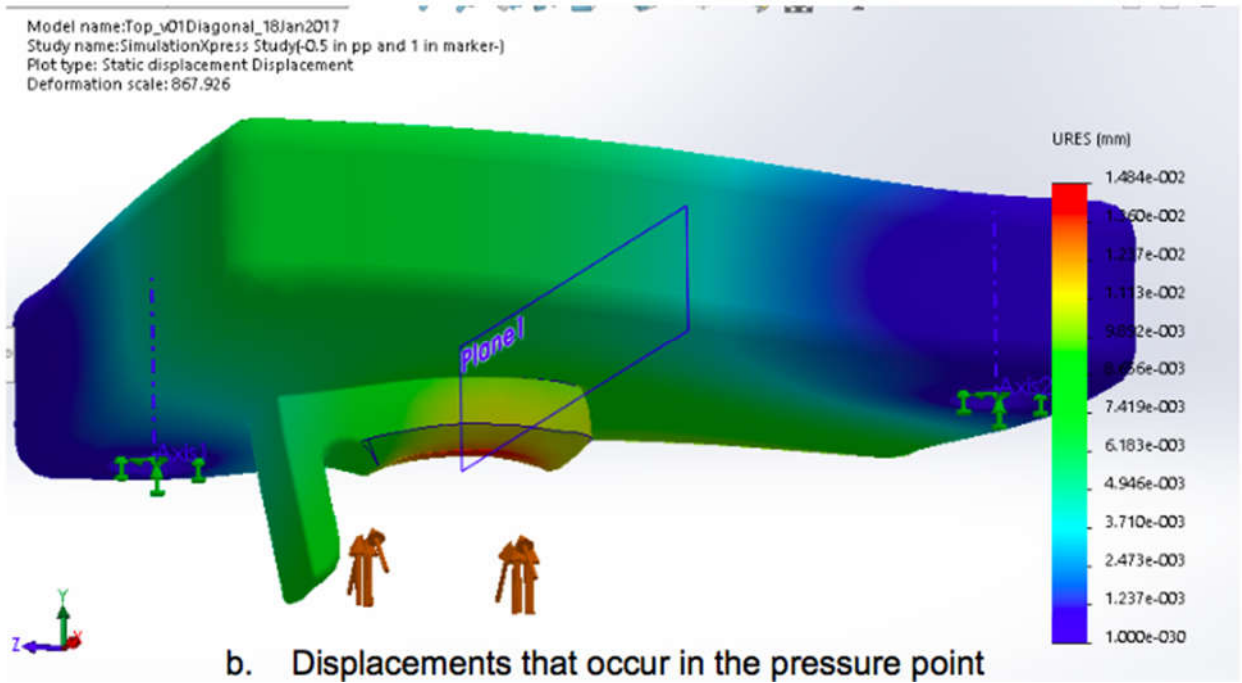
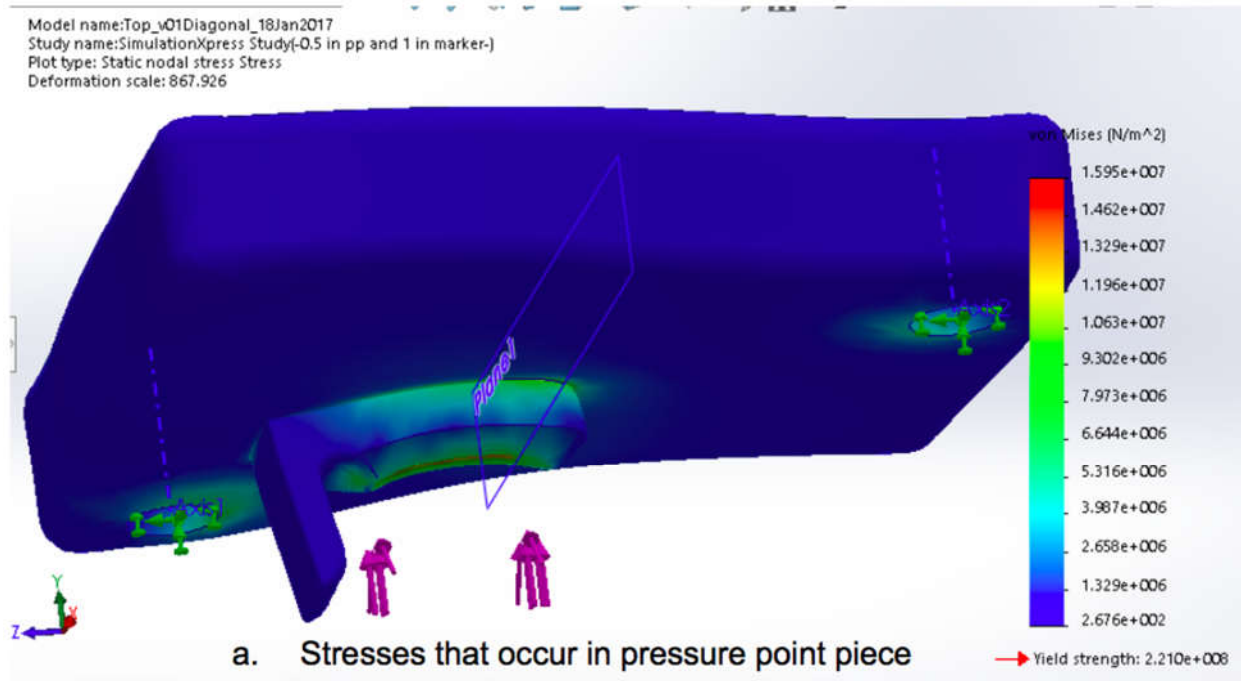


Figure 4-29 (a) Map of the stresses that occur in the pressure point piece (b) Map of the displacements that occur in the pressure point piece

Deformation in these images is scaled up 867 times.

Pressure point Geometry

Several different geometries for the pressure point were analyzed. First, two different shape pressure points were modeled. One had a full round surface with a radius of 0.25 inches as seen in Figure 4.30a and the other had a chamfered tapering off to a smaller face, (resulting in a radius of 0.12 inches) which contacts the wrist as shown in Figure 4.30b. Testing, which will be discussed in Chapter 5, analyzed the comfort of the two pressure point shapes.

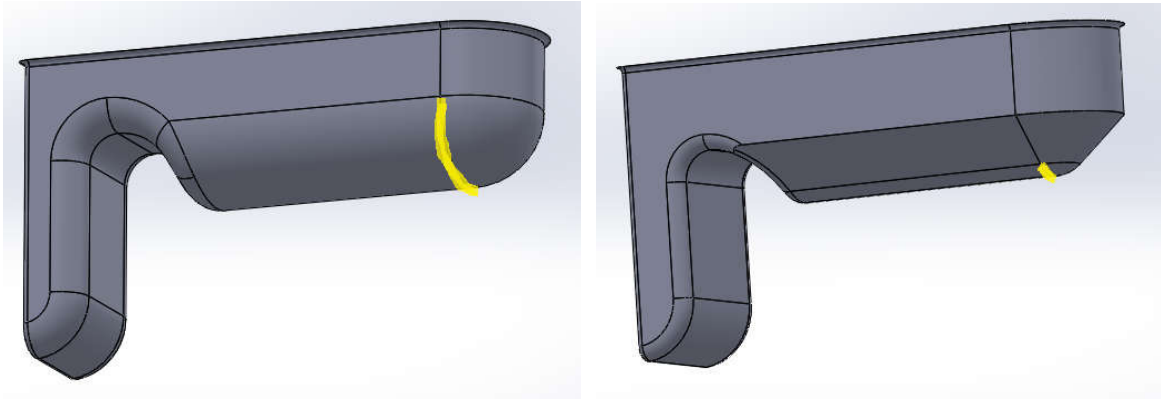


Figure 4-30 (a) The left image shows a pressure point with a full round surface. (b) The right image point that has a chamfered tapering

In addition to varying the shape of the pressure point, the dimensions were also varied. The force application surface of the pressure point itself, along with the side piece to line up with the styloid process (called the marker), were shortened on the chamfered pressure point model. These dimensions are shown in Figure 4.31 below.

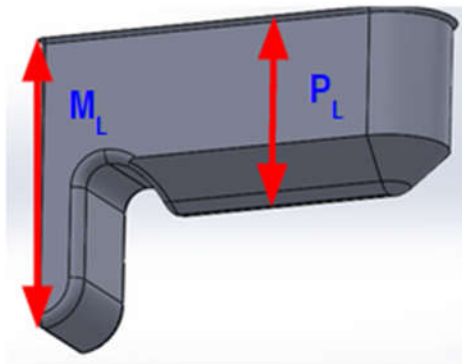


Figure 4-31 Image of pressure point with dimensions labeled. PL represents the pressure point length and ML represents the styloid process marker length

A few different pressure points were modeled and Solidworks stress simulations were run to analyze the differences in maximum Von Mises stress and maximum displacement of the part. As seen in Table 4.5, we found that as the pressure point length and marker length decrease, the max displacement decreases as well.

Table 4-5 Table that displays the difference in in max displacement when the pressure point and marker lengths are changed

Pressure Point Length (in)	Marker Length (in)	Max Stress (Von Mises) (Pa)	Max Displacement (mm)
0.75	1.25	1.623x10 ⁷	1.615 x 10 ⁻²
0.5	1	1.595 x 10 ⁷	1.484 x10 ⁻²
0.5	0.75	1.548 x 10 ⁷	1.48 x10 ⁻²
0.25	0.75	1.697x10 ⁷	1.399 x 10 ⁻²
0.25	0.5	1.587x10 ⁷	1.394x10 ⁻²

These simulations were run with a force of 550 N per face. For example, at a pressure point length of 0.75 inches and a marker length of 1.25 inches, the maximum displacement is 1.615 *10⁻² mm. When the pressure point length is 0.5 inches and the marker length is 1 inches, the max displacement is 1.484 *10⁻² mm. Finally, at a pressure point length of 0.25 inches and a marker length of 0.75 inches, the max displacement is 1.399 *10⁻² mm. The ideal pressure point dimensions were determined to be 0.5 in for the pressure point length with a 1 in long marker. The pressure point piece was shortened slightly to reduce the maximum stress and displacement values but was not shortened below 0.5 to allow for the skin on the wrist to compress without the supporting block of the pressure point to contact the wrist. The marker length was found to have a minimal effect on the stress and displacement values and was set to be one inch to conform to wrist geometry.

Material Reductions

Even radiolucent materials show up on the CT scan to some extent. Since the volume of material in the imaging region is as thick as it is, variations to reduce material while maintaining strength were considered. A few initial designs modeled were circular honeycombs, diagonal fins, cutouts in the part, and reducing thickness in the middle of the part.

The reduced thickness model was done so by effectively building the pressure point up into the support piece and leaving the maximum thickness around the rod holes. This model is shown in the top left of Figure 4.32 below. Another material reduction consisted of inserting cutouts into the design, as shown in the top right of Figure 4.32. This model reduced the material

that the x-rays would have to image through when coming from an angle.

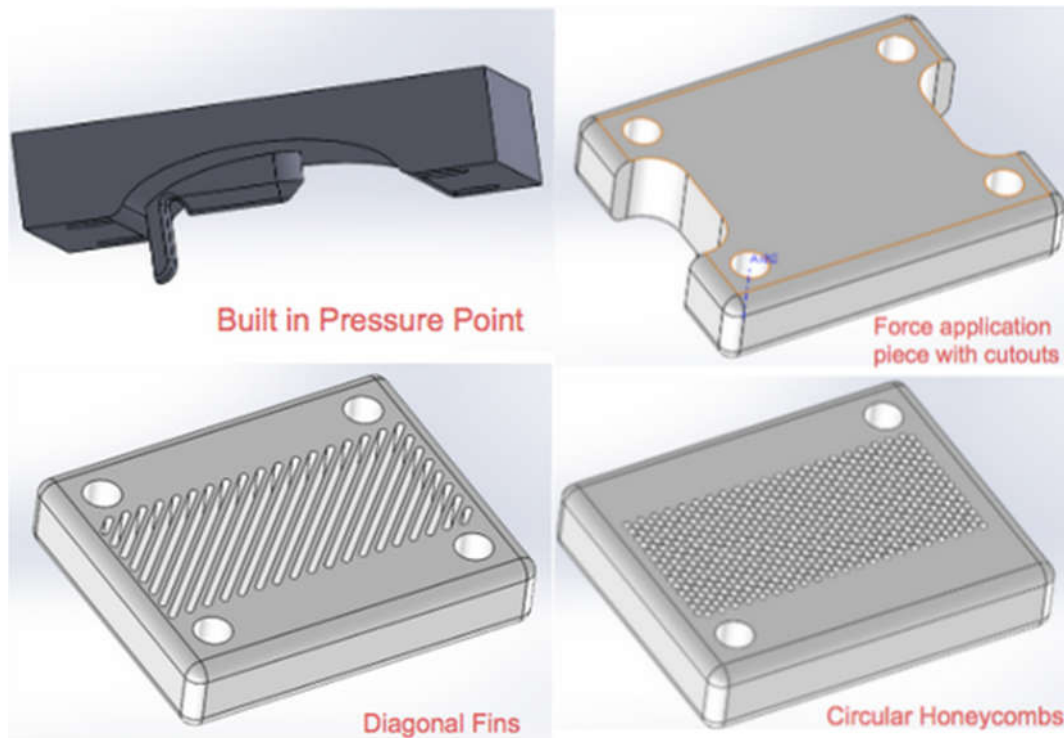


Figure 4-32 CAD models of material reductions in the force application piece.

Another potential material reduction consisted of inserting fins to the default model. As seen in the bottom left of Figure 4.27, fins consist of material cutouts that run diagonal to the base. Finally, honeycombing is another technique that can be implemented to reduce the amount of material. In honeycombing, circular and hexagonal cutouts run throughout the base of the material, as seen in the bottom right of Figure 4.27.

Table 4.6 displays differences in the volume of material in the imaging region, the max stress (in MPa), and the max displacement (in mm) for various material configurations. For this simulation, a force of 550 N was applied and Torlon 7130 was used as the material. Table 4.6 sorts the configurations that had the greatest maximum stress in order from highest to lowest. Two models were also made, which combined features. One model combined the circular honeycombs and the cutouts, and another was a circular honeycomb model, which decreased the overall part thickness to 0.5 in.

Table 4-6 Table that displays the difference in max stress and max displacement when the material configuration is changed

Reduced Material Configurations	Volume of Material in Imaging region	Max Stress (Von Mises) (MPa)	Max Displacement (mm)
Honeycomb + thinner	3.94	1.09(10 ⁵)	4.49(10 ⁻²)
Honeycomb + cutouts	5.10	6.60	1.37(10 ⁻²)
Built-in Pressure Point	8.13	5.79	9.40(10 ⁻³)
Honeycomb (Circular)	6.88	3.705 x10 ⁶	7.894 (10 ⁻³)
Fins	6.69	3.42	8.50(10 ⁻³)
Cutouts	8.46	3.08	9.32(10 ⁻³)
Default	11.03	3.08	5.94(10 ⁻³)

As seen in Table 4.6, the default material configuration had the lowest maximum stress (of 3.08 MPa) when a force of 550 N was applied and the lowest maximum displacement value (of 5.94(10⁻³) mm) because it had the highest density of material. Although a lower maximum stress and displacement occurs in the default configuration, the model would also have the highest net cost and more importantly could cause the image to be unclear because of how thick the part is. The combination of honeycombing with other material reductions (decreasing thickness and adding cutouts) were not pursued any further due to poor max stress and displacement values. It was also determined that this level of material reduction was not necessary.

Out of the four models shown above, the circular honeycomb and the fins had considerably lower volumes than did the cutouts and the default model. The honeycomb model optimized the decreased volume of the material while still minimizing the displacement. Honeycombing was determined to be the optimal method of material reduction for this application. In the following paragraphs, a more detailed description of honeycombing is described.

A cellular solid is any solid, which is comprised of a repeating pattern of a cell. The cells share walls with their neighboring cells. They can come in many shapes and in two-dimensional or three-dimensional patterns [54]. Honeycombing is one of many types of cellular solids, which has a two-dimensional hexagonal pattern of close packed cells, as modeled in the honeycombs of a bee. Honeycombs are the simplest and most common of cellular solid patterns. Hexagonal honeycombs are known to minimize density of material without compromising the strength of the

solid. Hexagonal honeycombs are proven to be stronger than other cell shapes, such as triangles or star-shapes. [54] [55]. The effective elastic modulus of the cellular solid can be determined based upon the ratio of the length of the cell to the thickness of the material in between cells as depicted in Figure 4.33, below.

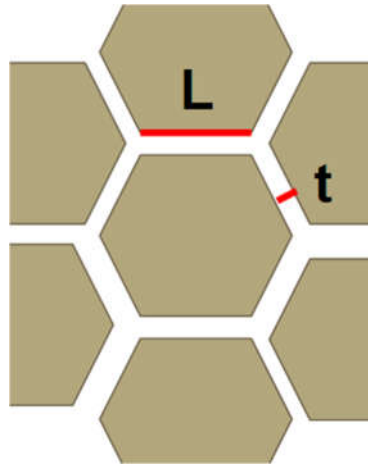


Figure 4-33 Image depicting the length of a cellular solid to thickness of the material in between cells

The elastic modulus for a regular hexagon can be calculated using the formula:

$$E = (4/\sqrt{3}) (E_s)(t^3/l^3)$$

Where, E_s is the elastic modulus of the solid material, and t and l are the cell dimensions as shown in the Figure 4.28 above [56]. Using these calculations, with a $t:l$ ratio of 1, the elastic modulus of the cellular solid would increase. With a ratio of 1:2, the elastic modulus would be about 30 percent of the elastic modulus of the solid material.

The plastic stress of a honeycomb structure is the stress value at which the cells begin to collapse. This is calculated using the formula [56]:

$$\sigma_{pl} = \frac{2}{3} (t^2/l^2)\sigma_y$$

Where σ_y is the yield stress of the material. Because of the $\frac{2}{3}$ fraction, a 1:1 ration for $t:l$ will result in a plastic stress lower than the yield stress.

A hexagonal honeycombed model was determined to be ideal for material reduction and manufacturable via 3D printing. Despite this, 3D printing a honeycombed material was not pursued because the voids in the material would not allow for enough layers of carbon fiber reinforcement to be placed between the honeycombs.

4.3.14 Evaluating Devices to Measure the Applied Force

We also evaluated which devices would be best in measuring the mechanical force that is applied. We considered three different instruments to measure the force, including a strain gauge based load cell, a piezoresistive force sensor, and a beam load cell. In this section, we discuss the benefits and drawbacks of each force measuring instrument as well as the design matrix that we utilized in evaluating these instruments.

Strain Gauge Based Load Cell

As the name implies, a strain gauge load cell contains a strain gauge, which is a device that uses electrical conductivity to measure the strain that occurs. A common type of strain gauge consists of rectangular pieces of foil with wires that lead to electrical cables, as shown in Figure 4.34.

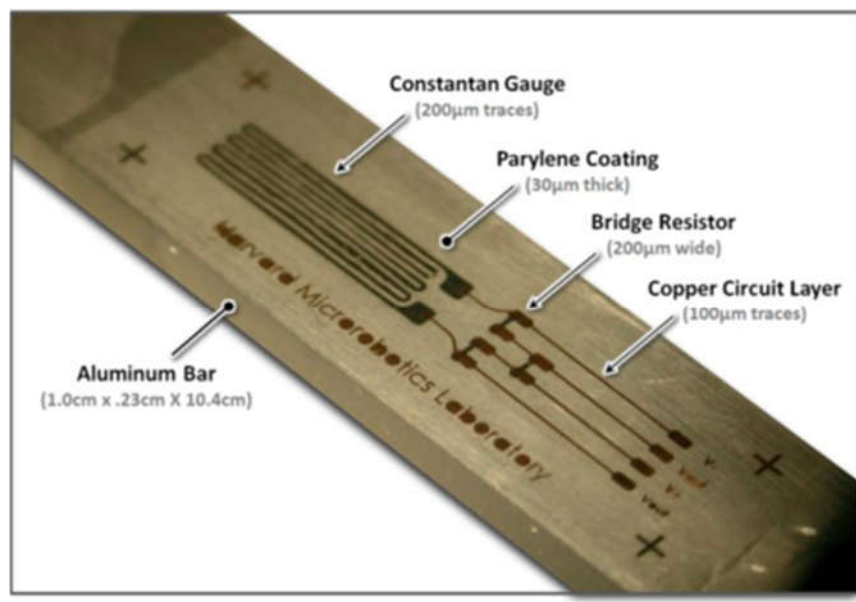


Figure 4-34 Schematic of a digital strain gauge [47]

The strain gauge is attached to the object of interest via a suitable adhesive. When an object, whose strain we are measuring, is deformed, the foil is deformed and this causes the foil's electrical resistance to change. Then, a Wheatstone Bridge is utilized to measure the resistance change, and a quantity known as the gauge factor relates the resistance change to the strain. The strain represents the change in length divided by the original length.

In a strain gauge load cell, a force is converted into a measurable electrical output. Additionally, in this load cell, strain gauges are bonded onto a structural member when a weight

is applied, and four strain gauges are typically used to obtain sufficient sensitivity. When a weight is applied to the strain gauges, the strain changes the electrical resistance of the gauges in proportion to the load. Strain gauge based load cells offer accuracies within 0.25% of the full scale (FS) measurement and are suitable for a variety of applications [48]. Other advantages include: they can be used for static and dynamic measurement, involve no moving parts, and can accommodate a wide range of force measurements. However, a disadvantage is that calibration can be a tedious procedure.

Piezo resistive Force Sensor

A piezo resistive force sensor measures force directly, in comparison to a load cell, which utilizes a strain gauge to measure the applied force. In this instrument, the applied force compresses two layers of a flexible, piezo resistive ink together. This compression results in a proportional change in electrical signal, and this device acts as a force sensing resistor in an electrical circuit. Furthermore, the resistance can be read by utilizing a multimeter and is inversely proportional to the applied force. An image of a piezo resistive force sensor is shown in Figure 4.35.



Figure 4-35 Piezo resistive Force Sensor [49]

An advantage of this type of sensing device is that it is durable and can be used in a wide variety of environments. Furthermore, they are small and relatively low in terms of cost (around \$20). These sensors can also be attached to many surfaces and allow for ease of integration. However, a disadvantage is that these sensors have a lower accuracy in comparison to strain gauge based load cells. For example, one piezo resistive force sensor found online offers an accuracy of $\pm 2.5\%$ within the full-scale measurement [50]. Additionally, calibration is also needed in this method, and piezo resistive force sensors usually are only able to measure forces up to approximately 100N. The amount of force that would need to be applied for an intermediately healed fracture is up to 550 N.

Beam Load Cell

Beam load cells are a type of strain gauge load cell that can convert an electrical signal to a measurable force. A beam load cell contains a metal spring element, which is deformed elastically when a weight acts upon it. This elastic deformation is converted into an electrical signal via a strain gauge, and Figure 4.36 depicts an image of a beam load cell.



Figure 4-36 Image of a beam load cell. [51]

Beam load cells can measure forces from several Newtons up to approximately 2940 N, which is more than the required amount of 550 N. Additional advantages of these load cells include: they offer a high accuracy of $\pm 0.030\%$ within the full-scale measurement and are relatively low in terms of cost (around \$40). However, a disadvantage of beam load cells is that they can be larger in comparison to strain gauge based load cells. For example, one beam load cell found online had dimensions of 1.57" X 5.91" X 1.38" in comparison to a strain gauge load cell, which had dimensions of 1.7" X 1.5" X 0.12". Beam load cells also require calibration, which can be a tedious procedure.

Table 4.7 displays a Pugh Matrix that we utilized in evaluating the different force measuring devices. We compared these devices based on the following criteria: accuracy, space constraints, range of force, ease of use, and cost effectiveness. Rankings were assigned on a scale of 1 to 3, with 3 being the most important, and 1 the least important.

Table 4-7 Pugh Matrix for the force measuring devices

	Importance of the Requirement	Strain Gauge Based Load Cell	Piezo resistive Force Sensor	Beam Load Cell
Space Constraints	3	3	3	3
Range of Force	3	3	2	3
Accuracy	2	3	2	3
Ease of Use	2	2	2	2
Cost Effectiveness	1	3	3	3
Totals		31	28	31

The first requirement considered was the ability of the device to fit in a limited space, and this requirement was rated as a 3 since it is essential for the device to fit inside the scanner opening. The strain gauge based load cell and the piezo resistive force sensor were rated as a 3 because they can fit in a small space. Although beam load cells are quite large, they were rated as a 3 because they would still be able to fit within the CT scanner without any difficulty.

Furthermore, we considered the range of force that the device needs to be able to measure. This requirement was rated as a 3 since it is essential that the device can measure a sufficient range of forces to determine which state the healing fracture is in. The strain gauge based load cell and beam load cell were rated as a 3 because they can measure forces in the range of several Newtons to 550 N. The piezo resistive force sensor was rated as a 2 since this device generally measures forces from several Newtons to 100 N.

As seen in Table 4.7, accuracy was rated as a 2 because it is important for the device to measure close to the actual force being applied to the distal radius fracture. This requirement was also rated as a 2 since it is less important compared to the range of force the device can measure and the space constraints. We rated the strain gauge load cell and beam load cell as a 3 because these instruments offer accuracies within 0.25 % of the full scale (FS) measurement. The piezo resistive force sensor was rated as a 2 because this device offers accuracies within 2.5% of the full-scale measurement.

We also analyzed the ease of use of force measuring instruments. This requirement was ranked a 2 since physicians/technicians need to be able to operate the device in a reasonable duration of time. The strain gauge based load cell, piezo resistive force sensor, and beam load cell were all rated as a 2 because it would be equally difficult for physicians/technicians to learn how to use these devices. While these devices are relatively easy to use, they do require calibration, which can be time consuming.

The last requirement considered was the cost effectiveness of the force measuring devices. Like the design rubric for the tensile loading device, this requirement was rated as a 1 because of additional funding available for the project. We decided to rank the strain gauge based load cell and piezo resistive force sensor as a 3 since these devices are relatively inexpensive (around \$10-20). Beam load cells are also affordable and cost approximately \$10-15 or more to measure a force of 490 N or greater.

As seen in the design matrix, the strain gauge based load cell and beam bending load cell performed the best and had a total score of 31. Some of the advantages of these force measuring devices include their ability to fit in a limited space and measure a wide range of forces. These load cells are also relatively easy to use, can measure forces within 0.25% of the FS measurement, and are affordable. We decided to use a Button load cell and a Miniature Beam Load Cell by Futek since they were available for free from a previous MQP project. In Chapter 5, the results for testing the load cells will be presented.

4.4 Design Calculations

This section contains the preliminary calculations to determine the ranges of force needed to produce displacements detectable by the HR-pQCT scanner (XtremeCT, Scanco, Switzerland) in a healing human distal radius.

The minimum displacement detectable is defined as 82 microns, the voxel resolution of the micro CT scanner used. Ideally, the displacement should be twice this distance, 164 microns, to produce movement visible in at least two voxels, thus improving the sensitivity of the image to a displacement in the bone (due to increasing the ratio of displacement to resolution scale). The following preliminary calculations use a standard linear elastic solid model to calculate fracture displacement in a simplified human forearm model when subjected to external loading.

In this one-dimensional model, a spring with stiffness constant K is displaced by a distance L due to the application of a force F .

Linear Elastic Spring Model:

$$F = K L$$

Using simple stress analysis, the 2-dimensional model accounts for force distribution across cross-sectional areas of the bone and soft-tissue.

Stress Analysis Model:

$$F = \sigma A = E \epsilon A$$

Here, σ represents the stress (force divided by area), A is the cross-sectional area, E is the elastic modulus of the bone, and ε is the strain, which is defined as the change in length divided by the initial length.

The results are presented below and we utilized the following properties of bone in the calculation:

Soft tissue radius is 2.5 cm, the radius of the bone is 2 cm, and bone callus radius is 2.25 cm [51].

An image of the properties used in the calculation is shown in Figure 4.37.

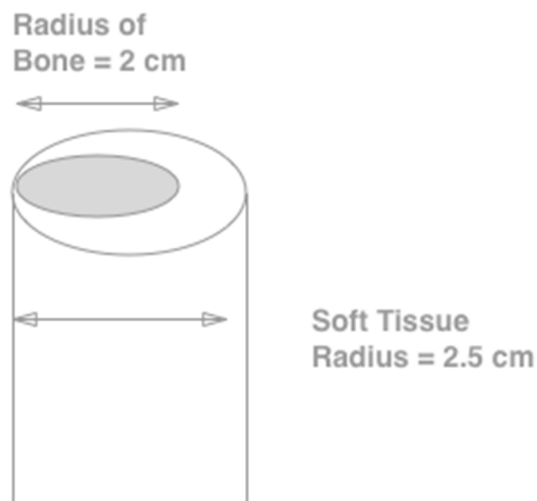


Figure 4-37 Image of the radius of bone and soft tissue

These calculations were performed iteratively for a healing complete fracture using the different elastic modulus values known for various healing stages [52].

Fresh, Complete Break:

$$E = 1.23 \times 10^3 \text{ Pa} - 3.15 \times 10^3 \text{ Pa for that of skin/muscle:}$$

$$\mathbf{F = <1 \text{ N}}$$

Early Union:

$$E = 5\text{-}10 \text{ MPa} \rightarrow \text{Woven Bone}$$

$$\mathbf{F = 7\text{-}15 \text{ N}}$$

Intermediate Healing:

$$E = 100\text{-}500 \text{ MPa}$$

$$\mathbf{F = 100\text{-}550 \text{ N}}$$

Good Union:

$$E = 15\text{-}20 \text{ GPa}$$
$$F = 16\text{-}22 \text{ kN}$$

It is shown that in the first three stages the force needed to displace the fracture increases by six orders of magnitude. The device will need to be able to apply a force from a few Newtons to around 550 N. It is anticipated that in the later stages of healing, when the bone is well joined, that we will not be able to displace the fracture without injuring soft tissue. At this stage, the bone will no longer be considered at risk for healing complications, and will likely not need further mechanical testing for appropriate treatment.

The following calculations were completed to determine the amount of force that would need to be applied to the distal radius. These calculations assume that the bone is a linear elastic, isotropic solid, which means that it fully recovers all deformation due to loading and has the same physical properties when measured in different directions. Additionally, the bone was modeled as a circular hollow beam to solve for the force. The equation for the deflection at any point is:

$$d = \frac{Fx^2}{6EI}(3L - x).$$

In this equation, F represents the force acting on the bone, L represents the length of the bone, E represents the bone's modulus of elasticity, x is the depth of the fracture, and I represents the area moment of inertia of the bone's cross section. As seen in Figure 4.31, a tensile force is being applied to both sides of the bone. Therefore, F is equal to 2T, in which T represents the tensile load acting on the bone. It is assumed that the displacement is small such that the angle of the broken surfaces is negligible. By substituting 2T into the equation, and by setting L = x, the equation becomes:

$$d = \frac{(2T)x^2}{6EI}(3x - x).$$

Solving for the tensile force, the equation becomes:

$$T = \frac{(3d)EI}{2x^3}.$$

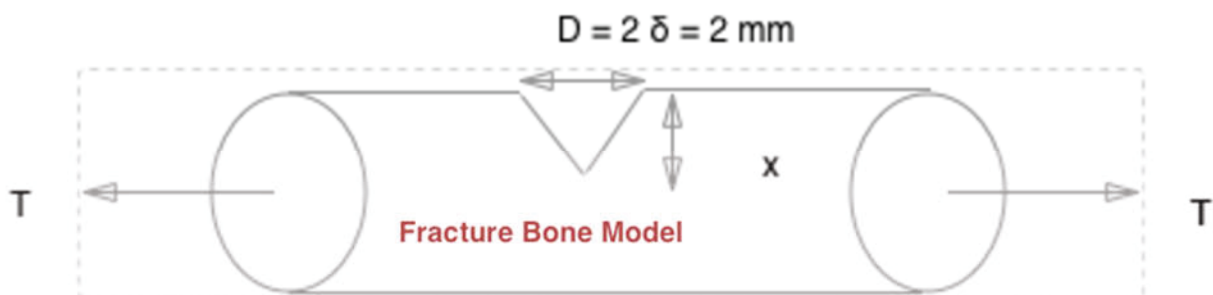


Figure 4.31: Schematic of the tensile force (T) that is applied to a fractured bone. In this model, the deflection (d) is equal to 2 mm, and x represents the length of the fractured bone

The area moment of inertia is a half-circle about the flat portion, and has the following equation:

$$I = \frac{\pi r^4}{8}$$

In this equation, r represents the radius of the distal radius and by plugging in the area moment of inertia into the deflection equation, the formula reduces to:

$$T = \frac{(3d)E (\pi r^4)}{16x^3}$$

Through background research, we found that the radius r of the distal radius is approximately r = 1.59 cm or 0.0159 m, the modulus of the healthy bone is approximately E = 10.5 GPa or 10,500 (10⁶) Pa, and the maximum deflection that can be applied to bone is approximately d = 2 mm [53].

By substituting these values into the equation

$$T = \frac{(3d)E (\pi r^4)}{16x^3}$$

it is found that the tensile force is approximately T = 197(10³) N or 197 kN

We also solved this equation for the cases in which the deflection d = 1 mm and d = 0.165 mm (165 μm).

For the case in which d = 1 mm, the required force would be approximately 98 kN.

For the case in which d = 165 μm, the required force would be approximately 16 kN.

Table 4.8 shows a summary of the results that were found via the calculations, and the amount of force needed to displace a healthy bone (with an incomplete fracture) is in the kN range.

Table 4-8 : Summary of the Tensile Forces required to displace healthy bone.

Deflection	Tensile Force Required
0.165 mm (165 μm)	16 kN
1 mm	98 kN
2 mm	197 kN

Here, it should be noted that it is likely not possible to apply the magnitude of force necessary to displace an incomplete fracture through the tensile method because these forces must be applied through the overlying soft tissue, which is likely to be damaged by this level of force.

The main advantage of the bending stress design (in comparison to the tension design) is that it can displace unusual fracture geometries and has mechanical advantage from the bending force application geometry; this mechanical advantage allows for higher internal bone forces with lower external soft tissue forces at the force application points. Deflection calculations for this design are presented in the next section.

4.4.5 Bending Design Force-Displacement Calculations

Upon selection of the three-point bending design, the force-displacement-stiffness calculations were performed to calculate the needed forces for the same displacements at the above prescribed healing levels. The force F applied equidistance between two supports placed a distance L apart required to displace a beam a distance D is given by the following equation:

$$F = 48*DEI/(L^3)$$

Where I is the bending modulus:

$$I = \pi*(r^4)/4$$






for intermediate stages of healing with a full circular callus cross-section and

$$I = \pi*(D^4 - d^4)/64$$

for initial and final healing stages with a cylindrical cross-section, D is outer diameter, d is inner diameter.

The force levels required to displace the bone in the final device design and predicted discomfort with the padded chamfered pressure point are Presented in Table 4.9

Table 4.9 Summary of calculations for 3 point bending forces necessary for a fractured distal radius at various stages of healing

Bone healing stage	Fracture callus modulus [7]	Cross section assumed	Force range (N)	Projected discomfort level
Fresh break	< 1 Pa		< 1	1
Early union	5-10 MPa		9 - 150	1-2
Intermediate union	15-20 MPa		28 - 449	1-6
Full union	100-500 MPa		921 – 11000	10
Healthy bone	18-20 GPa		> 50000	10

4.5 Design Conclusions

As mentioned in Section 4.3 of this report, design matrices were used to evaluate the loading type, loading mechanisms, hand and elbow gripping options, and load cell that will be used.

Another key decision made during this phase of the project was whether to select the Tension design that utilizes a screw drive, the 3-point bending design, or to pursue both options and see which one performs better. We decided to pursue the design that applies a 3-point bending moment for a multitude of reasons. Table 4.10 outlines the pros and cons of each design.

Table 4-10 Pros and Cons of Tension and Bending Designs

	Pros	Cons
Bending	<ul style="list-style-type: none"> ○ Simpler Design ○ Less moving parts ○ Offers a mechanical advantage ○ Left/right compatible ○ More Affordable 	<ul style="list-style-type: none"> ○ Difficult to adjust loading while inside the scanner ○ Will not work with a cast
Tension	<ul style="list-style-type: none"> ○ Worm screw and operation is outside of field of view and more easily accessible ○ Different L/R accessories 	<ul style="list-style-type: none"> ○ Difficulty in gripping ○ More complex design

As seen in this table, the bending design involves fewer moving parts and is much simpler in comparison to the tension design. This can improve the device's repeatability and ability to remain rigid when a mechanical force is applied. The bending design also offers a mechanical advantage via 3-point bending, allows for easy right/left (R/L) changeover, and is more affordable. A key limitation of the bending design is that the patient will need to remove his/her cast to use the device, and it can be difficult to adjust loading while inside the scanner.

The tension design also offers advantages, such as R/L compatibility and the ability to adjust the loading easily. The drawbacks to the tension design include difficulty in gripping the hand and elbow mechanisms and relative design complexity that involves more moving parts. This can affect the ability of the device to apply a repeatable load and to remain stable during force application. Although loading in tension was initially preferred due to the possibility of the cast remaining on the arm during the procedure, it has been determined that this is outside the scope of this project since preliminary evaluations showed that gripping the casted hand securely enough is extremely difficult and will likely take longer to develop than this project timeline allows.

Selecting the bending allows us to move more quickly into the next stage of prototyping because the simplicity of the design does not require significant additional modifications, whereas the tension design will require more time to further develop. Due to the time constraints of this project, it is imperative that a fully functional prototype is machined sooner to allow for cadaver testing to be done to verify that the loading concept and bone displacement methods work as intended. Some slight design updates for the next prototype will include a less angular design. This will improve comfort and maximize the use of the scanner's cylindrical field of view. Hook and loop strapping will be added for arm security, and the load cell for force measurements. The geometry of the pressure point will be further evaluated to determine that the force is spread over a suitable area on the wrist and not directly to the ulna.

4.5.1 Material Selection

We ultimately decided to pursue 3D printing because it allows for faster production time. We also selected a plastic material that was easy to 3D print. Plastics that we selected from included PLA (Poly Lactic Acrylate), ABS (Acrylonitrile Butadiene Styrene), and Torlon. Recently, a 3D printer which can print using glass fiber materials has also become available. Finally, the last design requirement is that the device should not cost more than \$1000. In the design process (including testing and building the final prototype), the detailed budget breakdown is presented in the Appendix A. Future recommendations are to use Polycarbonate and Carbon fiber mats to provide maximum strength and fracture toughness.

Various materials were considered to determine which would be ideal. One important parameter in selecting a material was the flexural modulus, which indicates the resistance of a material to bending deformation. For example, a material with a higher flexural modulus deforms only slightly in response to flexural/bending loads. In our device, when a mechanical load is applied to the patient the device must not fracture or deform enough to impact the scan before achieving the necessary displacement. Another parameter that we considered was the cost, to keep the selling price of the device under 1000 dollars.

Materials which met the following specifications were considered: radiolucency, a flexural modulus greater than 3 GPa and a price less than \$80/kg¹. Several pure materials with these specifications were found in the CES Edupack database, as shown in Table 4.11, below.

Table 4-11 Properties of plastics that are not carbon fiber or glass reinforced

Plastics without glass	Full name of each plastic	Flexural modulus (GPa)	Price (\$/kg)
PLA (30% natural fiber)	Polylactic acid (30% natural fiber)	4.75	2.96
PLA (30% mineral, impact-modified)	Polylactic acid (30% mineral)	4.14	2.78
EVOH	Ethylene vinyl alcohol	4.1	7.68
PHA	Polyhydroxyalkanoates	4.05	6.5
PPS	Polyphenylene Sulfide	3.96	7
SAN	Styrene Acrylonitrile Resin	3.82	3.13
PLA (10% mineral, impact-modified)	Polylactic acid	3.5	3.37

Table 4.10 displays materials that met the specifications above including: PLA (30% natural fiber), PLA (30% mineral impact modified), EVOH, PHA, PPS, SAN, and PLA (10% mineral impact modified). The flexural modulus of these materials ranged between 3.5 - 4.75 GPa and the price ranged between \$2.78 - 7.68 / kg.

Carbon fiber reinforced plastics resulted in higher flexural moduli while maintaining radiolucency. Alternative fillers to carbon fiber filaments which increase strength are typically not

¹ A flexural modulus of 5 - 25 GPa is considered relatively high for plastics.

radiolucent, such as glass fibers. The carbon fiber reinforced plastics found include: PAI (Polyamide-imide, which is also known as Torlon), LCP (liquid crystal polymer), SPS (Syndiotactic Polystyrene), PARA (Polyarylamide), and PC (Polycarbonate); these materials are 30 % carbon fiber reinforced, and a table of properties for each of these plastics is shown in Table 4.12. The flexural modulus' of these materials is between 19.3 - 25.8 GPa.

Table 4-12 Properties for Carbon Fiber Reinforced Plastics

Plastic	Reinforcement	Flexural modulus (GPa)	Yield strength (MPa)	Fracture Toughness (MPa * \sqrt{m})	Price (\$ / kg)
PAI (Torlon)	30 % CF	19.9	143 - 157	5.12-6.42	60 - 80
LCP	30% CF	23.5-25.8	118-130	3.64-3.79	12.1-14.78
SPS	30% CF	19.8-20.5	118-130	1.40-1.51	12.8-15.2
PARA	30% CF	20.2-24.2	188-235	5.88-6.49	11.2-14.6
PC	30% CF	19.3-19.9	127-132	4.94-5.93	10.4-13.2

Another key material property that we considered during the design process was the fracture toughness, which describes the ability of a material containing a crack to resist fracture. This is a crucial parameter to ensure that the device will remain stable when a mechanical load is applied. As seen in Table 4.11, the carbon fiber reinforced plastics with the highest fracture toughness' were PARA (Polyarylamide), which had a fracture toughness of 5.88-6.49 MPa * \sqrt{m} , and PC (Polycarbonate), which had a fracture toughness of 4.94 - 5.93 MPa * \sqrt{m} .

Torlon was eliminated due to its a considerably higher price (\$60 - 80) in comparison to LCP (liquid crystal polymer), SPS (Syndiotactic Polystyrene), PARA (Polyarylamide), and PC (Polycarbonate). Table 4.13 displays detailed information on suppliers for carbon fiber reinforced plastics.

Table 4-13 Suppliers of Carbon Fiber Reinforced Plastics

Material	Supplier
PC 30% Carbon Fiber	RTP Company
LCP 30% Carbon Fiber	Calanese
PARA 30% Carbon Fiber	Solvay Specialty Polymers

SPS 30% Carbon Fiber	Dow Chemical Company
----------------------	----------------------

All the plastics in the above table were sold in pellet form for injection molding. 3D printing materials were also analyzed. Injection molded plastics are preferred due to their superior flexural modulus compared to 3D printed materials. Solid CF reinforced plastics have flexural moduli greater than bone, which is an important mechanical consideration when deflecting bone in later and stiffer stages of healing. For this reason, we recommend that the final device be manufactured through injection molded CF reinforced methods, using honeycombing to reduce material in the imaging region.

4.5.2 Manufacturing Technique Selection

Various manufacturing techniques were considered to develop the prototype. One manufacturing technique considered was injection molding, which is a process that involves melting the plastic in an injection molding machine and then cooling the plastic. Injection molding offers an array of advantages in comparison to other manufacturing techniques. As an automated process, most injection molding is performed by machines and robotics, which helps reduce the manufacturing costs. Injection molding allows for a large amount of detail in parts because of the high pressure that is applied during the molding process. Table 4.14 includes injection molding companies in the area.

Table 4-14 Table of injection molding Companies in the Worcester, MA Area

Injection Molding Companies	Location	Manufacturing Time
Applied Plastic Technology	Worcester, MA	At least 4-6 weeks
Lee Plastics	Sterling, MA	4 weeks + (polymer shipping time)
Plastic Molding Manufacturing	Hudson, MA	N/A

As seen in Table 4.14, lead times for injection molding materials are typically greater than four weeks. Therefore, due to time constraints, injection molding was not feasible for this prototype device. Instead, 3D printing will be chosen as a manufacturing technique. 3D printing in Onyx will be readily available through the Center for Advanced Orthopedic Studies, BIDMC and provided acceptable material properties. We also considering using carbon fiber reinforced PLA because it also offers a high flexural modulus.

4.6 Optimization

To develop a well-functioning device, we used design matrices, experimental testing, and took into consideration constraints in the project.

As described earlier, to select the loading type and mechanisms that would be utilized, we utilized a Pugh matrix. Several of the main requirements taken into consideration include: repeatability, ability to fit within the CT scanner, range of force that the design can apply, ease of use, and ergonomics. We selected the 3-point bending design because we think that this device will be able to apply a suitable and repeatable mechanical load. Based on CAD models, this design will be able to fit in the CT scanner (which has dimensions of 7.5" X 31" X 5.5").

Initially for the tension design, we performed experimental tests to select hand and elbow gripping components. The results of these experimental tests will be discussed more in the next chapter, and design requirements we took into consideration include the security and comfort that these parts will provide.

For the initial tension design gripping mechanisms, we selected components that can withstand higher forces and able to remain secure while a mechanical load is applied. We also implemented a design matrix to select the load cell that would be incorporated. Several key requirements taken into consideration include: space constraints, range of force, accuracy, and ease of use. The load cell was selected because it is accurate and can measure close to the upper portion for intermediate healing (550 N). It is also able to fit in a limited space and is relatively easy to use. Another design consideration evaluated is the type of frame the device should have. For the frame, we considered using bottom supports, single side supports, or a full cage support. We decided to choose the bottom supports because it will be able to fit well within the space constraints and it is the most affordable option in comparison to other types of frames. While a full cage support does offer more rigidity, this design will likely not be feasible due to space constraints inside the scanner. Ultimately, this design was abandoned due to difficulties with reproducibility and varying patient anatomy.

The updated three-point bending design was determined to be the most effective method of applying the displacement load. We considered what materials should be used in the design. We selected materials based upon radiolucency, cost effectiveness, and the ability to remain still when a mechanical load is applied. We initially decided to use PLA with carbon fiber reinforcement, which is a radiolucent and thermoplastic material. Advantages of this material include that it is environmentally friendly, available at a low to moderate cost, and it offers high flexural strength and reliable performance. A printer that can print glass fiber along with traditional

filaments became available however, and it was decided to use this method with threaded inserts to produce the first full prototype.

Bearing Ratio Considerations

Bearing ratio (BR) is the ratio of the total length of the slide bearing to the diameter of slide as shown in Figure 4.38. A bearing ratio of > 1.5 is required for smooth sliding at all speeds, and a bearing ratio of < 1 will induce mechanism binding even at slow speeds. For this device, bearing ratio represents the ratio of the distance between rod supports over the maximum rod separation. Here: $D = 3.75$, $L = 5.5$ in (entire rod length) which cannot exceed ~ 6.5 in due to scanner dimensions leading to a $BR = 1.47$. This is slightly under the ideal 1.5, but not a problem due to the slow speeds indicated for this application.

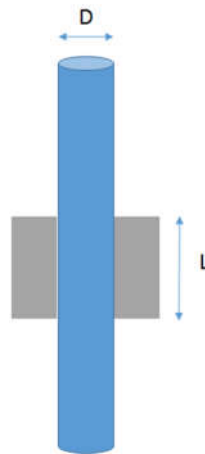


Figure 4-38 Bearing ratio of a sliding mechanism.

Upon consultation with WPI Machinist James Loiselle, the need for validation of the drive mechanism was identified. A design principle from kinematics known as the bearing ratio for sliding parts may cause problems with the smooth translation of the loading mechanism. The bearing ratio of the current design was assessed, determined to be within the acceptable limit, and sliding guide rods were added to the loading mechanism for improved stability.

4.6.1 Drive Mechanism Resolution Improvement

The initial loading mechanism calibration tests indicated that once secure compression was achieved, it took only $7/24$ of a turn, about 105, of the $\frac{1}{2}$ with 13 inch threaded rods to produce the maximum force rating of the load cell of approximately 550 N. This means that there is very little control in the loading range (in terms of Newtons per degree) that is available to the

technician operating the device in a clinical setting. Lack of control of the loading mechanism could lead to inappropriate or damaging loads on a patient, so this problem was corrected.

Assuming a fully rigid, non-conforming mechanism, and complete force transfer, the following calculations were made to quantify this effect in engineering terms presented in Table 4.15.

Table 4-15 Improved Thread Pitch Force Resolution Calculations

	½ - 13 thread	½ - 40 thread
Number of turns total range	0.29	11.67
Vertical displacement per turn	1/13 in	1/40 in
Average force per degree turn	21.9 N/deg	0.07 N/deg
		>300x higher resolution

At 13 TPI (turns per inch), each full turn corresponds to 1/13 of an inch of vertical displacement in the loading mechanism, which is equivalent to approximately 0.076 inches/turn so 0.2917 inches corresponds to an average of 21.9 N/degrees of rotation. At 40 TPI however, 0.2917 inches corresponds to 0.07 N/degrees of rotation, more than 300 times increase in resolution.

It should be noted that this curve is best fit as a power curve, so averages are used to describe the whole range in a comparative fashion. Additionally, the mechanism is calibrated without a wrist phantom, and therefore deflection can have attributed only to the loading mechanism. It is important to note that the deflection is not representative of a human, who is expected to exhibit greater compliance. The calculations above display a significant improvement in drive distance resolution. This improvement improves device performance capabilities and decreases the risk of harm to the patient.

Conclusion

Above are presented the design alternatives considered in the development of the device and evolutions during the first three quarters of the project. The current device design offers optimized performance and manufacturability. Recommendations are also made for a next-stage injection molded part.

Chapter 5 : Design Verification

In this chapter, we have written experimental procedures and results to confirm that all elements of the device are operating properly. We have written protocols and results for testing the hand and elbow gripping mechanisms, for determining the field of view (FOV) in the CT scanner, and for testing the prototype loading mechanism. IRB comfort testing and cadaver testing protocols are also provided in this chapter. Experimental testing is important because it allows us to determine if each individual component of the device is functioning well. Full data sets are available in the Appendices.

5.1 Experimental Testing Phase

The bending design will need to be evaluated for how well it meets the prescribed design requirements. Some of these requirements will be evaluated via the literature review or calculations while others will be evaluated through tests. Table 5.1 below details the list of design requirements and what type of evaluation will be needed.

Table 5-1 Experimental requirements

Experimental Requirements	Type of requirement
1. Reliability/ repeatable force application	Loading
2. Force adjustment ability	Loading
3. Produces displacement in a safe range for healing bone and max force	Loading
4. CT Image Clarity	Imaging
5. Ergonomics/ Comfort	Comfort
6. Pain Level for user is 3 or below	Comfort
7. Device Rigidity and arm stability	Materials requirement

As seen in Table 5.1, several tests needed to be completed to evaluate the designs and select a final version. The tests that to be completed include:

1. **Repeatability of Loading** - This test determines how repeatable the bone loading is and determine if the device can successfully load the bone. The test will be performed using the tension and bending devices to load a cadaver wrist 10 times and ensuring that the same force and results are seen each time within the tolerances of the device and imaging system.

2. **Force Adjustment Abilities** - The force of the device needs to be adjustable up to 550 N to adapt to the changing elastic modulus of bone as it heals. To evaluate the force adjustment abilities of each design, we tested the 3-point bending design.
3. **Production of a necessary displacement** - This test was conducted to show that the loading can produce a displacement, which is measurable on the CT scanner. This was done by simulating use of the device on a cadaver model. A fracture was placed in an avian model and we will measure the amount that the device displaces when mechanical loads are applied.
4. **CT Image Clarity and imaging size-** To ensure that the device stays stable and allows for a clear image during the procedure, a test was performed by placing the device inside the scanner and evaluating images for clarity. We could determine the imaging size of the CT scanner, which is a maximum of 126 mm (4.96 inches) in diameter and 150 mm (5.91 inches) in length.
5. **Ergonomics / Comfort** - The device needs to be comfortable and well adapted to the geometries of the arm for patient comfort, image clarity, and reduction of motion artifact during imaging. We tested for patient comfort by having team members try on the device, and reporting the level of pain when using the bending design.
6. **Pain Level Caused by the Device** - This test was done to determine how painful the device is to the patient. The test will be conducted on team members and potentially other WPI students. The force was applied to the distal radius outside of the CT scanner. The subject was asked to rate how painful the experience is on a pain scale of 1 to 10, with 1 feeling like a gentle touch, and 10 being unbearable pain. Since the subjects have healthy bones, the level of pain experienced by the patient is lowered to ensure the worst-case scenario. Therefore, we looked for a pain level of 3 or below for those with healthy wrists.
7. **Device Rigidity and Arm Stability:** The device and the patient's arm need to be able to remain in place while a mechanical load is applied to ensure sufficient imaging clarity. To test for arm stability, we evaluated how much the device moves when a force is applied to an avian bone. We evaluated how much the patient's arm moves inside the scanner.

The following sections of Chapter 5 describe the testing protocols and results for evaluating these experimental requirements.

5.2 Testing Procedures for the Hand and Elbow Gripping Mechanisms

During this initial testing phase, we performed experimental tests for the hand and elbow gripping mechanisms. The goals of these tests were to:

1. Fabricate the gripping mechanisms
2. Assess subject discomfort in use of mechanisms
3. Assess slip potential of each mechanism
4. Assess load bearing potential of each mechanism
5. Gather practical experience and information on refining each mechanism design and implementation

5.2.1 Testing procedure for the hand

The experimental steps for testing the hand are as follows:

1. Lay the subject face down on the table with the arm to be tested extended at a right angle to the body.
2. Position the subject so that the inside of the elbow and the humerus are supported by the table with the forearm and hand hanging freely off the edge of the table. Place foam padding under the upper arm and shoulder for comfort.
3. Place foam padding around the hand peg.
4. Place and secure cardboard of about 2 cm in thickness around the hand to mimic cast contribution.
5. Apply the gripping mechanism.
 - a. For the hook and loop finger brace: wrap fingers and thumb around padded peg, secure fingers by wrapping around the phalanges where the fingers meet the palm, and by wrapping a second strip around the tips of the fingers and the metacarpals, as shown in Figure 5.1.



Figure 5-1 Image showing how hook and loop is applied to the hand

- b. For athletic tape: wrap fingers as above, but using athletic tape instead of hook and loop.
6. Ensure that the subject fully relaxes the hand and forearm.
7. Secure the gripping mechanism, apply sufficient binding force until the mechanism seems securely tightened and not prone to slipping
8. Draw a slip measurement line with a washable marker or pen. The line is to be drawn on all portions of the skin at the edges of the gripping mechanism.
9. Load the gripping mechanism by attaching the hanging weights to a string connected to the loading contacts on the hand gripping mechanism.
10. Record the applied load and measure the slip with calipers; increase the load gradually and repeat.
11. Continue to load the gripping mechanism and record slip until the mechanism fails or the subject reports a pain level of 5 on the 1-10 self-assessed pain scale.

NOTE: the entire hand and forearm is assumed to be in tension of equal magnitude to the weights hanged from the loading mechanism, and the weight of the arm and hand is to be neglected.

Figure 5.2 displays a drawing of the testing setup that we utilized in evaluating the hand gripping mechanisms. We measured the slip by drawing a line on the skin at the edges of the gripping mechanism in the unloaded position. Then, we measured the displacement change from the unloaded condition from the line on the skin to the edge of the mechanism.

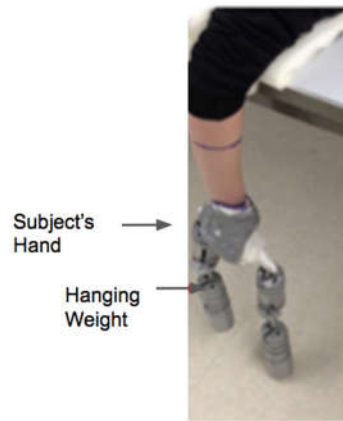


Figure 5-2 Image showing how hook and loop is applied to the hand

5.2.2 Testing Data for the hand

We performed experimental trials for evaluating the hand gripping mechanisms. Figure 5.3 displays an image for testing hook and loop.

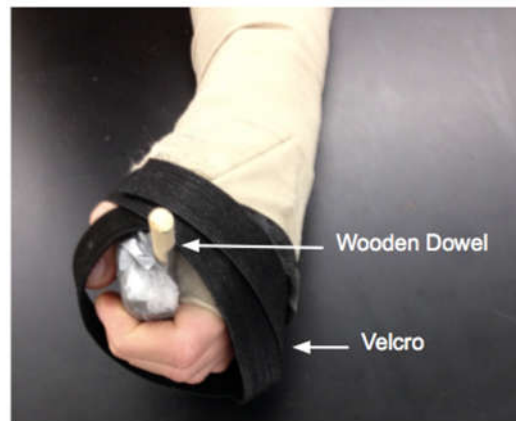


Figure 5-3 Image showing how hook and loop is applied to the hand

During testing, we quickly found that hook and loop was unable to properly grip the hand. In one mini experiment, a team member pulled the dowel to assess the security that the mechanism provides, and the subjects fingers would quickly slip. Based on qualitative testing, it seemed that the hook and loop did not sufficiently restrain the patient's hand. We therefore decided to pursue the Athletic Tape Finger Brace, and an image of this brace taken during device testing is shown in Figure 5.4. More detailed data is shown in Appendix F.

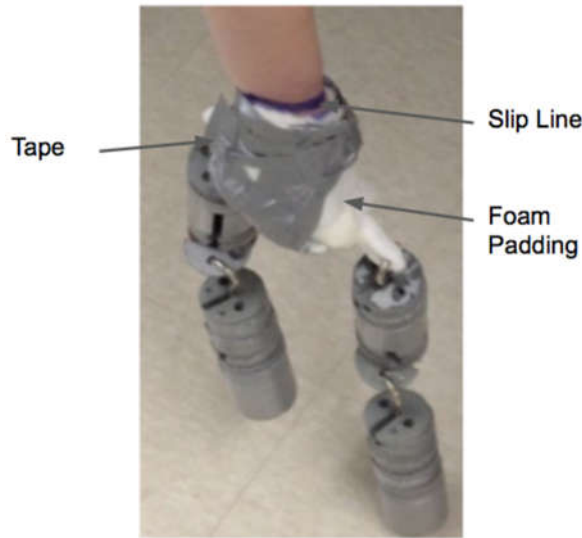


Figure 5-4 Image of the Athletic Tape Finger Brace taken during testing with the components labeled

As seen in the figure, duct tape was used in order to secure the foam padding and the patient's hand. Underneath the duct tape, athletic tape was used, and during device testing we found that this mechanism worked much more effectively. This brace is comprised of three rigid pieces: one to restrain the metacarpals, one to restrain the flanges, and one to restrain the thumb. The rigid pieces are held together currently with tape, which will be replaced with adjustable hook and loop in a future iteration. The results from testing the Athletic Tape Finger Brace are shown in Table 5.2, and this table displays experimental data at comfort levels of 2, 3, 4, and 5.

Table 5-2 Experimental data for the Athletic Tape Finger Brace

Mechanism Used	Average Force (N)	Average Slip (mm)	Level of Discomfort
Athletic Tape Finger Brace	30.40 N	1.86 mm	2
	40.21 N	4.13 mm	3
	50.01 N	4.85 mm	4
	54.92 N	4.85 mm	5

As seen in the table, at a comfort level of 3, the slip value was 4.13 mm and the subject could withstand 40.21 N of force, which is much greater than the amount of force that the hook and loop strap could withstand. A more secure method may be needed to withstand forces for intermediate healing (100-550 N).

The security, patient and cast compatibility, ease of use, cleanability, and cost effectiveness of the hook and loop finger brace and athletic tape finger brace are shown in Table 5.3.

Table 5-3 Pugh Matrix used to evaluate the hand gripping options

	Importance of Measurement (1-3)	Hook and loop Finger Brace	Athletic Tape Finger Brace
Security	3	1	3
Patient Compatibility	3	3	3
Cast Compatibility	2	3	3
Ease of use	2	2	2
Cleanability	1	2	2
Cost Effectiveness	1	3	3
Totals		27	33

As seen in Table 5.3, the athletic tape finger brace had a total score of 33 while the hook and loop finger brace had a score of 27. In terms of security, the athletic tape finger brace was rated a 3 since it endured much greater forces (up to 54.92 N) in comparison to the hook and loop finger brace. We gave the hook and loop Finger Brace a rating of 1 since the subject's hand slipped quickly during testing.

For patient compatibility/comfort, we gave both designs a 3 since they were quite comfortable to wear during testing. Both designs were rated as 3 for cast compatibility since they do not interfere with the cast applied to the distal radius.

For ease of use, the hook and loop finger brace and athletic tape finger brace were assigned a 2 since they were moderately straightforward in applying to the hand. A slight challenge for both braces, however, was molding the plastic pellets, which can take approximately 15-20 minutes to make. Ideally, a more adaptable brace will be made to accommodate varying hand sizes.

The next requirement was cleanability, and as seen in Table 5.3, both braces received a 2 in this category. A slight challenge in cleaning these gripping options would lie in removing the plastic supports. Finally, the last requirement is cost effectiveness, and for this criterion both

devices received a 3. The total cost to make each device would be \$3-5.

As mentioned earlier, the athletic tape finger brace received a score of 33, which is higher than the hook and loop finger brace. We therefore pursued this gripping option during testing, in which we tested the device. The athletic tape finger brace had a much lower slip in the hand and could withstand much higher forces in comparison to hook and loop, which failed and slipped very easily.

5.2.3 Testing Procedure for the Elbow Mechanisms

Figure 5.5 illustrates a schematic of the testing procedure used to evaluate the elbow gripping devices.



Figure 5-5 Schematic and image for testing the elbow gripping mechanisms

The step-by-step protocol for testing the elbow gripping components is written below.

1. Lay the subject face up on the table with the arm to be tested extended at a right angle to the body and to the table, and the hand in the air.
2. Position the subject so that the elbow and about 4 inches of the upper arm are supported by the table with the rest of the arm extending beyond the edge of the table.
3. Place foam padding under the upper arm and shoulder for comfort.
4. Place foam in front of and behind the upper arm to prevent it from rotating without any effort by the subject.
5. Place and secure cardboard of about 2 cm in thickness around the hand to mimic cast contribution.
6. Apply the gripping mechanism
 - a. Ensure that the subject fully relaxes the hand and arm.

7. Secure the gripping mechanism and apply a sufficient binding force until the mechanism seems securely tightened and not prone to slipping.
8. Draw a slip measurement line with a washable marker or pen. The line is to be drawn on all portions of the skin at the edges of the gripping mechanism.
9. Load the gripping mechanism by attaching hanging weights to a string attached to the loading contacts on the hand gripping mechanism.
10. Record the applied load and measure the slip with calipers; increase the load gradually and repeat.
11. Continue to load the gripping mechanism and record the slip until the mechanism fails or the subject reports a pain level of 5 or greater on the 1-10 Self-Assessed Pain Scale.

5.2.4 Testing Data for the Elbow Mechanisms

We performed eight experimental trials for evaluating the elbow gripping mechanisms. Table 5.4 displays experimental data at comfort levels of 3, 4, and 5 for the elbow brace, blood pressure cuff, and bony contacts for the elbow. More detailed data for each subject is shown in Appendix E.

Table 5-4 Experimental data for the elbow gripping mechanisms

Mechanism Used	Average Force (N)	Average Slip (mm)	Level of Discomfort
Elbow Brace	25.50 +/- 17.83	2.76 +/- 0.02	3
BP Cuff	17.00 +/- 3.11	3.66 +/- 1.92	3
Bony Contact Brace	32.26 +/- 11.89	1.99 +/- 0.23	3
Elbow Brace	30.73 +/- 17.55	3.73 +/- 0.39	4
BP Cuff	28.77 +/- 10.21	5.13 +/- 2.19	4
Bony Contact Brace	38.90 +/- 10.76	3.38 +/- 1.49	4
Elbow Brace	37.59 +/- 16.12	4.96 +/- 1.08	5
BP Cuff	35.63 +/- 9.82	9.81 +/- 1.59	5
Bony Contact Brace	43.80 +/- 10.75	4.81 +/- 1.00	5

Based on the experimental data, the bony contact brace can withstand the greatest force for the various discomfort levels. Figure 5.6 depicts images of testing the blood pressure cuff, elbow brace, and bony contact brace. As seen in this figure, the blood pressure cuff (in the middle of the figure) had a much higher slip in comparison to the elbow brace and bony contact brace. More experimental images for testing the elbow gripping mechanism are shown in Appendix G.

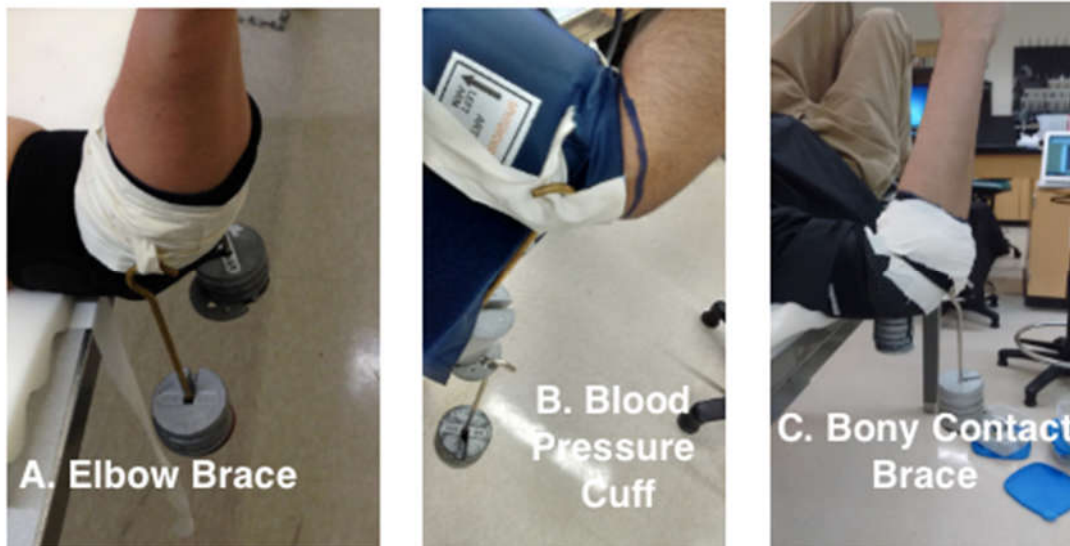


Figure 5-6 Experimental images for testing the A) Elbow Brace, B) Blood Pressure Cuff, and C) Bony Contact Brace

Like the hand gripping evaluation, we considered the security, patient and cast compatibility, ease of use, cleanability, and cost effectiveness for each elbow gripping mechanism. The Pugh Matrix that we used to evaluate the elbow gripping options is shown in Table 5.5.

Table 5-5 Pugh Matrix that was used to evaluate the elbow gripping options

	Importance of Measurement (1-3)	Elbow Brace	Blood Pressure Cuff	Bony Contacts for Elbow
Security	3	2	1	3
Patient Compatibility	3	3	3	3
Cast Compatibility	2	2	3	2
Ease of use	2	3	3	3
Cleanability	1	3	3	2
Cost Effectiveness	1	3	3	3
Totals		31	30	33

In terms of security, we decided to rate the bony contact brace as a 3 because it endured greater forces in comparison to the other components. We ranked the elbow brace as a 2 since this option failed at lower mechanical loads. The blood pressure cuff was ranked as a 1 because it produced a significant amount of slip at higher mechanical loads.

The second requirement is cast compatibility, which refers to the comfort of each elbow gripping option. We decided to rate the elbow brace, blood pressure cuff, and bony contact brace as a 3 because these designs were comfortable to wear during testing.

Additionally, for cast compatibility, we rated the blood pressure cuff as a 3 since it is applied on the upper portion of the patient's arm, and does not interfere with the cast. The elbow brace and bony contact brace were ranked as a 2 because these options are applied on the elbow and can slightly interfere with the cast.

The fourth requirement is the ease of use of each gripping component. We rated all the components as a 3, since they were relatively straightforward to use during device testing.

Furthermore, for the cleanability of each design, we ranked the elbow brace and blood pressure cuff as a 3 because these devices are easily cleanable via standard medical procedures. However, we rated the bony contact brace as a 2 since it is more difficult to clean due to the

plastic portion. Improving its integration into the brace would improve this score. Finally, the last requirement considered is the cost effectiveness of each design. For this metric, we decided to rate all the gripping options as a 3 since they are quite affordable and cost approximately \$10-15.

Based on the design matrix and experimental results, we selected the bony contact brace as the elbow gripping component because it received the highest score of 33. Advantages that this component provides include: the ability to secure the elbow and to provide comfort to patients.

5.3 Validating the Load Cell Circuit

Both load cells were connected to a computer for data acquisition in the following manner. The circuit diagram shown in Figure 5.7 shows how the components are connected.

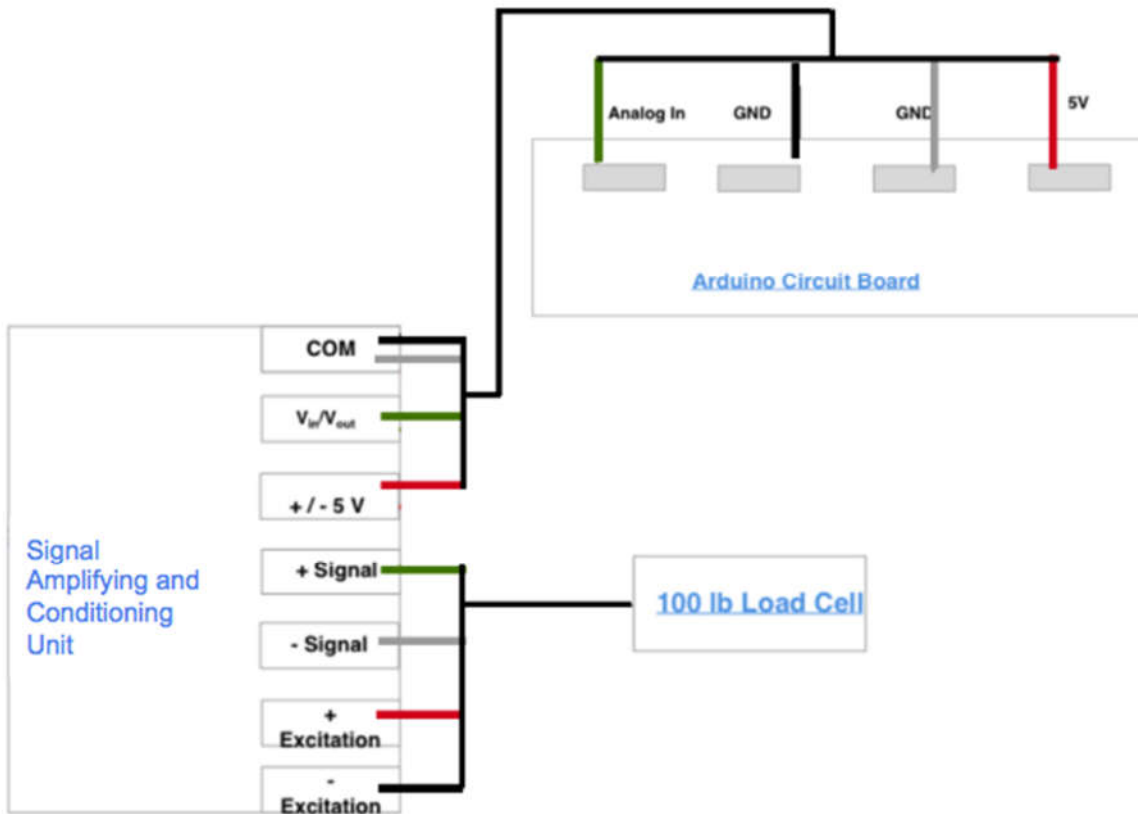


Figure 5-7 Circuit block diagram for load cell data acquisition.

As seen in Figure 5.7, the Load Cell, Arduino Circuit Board, Strain Gauge Unit, and port of each unit are labeled. In the Arduino circuit Board, the key components include the Analog input, Ground (GND), and 5V power supply ports, which are all connected to the Strain Gauge (via the +/- 5 V, $V_{in/out}$, and Communication ports). For the load cell, the connections are: the positive and negative excitation ports, and the positive and negative signal ports, which all lead

to the Load Cell. In this circuit, the load cell is wired into a Wheatstone bridge which permits the measurement of the voltage drop across the element. The signal for the strain gauge is then amplified and processed to improve the signal-to-noise ratio and passed into the Arduino Uno Board which allows acquisition of the voltage output. Calibration of the load cell with an Instron machine allows for the conversion of output signal to measured load. Noise was further reduced by attaching an additional building ground to the Arduino board.

The steps for validating the circuit are the following:

1. Sketch how each component of the circuit is connected.
2. Construct the circuit per circuit diagram. An image of the circuit is shown in Figure 5.8, with each component labeled.

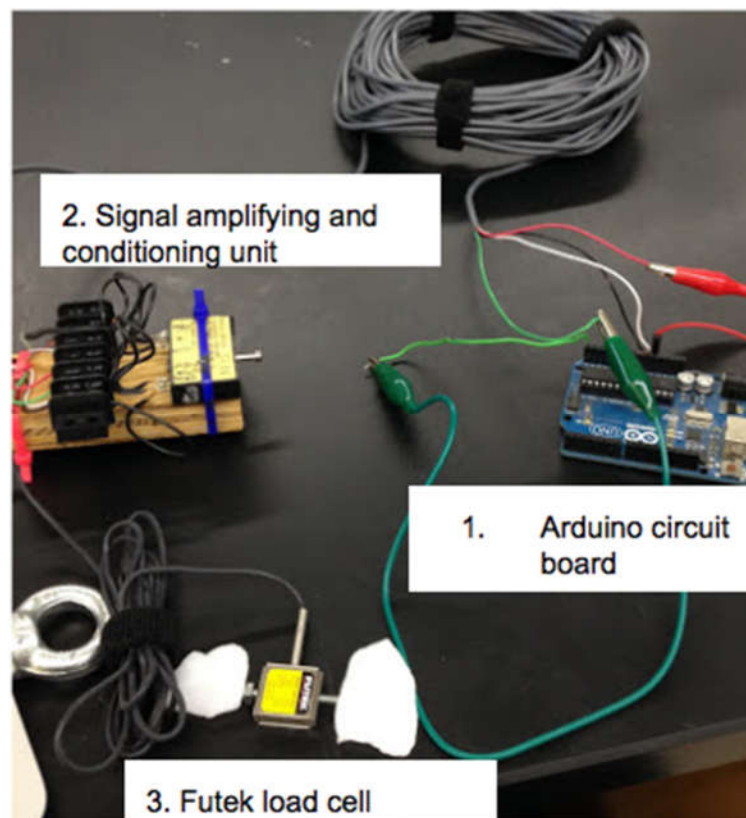


Figure 5-8 Image of the circuit with each component (including the Arduino Circuit Board, Strain Gauge Unit, and Load Cell) labeled

3. To set up the multimeter, select a multimeter function by using the dial on the instrument, and insert the measuring probes into the multimeter.
4. Ensure that the input voltage matches the expected value, which is 5V.
5. Use the multimeter probes to measure the voltage difference between various pins, and compare the measured voltages with the expected voltages.

5.4 Load Cell Calibration

Two different load cells were used for testing: a Futek beam load cell and a Phidgets compression button load cell. Both load cells were connected to a signal conditioning and amplifying unit and to an Arduino to read the output voltage drop.

The offset voltage is a parameter that varies between load cells, and therefore needs to be measured prior to calibration. The offset value corresponds to the y-intercept of the calibration curve later discussed. The gain is the ability of the circuit to increase the amplitude of the signal, corresponding to the slope of the calibration graph. In these equations, F is the known force placed on the load cell and G is the gain value. Offset and gain are related by the equations below:

$$F = G * (\text{measured voltage} - \text{offset voltage}) \quad (1)$$

$$G = F / (\text{measured voltage} - \text{offset voltage}) \quad (2)$$

The Arduino software was set to output data at the sampling frequency of the Instron. The Arduino linearly maps voltages in the range of 0 - 5 V to 8 digital bits. Therefore, it is necessary to calibrate the circuit to correspond output bits to force on the load cell. For calibration, the load cell was placed in an Instron 5544 materials testing machine, and loaded in the range of 0 to roughly 85 lbs. (378.1 N) which corresponded to an output of 5V, the maximum voltage input for the Arduino Uno. The Arduino output is plotted against Instron force during each calibration run, then linearly curve-fit. This test indicated a good level of repeatability between runs as well as linearity of the device.

Steps for experimental testing of the Futek Load Cell:

- 1) Calibrate the load cell.
 - a. Connect the load cell to the circuit.
 - b. **To determine the offset voltage:** use a multimeter to measure the output voltage when no force is applied to the load cell.
 - c. Place a weight (of known mass) onto the load cell, and record the output voltage produced by the weight.
 - d. Quantify the required gain for the load cell by using Equation (2).
 - e. Apply the gain needed for the load cell to take measurements in the required force range.
- 2) Place the load cell on the Instron Testing Machine, as shown in Figure 5.9.

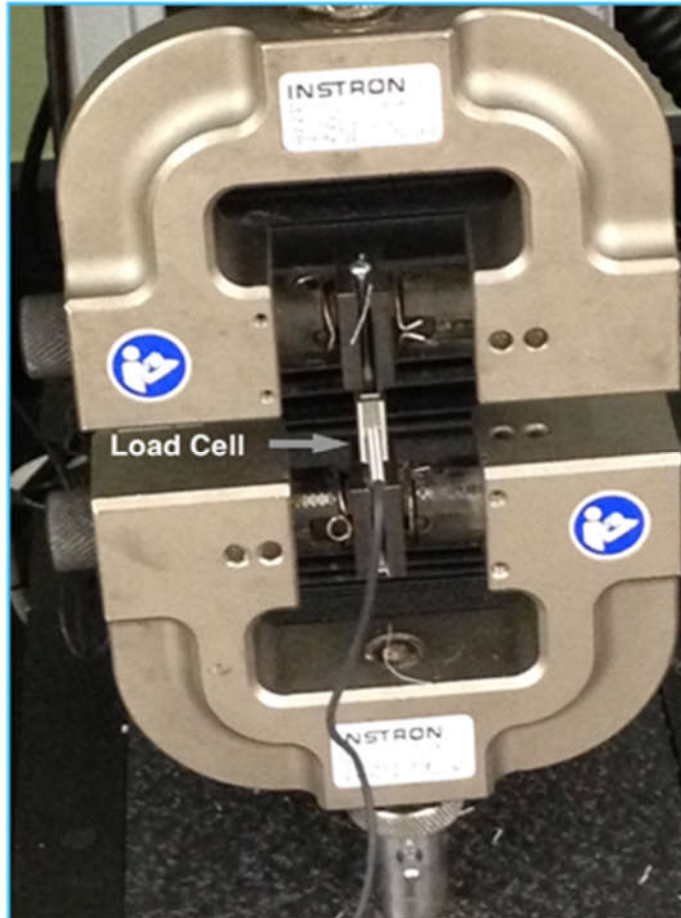


Figure 5-9 Image that depicts how the load cell is placed on the Instron Testing Machine

- 3) Record the force reading on the load cell.
- 4) Compare the experimental and calculated force values.
- 5) Repeat the test 2 more times to ensure experimental accuracy.

Figure 5.10 depicts the results of one trial of the Load Cell Linearity Test.

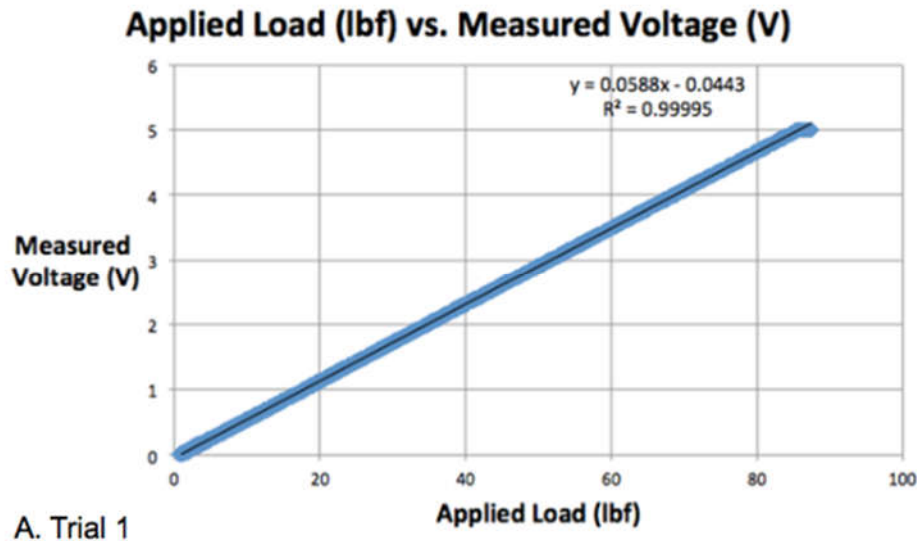


Figure 5-10 Graph that depicts the line of best fit and the coefficient of determination for the Average Voltage (in volts) and the Applied Load (in pounds) for Trial 1.

As seen in the figure, the load cell could properly correlate the voltage output to the applied force since the curve has a linear fit. The Coefficient of Determination (R^2) is 0.9999, which indicates that the linear model provides a very good representation of the data. The results of all the trials are shown in Appendix H. Furthermore, the slope of the line of best fit (change in Voltage/change in Applied Load) was quite similar for each trial: the slope was 0.0588 v/lbf in the first trial, and 0.0587 v/lbf in the second trial.

The potential difference between various pins. The reference and ground pins have a voltage of 0, which was the expected value. Similarly, the 5V power supply and the ground pin had a voltage difference of 4.79 V, which was close to the expected value of 5 V. Finally, when a 50 lb force was applied to the load cell, the potential difference between the signal to ground was 2.82 V, which was close to the expected value of 2.91 V.

The compressive button load cell is a Phidgets model 3137 with a capacity of 200 kg (approximately 1960 N). The button load cell was calibrated in compression using the Instron, similarly to the Futek load cell. The button load cell was loaded using the 3-point bend fixture and a compressive force was applied at a rate of 0.1 mm/min to a maximum force of 1900 N. The graph below in Figure 5.11 shows the calibration of the load cell from mV to N.

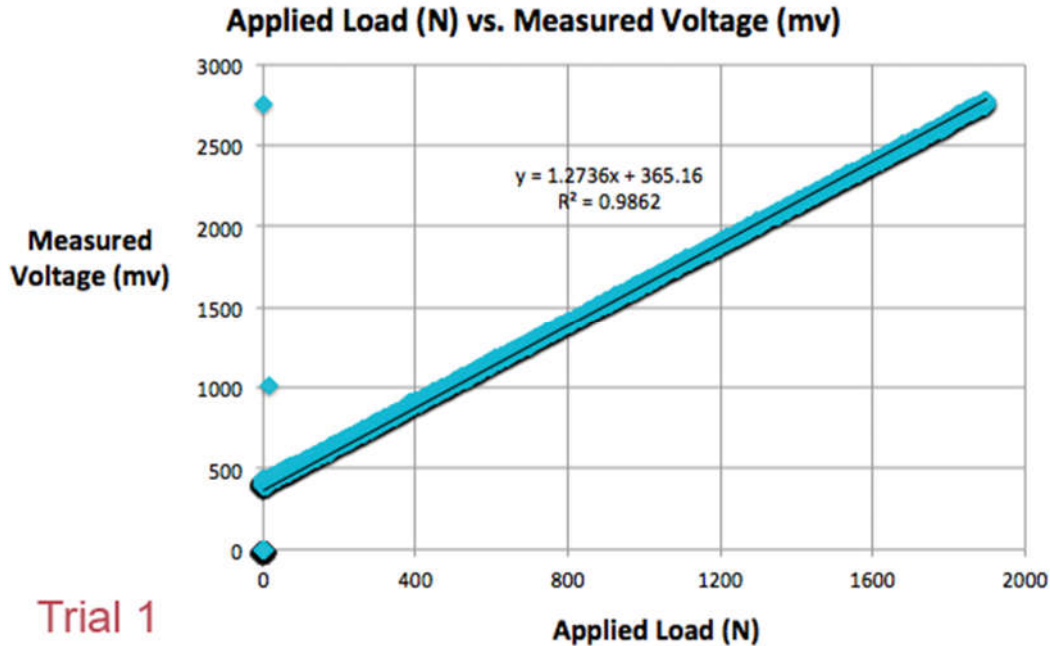


Figure 5-11 Calibration of the Phidgets model 3137 button load cell for Trial 1

From this test, we could calibrate the load cells and validate linearity and repeatability. The Arduino code for the load cells is shown in Appendix I.

5.4.1 Loading Mechanism Testing

Testing was run on a model of the functional loading section of the device to determine how much force the rods could apply for degrees the rod was turned. First the Futek load cell was used driving the mechanism open to load the cell in tension. This gave the first indications that the drive mechanism was not sufficiently high in resolution. Data for this test are not shown, as the mechanism is not intended to load in tension. The button load cell was used to test the amount of force applied by the drive rods prototype device. The test was used to correlate the amount of force applied to the degrees the screws are turned and the linear distance downward that the pressure point traveled.

Test Protocol:

1. Assemble the force application piece and connect to the computer and Arduino board, as shown in Figure 5.12. An aluminum bridge is placed across the open portion of the bottom plate. The drive rods are screwed into the top plate. The load cell is sandwiched between the bridge and top plate with the button against the top plate. The bottom plate is slid over the drive rods and secured using the nuts.

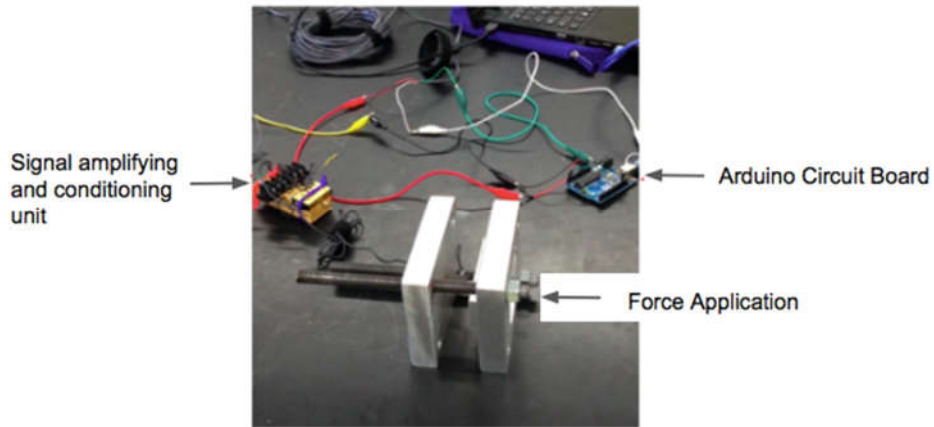


Figure 5-12 Image of the force application piece with the signal amplifying and conditioning unit and Arduino board

2. Place the device (with the button load cell) on the table, as shown in Figure 5.13.

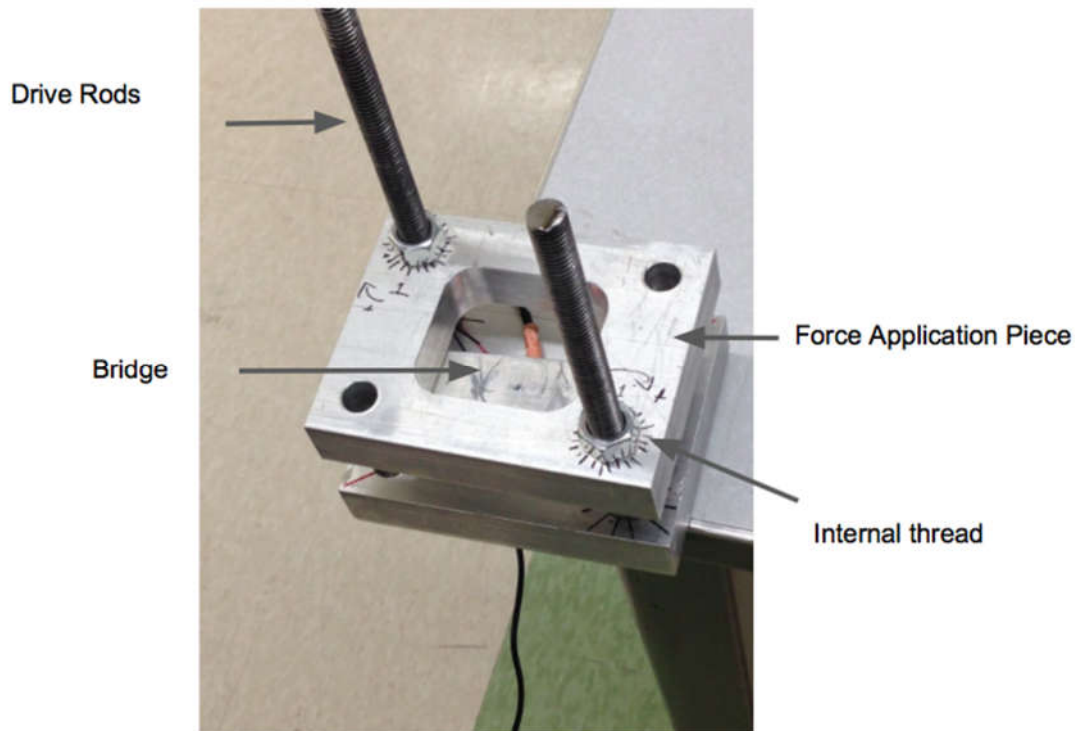


Figure 5-13 Image of the force application piece on the table

3. Draw 24 reference lines on the base and number these 1-24, as seen in Figure 5.13. Each line correlates to 15 degrees.

4. Tape the bridge to the base, and tighten the internal threads onto the drive rods.

5. Turn 1/24 of a rotation (to the first hatch mark) on both rods and determine the applied load using the Arduino Uno Software. Allow 30 seconds of reading the force to allow for enough data points outputted from the Arduino.

6. Repeat until the maximum force measurable by the load cell is reached.

7. Save Arduino output data.

Five runs of the test were completed and the results were analyzed in MATLAB. Figure 5.14 below shows the graph of linear distance to average force.

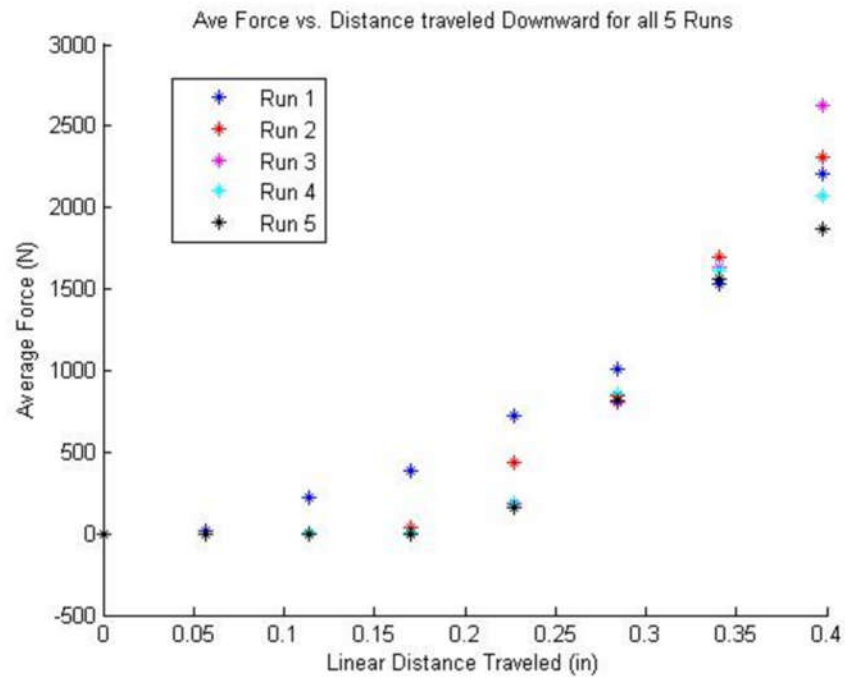


Figure 5-14 Graph of the Average Force Generated vs. the Linear Distance traveled downward for the force application piece

Figure 5.15 correlates the degrees of force turned to the average force.

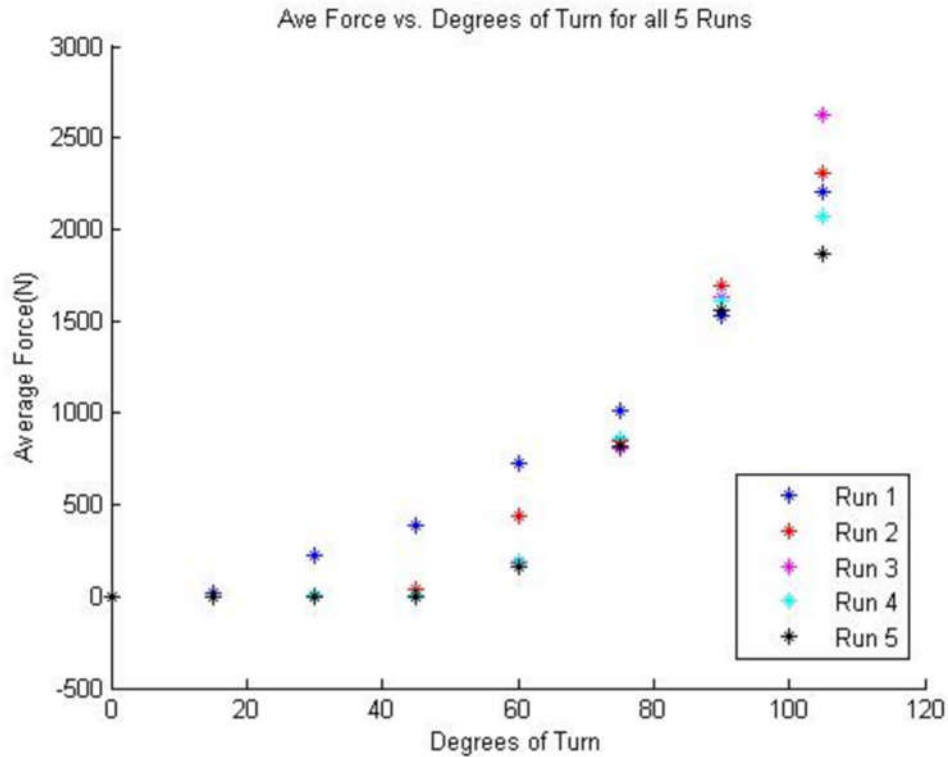


Figure 5-15 Graph of the Average Force Generated vs. the number of degrees each rod is turned for the force application piece

Both Figure 5.14 and 5.15 depict all five runs and all data from the eight turns of the screw. These graphs are not linear. Runs 1 and 2 varied from runs 3 to 5. Variation in testing was due to the instability of the test set-up due to the button on the button load cell, and due to the precision available (by adjusting only a small amount by hand). The variability of the first two runs may have been because the load cell required time to warm up. The first four screw settings (except for run 1) were effectively zero, showing that the load cell had probably not been fully contacted in the beginning by the pressure point piece. Analyzing only runs 3 through 5, and only screw settings 5, 6 and 8 resulted in a linear fit shown in Figure 5.16 below. Screw setting 8 was removed since it was not consistent over all four runs because it was exceeding the limit of the load cell. Not enough data acquisition points could be obtained at this setting, and for some runs only one screw was turned to avoid damaging the load cell. Additional limitations were introduced by the coarse threads of the drive rods and the challenge of maintaining levelness of the plates.

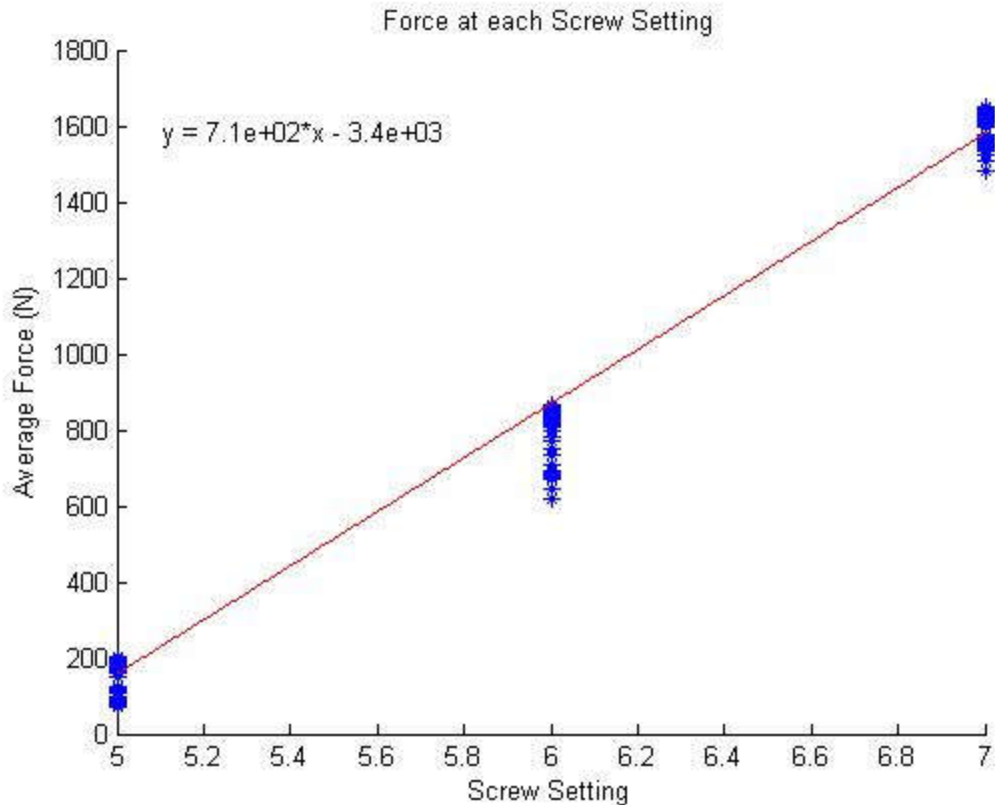


Figure 5-16 Line of best fit for applied force vs. screw setting in the button load cell

Figure 5.16 above shows the linear fit equation for the testing. This equation is also representative of the linear distance traveled and the degrees turned in the screw. This testing showed that a more finely threaded rod is necessary to achieve the adjustment needed between the loads. This testing was done only with metal parts. However, when compressing an arm, the force applied will be less at each setting because of the viscoelastic nature of the tissue.

5.5 Field of View (FOV) and Scanning Size Validation

The XtremeCT scanner has size limitations on measurement specimens as measurement resolution. Figure 5.17 shows specifications for the resolution and max scan size from the User Manual.

Specifications	XtremeCT
Type	High-resolution peripheral quantitative CT No external shielding required
Resolution	< 105 μm (10% MTF) 41 - 246 μm nominal isotropic (pixel size)
Max. scan size	126 x 150 mm (\O xL)

Figure 5-17 Image that displays specifications of the scanner including imaging resolution and max scan size

The XtremeCT has a measurement resolution of 82 microns (μm), a scan size up to 126 mm (4.96 in) in diameter and 150 mm (5.91) in length. To locate the field (FOV) of view and scan tray fixture the following procedure was used:

1. Obtain an image from Karen Troy's Lab. For the field of view (FOV) validation, we obtained an image for the fibula and tibia (shinbone) structures of the bone.
2. Upload the image into ImageJ, which is an image processing software.
3. Set the scale for the image, as seen in Figure 5.18 by clicking the Analyze Tab, and then the measure option.

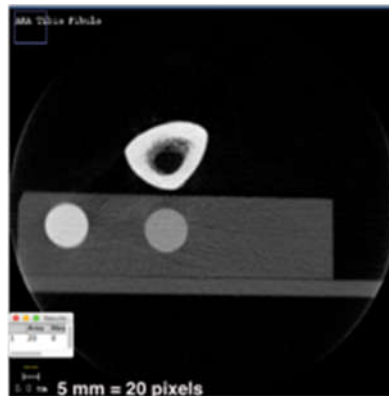


Figure 5-18 Image that depicts the scale bar the team set

In this figure, 5 mm is equivalent to 20 pixels.

4. Measure the diameter and the height of the image, and then compare these values to the maximum scan size.

The diameter was 509.08 pixels, as seen in Figure 5.19.

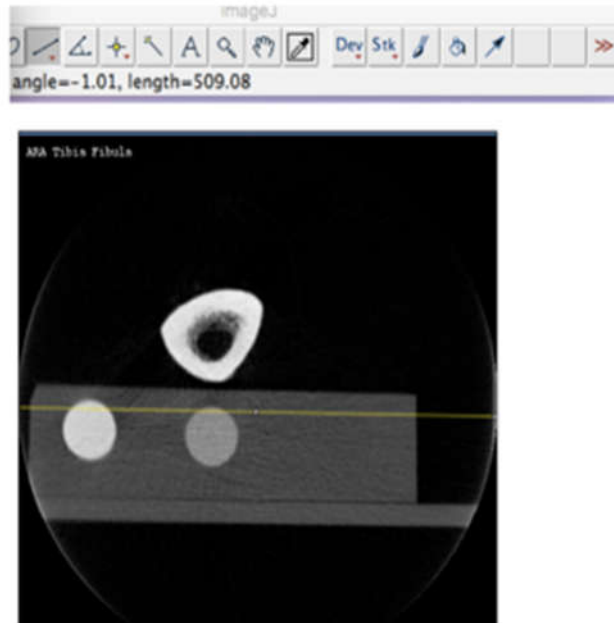


Figure 5-19 Image that displays the diameter that we measured

Pixels are converted to millimeters using the conversion rate of 5 mm = 20 pixels, resulting in a diameter of: $509.08 \text{ Pixels} * (5 \text{ mm} / 20 \text{ pixels}) = 127.3 \text{ mm}$ (5.01 in). The height of the field of view is 374 pixels, as seen in Figure 5.20.

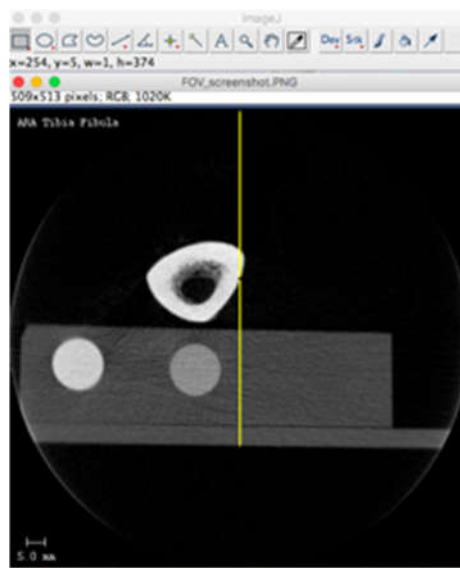


Figure 5-20 Image that displays the height that was measured

When converted to millimeters, the height was: $374 \text{ Pixels} * (5 \text{ mm} / 20 \text{ pixels}) = 93.5 \text{ mm}$ (3.68 in).

Through measurements in ImageJ, the diameter of 127.3 mm (5.01 in) was quite close to the maximum scanning diameter (126 mm or 4.96 in). The measured height of 93.5 mm (3.68 in) is within the maximum height of 150 mm (5.91 in). The resolution used for this scan was 82

microns. The tray fixture is known to be in the center of the lower plate in the image, which corresponds roughly to the center of the FOV. This information guided the placement of the scanner clip fixture on the device under development, as well as the definition of arm placement to ensure proper imaging.

After device fabrication, cadaver testing is planned to validate device ability to displace a 'fractured' bone, and that this displacement is measurable in the image. A resolution of 82 microns should be sufficient to measure displacement of fragments, based on engineering calculations presented in Chapter 3.

5.6 Device Ergonomics Testing

We planned to perform human subject testing to verify ergonomic and imaging performance. However, due to time constraints, we were unable to perform this testing procedure. This testing procedure can be pursued in a future project. The full testing protocols are shown in Appendix J and the IRB application to receive approval of the study is shown in Appendix K. The experimental test asks the subject to report how comfortable the device is when a mechanical load is not applied, using a rating on the self-assessed pain scale from 1-10.

During testing, the arm would be placed palm down, and the distal radius would be imaged unloaded. Then (using the device) a static load can be applied and the distal radius reimaged. Displacement would be assessed in the digital image, allowing the calculation of stiffness in the healing bone. It is important to note that the stiffness is an indicator of how much a distal radius fracture has healed.

In the testing procedure, force to the subject's wrist would increase in 50 N increments (approximately 11 lbs.) up to 550 N (approximately 123 lb), until a pain level of 5, or the subject asks to stop. During each force increment, the subject would be asked to report how comfortable the device is. The force would be held for no more than one minute, and the testing would stop when one of the following criteria is reached: a) the maximum necessary force of 550 N is reached, b) the subject reports a discomfort level of 5 or below, or c) the subject requests the experiment to be stopped. A sample flyer that can be used to recruit subjects is shown in Appendix L.

5.7 Avian Bone Imaging Validation Testing

The procedure for avian testing is shown in the Appendix M. Team members completed Biosafety and bloodborne pathogens training to ensure proper safety in the lab.

The goals were to:

1. Validate and measure bone displacement for both a whole and fractured distal radius
2. Evaluate the ability of the device to produce a displacement in a safe and relevant range for a healing bone
3. Determine the device's compatibility with skin and soft tissue
4. Understand the degree of force mediation due to soft tissue over the imaging site
5. Determine CT image clarity by evaluating the following:
 1. The ability to detect displacement in CT images
 2. Ability to measure displacement in CT images

To measure fragment displacement, the team inserted the device into the CT scanner and took an unloaded HR image of the cadaver specimen. Then, a force of 50 N (~11 lbs.) was applied to the specimen, and was increased up to 275 N (~61.5 lbs.) and 550 N (~ 123 lbs.). Images were taken at each force increment and determine the displacement of the loaded cadaver arm using the Micro CT software and Mimics Software version 18.0 (made by Materialise) following standard segmentation of HU from -270-600 for bone followed by manual correction. Displacements were measured in Mimics using the Measurement tool on the border of the bone and flesh regions.

It was not possible to measure deflection as in the first set of tests, the bone was not placed under the pressure point but rather next to it, resulting in no bending force being applied. In the second set of testing, the bone broke at the cut due to excessive transient loading. In this testing set, it was further tried to displace the metaphysis of the specimen, however the bone rotated about the long axis, as assessed by position of tendon insertions in the images, leading to an inability to compare like-to-like bone positioning in loading states. Additionally, whole avian bones possess a very high modulus compared to healing human fracture regions, thus any displacement seen would be expected to be significantly lower than that anticipated in the clinical setting. Future work would use radiopaque biological equivalent phantoms to examine displacement, or might use partially healed sheep or porcine bone for the imaging validation.

Initially, it was posited that displacement of the edges of the fragments would be measures, however bone edges resorb and become fuzzy in the remodeling process. Therefore, it was determined that measuring the distance between a line drawn from the edges of the bone at the limit of the image and from that line to the edge of the bone directly under the pressure point is the most robust method.

Image Clarity Evaluation

Imaging clarity is of concern due to device element thicknesses required to withstand high loads. To determine the clarity of CT images, the team took a high-resolution image of a cadaver arm on the standard cadaver specimen tray, without the device, to obtain a baseline image. Then, we took a high-resolution image of a cadaver arm in the device. Finally, a visual assessment was made and recorded by a member of the lab trained in radiology, and QCT data will be compared for the arm with and without the device.

5.8 Third Quarter Design Changes

Bending portion for testing production

A prototype version of the loading mechanism was manufactured out of aluminum stock, Delrin guide rods, and steel $\frac{1}{2}$ - 13 threaded rods for evaluating mechanism motion. This model also enabled mechanism force transmission validation and comfort testing. Solidworks CAD files were prepared for the loading region by slicing the whole model as shown in Figure 5.21. The files were prepared for CNC machining using the CAM software ESPRIT and machined in the WPI Washburn Shops and Manufacturing Labs. The empty holes hold the guide rods, which improve smooth operation of the mechanism.

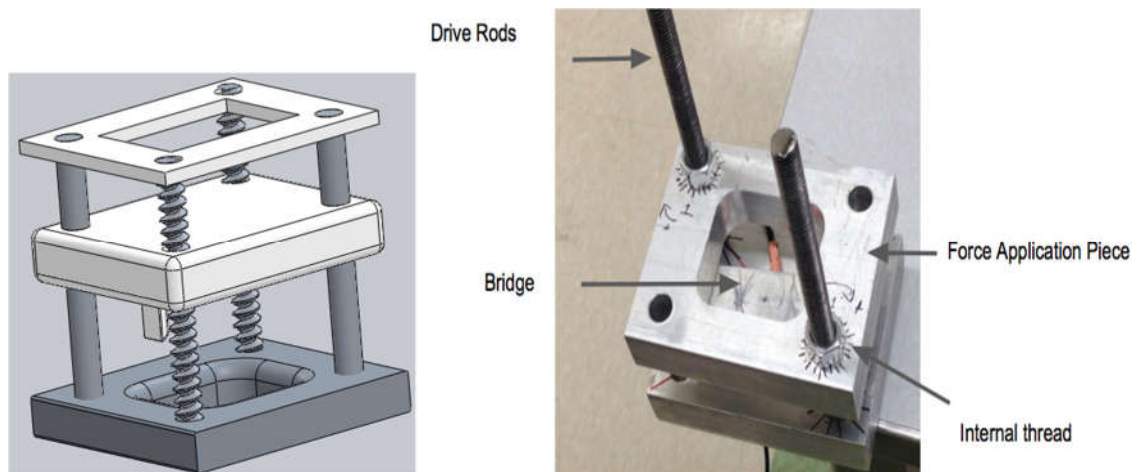


Figure 5-21 Loading region model sliced for prototyping (left) and prototype with load cell (right).

Force testing with the loading portion of the device indicated that once secure, compression was achieved, and there was very little deflection achievable without great force. It is expected that the secure compression range with a human arm is much greater in comparison to the force testing completed; this is due to the compliance and thickness of soft tissues in human

wrists. To address this drive mechanism resolution problem, the threads of the rod used were changed to 20 threads per inch. The design changes made to improve the spatial and loading resolution of the device are presented in Chapter 4 Section 4.6.1 Drive Mechanism Resolution Improvement.

5.9 Pressure Testing

To identify the predicted range of pressure between the pressure point and the patient's wrist during loading, the pressure point's area of contact is assumed to be ½ of an inch squared. This value is derived from measuring the residual pink region on the team member's wrists after loading comfort self-experimentation. The max force predicted to displace an intermediately healed bone is 550N (approximately 123 lb). Therefore, the pressure that will be applied to the patient is: $123 \text{ lb}/0.5 \text{ in}^2 = 247.4 \text{ psi}$. Table 5.6 displays calculated pressures for pressure concentration factors up to 4 due to the rounded pressure point tip.

Table 5-6 Calculated pressures for pressure concentration factors up to 4

Concentration factor	Pressure (psi)	Pressure Reference
1	247.4	Pressure of human bite
2	498.8	Paintball propellant
3	742.2	Spray nozzle, car wash
4	989.6	Low-end pressure washer

We do not anticipate that a pressure above 498.8 psi (about twice the pressure of a spray nozzle at a car wash) will be well tolerated by the patient.

While the applied force is known, the pressure applied to the wrist is less definite and can vary between individuals. Since tolerability of forces was likely dependent upon the pressure applied, a test using the aluminum prototype and pressure sensitive film was conducted. Pressure sensitive film pieces were first calibrated using known force on the Instron on a known area of the paper. Three pieces of film were placed on the device, at the proximal and distal edges of the cut-out, and on the pressure point. The arm was placed in the device and force was applied via stacking weights on top of the top plate of the prototype. The complete testing protocol can be found in Appendix O.

Results were largely inconclusive in terms of pressure applied. The scans containing all pieces of stained film can be found in Appendix P. It was found that the greatest pressure was

applied via the pressure point. Also, the edges of the cutout had less of a fillet in the final design and were not padded for the test, likely causing increased pressure applied on the distal and proximal edges of the base to the arm.

5.10 Pressure Point Comfort Testing

For the right arm of each member of the team, the arm was placed into the aluminum prototype device. The pressure point was lined up against the styloid process of the wrist. A pain rating was taken on the scale from one to ten at increasing force levels. The force levels used were 0, 7.76, 15.52, 23.29, 31.05, 38.81, 46.57, 54.34 Newtons. These force levels were chosen to remain consistent with the levels of the pressure sensitive film testing, as explained in Section 5.9. Force was applied by the placement of known weights to the top plate of the prototype. This process was repeated using the left arm of each subject and with the chamfered pressure point, full round pressure point and chamfered covered in thin foam padding.

The graph in Figure 5.22 below depicts the comparison of average pain rating at increasing force levels for each pressure point option. Testing was performed for each member of the group.

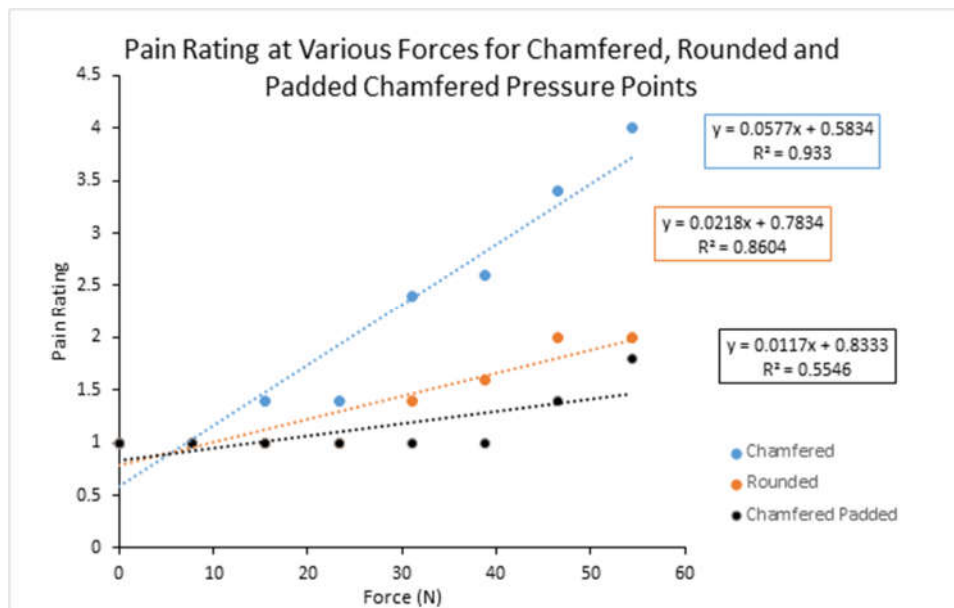


Figure 5-22 Graph of Comfort Testing results comparing various pressure point designs

As seen in the graph, the maximum pain level reached was highest for the chamfered pressure point. Padding this pressure point decreased the force levels to be lower than those for

the rounded pressure point. The chamfered pressure point with padding was chosen because of this testing to ensure localization of the force and increased comfort via padding.

This testing also verified that the device in general, and the loads applied were tolerable up to 54 Newtons. Beyond this could not be evaluated due to a lack of known weights to add to the prototype to increase applied force. Complete data and graphs from this testing can be found in Appendix Q.

5.11 Instrumentation

Strain gauges permit the measurement of micro strain in loaded members, and are a standard loading measurement instrumentation. In this application, the non-driving portions of the drive rods are turned down to a standard dogbone test piece, and a strain gauge is applied to this portion. The strain gauge is wired to a conditioning and amplifying circuit, which reports resistance change across the gauge at a given load. Calibration allows the direct measurement of force in the member. Testing remains to be completed to know if force can accurately be assessed by doubling the force in the proximal drive rod or if it is necessary to measure the force in the distal drive rod as well. If the latter is true, wireless or radiolucent wiring techniques will be needed to prevent imaging artifact.

Placing strain gauges on the drive rods also impacts the drive mechanism configuration. The current configuration turns the rods to translate the top plate. In this case the pulleys under the device had a rigid connection to the drive rods and turn with the drive rods. If a strain gauge is placed on the drive rod, it is preferable not to turn the rods to avoid wrapping the instrumentation wires. This is accomplished by fixing the drive rods with respect to the top plate and placing threaded nuts inside the pulleys. Turning the pulleys then drives the rods with respect to the base without turning the drive rods.

Placing strain gauges on the drive rods also impacts the drive mechanism configuration. The current configuration turns the rods to translate the top plate. In this case the pulleys under the device have a rigid connection to the drive rods and turn with the drive rods. If a strain gauge is placed on the drive rod, it is preferable not to turn the rods to avoid wrapping the instrumentation wires. This is accomplished by fixing the drive rods with respect to the top plate and placing threaded nuts inside the pulleys. Turning the pulleys then drives the rods with respect to the base without turning the drive rods.

Chapter 6 : Design Verification – Discussion

While designing, fabricating, and planning experimental tests for this device, there were a wide range of non-technical considerations to address. These include economic, environmental, societal, political, health, and manufacturability considerations.

Economics

In the U.S. alone, there were 640,000 cases of distal radius fractures that were reported in 2001. Furthermore, distal radius fractures account for 18% of all fractures in the elderly age group. In terms of healthcare costs, in 2007, Medicare paid \$170 million in distal radius fracture treatments. The mean payment for each patient was approximately \$1,983. This device aims to improve outcomes for one of the most common injuries in adults in the United States [57]. Significant economic costs are incurred by the person experiencing a distal radius fracture in doctor's appointments, casting, imaging, and lost productivity. These costs are passed on to society through burdens on the health insurance and care systems, and lost worker time. Distal radius fractures primarily impact postmenopausal women who are at an increased risk of fragility fracture due to age-associated osteoporosis, a condition that affects women worldwide. Due to their unpredictable healing rate, many of these patients will experience delayed union or non-union, which will not be detected until they are uncasted at the typical 6-8 weeks. These patients may continue to experience pain or re-injure themselves leading to retreatment and often the need for surgical intervention. Additionally, the cost to treat distal fracture complications was not found in the literature, but complications occur in over 80% of the fractures [58]. However, this device can help reduce the need for retreatment, which can in turn lead to lower medical costs. We anticipate that this device will improve diagnosis and monitoring for these at-risk patients and reduce overall treatment durations. It will reduce the burden of healthcare costs in the U.S. and globally by reducing the amount of care and time needed in this fracture population.

We anticipate that the device will help decrease the cost to treat distal radius fractures by allowing physicians to more accurately assess the degree of healing. This will allow for more accurate treatment decisions and can prevent premature cast removal, which can in turn decrease the net medical expenses for treating distal radius fractures.

It is important that the device be affordable for both hospitals and imaging centers. To achieve this goal, we selected materials that offered the optimal combination of strength, toughness and stiffness for a price of less than \$15/kg per CES EDUPACK.

The current device prototype costs around \$420 in materials, and several hours in setup and assembly. Improved manufacturing techniques and the recommended final materials will further reduce the production cost of the device. Even with the preliminary model, the device and project cost about half the required \$1000, not including time spent by the team and support staff. The complete bill of material can be found in Appendix R.

Environmental impact

This device has a small to negligible impact on the environment. Sources of environmental stresses in this project include material usage and bio-hazardous waste.

Materials that will be used to make the device include: stainless steel, brass, foam, and glass-fiber reinforced Onyx. The plastic material, Onyx, is recyclable by shredding and washing the material, and then turning the material into a granulate (which will be ready to be used again). Additionally, polymer composites (such as Onyx) have been shown to be recyclable through other techniques. One method that can be implemented involves using supercritical fluids to separate the polymer matrix and carbon fibers. This process degrades the resin into lower molecular weight compounds. The tensile properties of the fibers have been shown to retain their original tensile strength after recycling. In addition, the fibers can remain undamaged and retain their original morphology [59].

Biological waste was limited to avian specimens which were obtained at meat market, and PPE. All materials were disposed through standard institutional protocols, and represented less than 5 lbs. of waste.

Societal Impact

During the design and manufacturing process, we considered the net societal impact our device will have. To produce a positive societal impact, we aimed to make our device easy for physicians and technicians to use. We did this by selecting the bending design, which is easier to use in comparison to the tension design. The device can not only benefit physicians and technicians, but it can also benefit patients with distal radius fractures. By observing bone displacement and by measuring the strength of healing distal radius fractures, the device can help

prevent premature cast removal and allow for early identification of healing complications. This will improve patient experiences, outcomes, and the standard of medical care for the single most common bone injury in adults. Early identification will permit lower overall complication rates and associated treatment costs. The device also provides a platform for quantitatively evaluating bone healing interventions, which is currently unavailable.

Political Ramifications

We considered how the device will influence the global market and political ramifications. It is expected that the device will have no direct political impact. This is an orthopedic diagnostic device and addresses a significant need in the healthcare industry. For our device to have a positive impact on the global market, it is essential that it first performs well in the U.S.

We anticipate that once the device does well in the U.S., then it will have a positive influence on the global market. Per the National Institute on Aging, 8.5% of people today are aged 65 and over. This percentage is projected to increase to 17% of the world's population by the year 2050. An increase in patients who are ages 65 and older can lead to a greater number of fractures in the world's population. Thus, the device, which can measure the extent of healing in distal radius fractures, can add value to the global healthcare marketplace. It will continue to be important to make healthcare affordable and accessible to an aging population in the future.

Ethical concern

One major ethical concern includes testing the device with human subjects. All testing must be IRB approved and follow standard protocols to manage risk and ensure participants provide appropriate informed consent. It is also crucial to maintain appropriate confidentiality measures, document all testing completely, and provide unbiased information on testing outcomes in publications.

Another ethical concern is using cadaver models during testing. When using cadaver models, it is important to understand that these people have donated their body for scientific research and the advancement of healthcare. Therefore, it is essential to conduct cadaver testing respectfully. For the purposes of preliminary testing, avian bone and tissue specimens were used as they possess material properties like those of humans and have lower safety and ethical risks.

Health and safety issues

The first health and safety concern is for damage resulting from the diagnostic technique. The scanner can measure displacements starting at 164 microns, so the device must displace the bone at least this far to perform the diagnostic measurement. At first consideration, it may seem unwise to displace a healing bone. However, bone needs to sense small amounts of motion both to detect damage and to heal well. This is normally accomplished with an external cast that allows small amounts of motion between the bone fragments but prevents gross misalignment. Various therapeutic techniques such as traction and distraction osteogenesis are used to promote bone healing at quasi-static displacement rates of up to 1 mm per day. All materials deform (experience strain) to a degree when subjected to loading, with softer materials deforming more than harder materials of the same geometry under a given load. Transient strains produced by rapid loading can be significantly higher than strains produced by slow loading with the same force. Such transient high strains are produced by daily activities such as opening doors and shaking hands, and are commonly experienced by individuals with healing fractures. Thus, with proper application, this device does not expose the patient to significantly more mechanical risk than daily living activities.

The device designed has a spatial resolution of less than 1 mm in the drive mechanism, and less than half a millimeter per complete turn in the recommended 40 TPI drive mechanism described in Ch 7. The device is also able to provide real-time loading information. Combined, these two features allow the technician to know precisely the mechanical demands being applied to the tissue. Further work with cadaveric and biological equivalent models will help to validate the loading-displacement relationship of the device and to train the automatic image processing software that needs to be developed.

The device use protocols call for initial unloaded imaging of the bone followed by imaging at increasing loading levels to produce measurable displacements in the healing region of the bone. Combined with the excellent spatial resolution and knowledge of the time the fracture has been healing, a conservative max force level can be determined for individual patients to prevent damage while still enabling the diagnostic function. The next step in validating the device requires cadaveric testing of radii in different, known degrees of healing, to better understand the deformations, deflections, and develop ideal imaging techniques. While working with cadavers, it is important to follow safety precautions for Biosafety Level 2. Care must also be taken to responsibly use these resources with respect for their donors.

Currently there is no way to quantitatively measure bone healing noninvasively. Physicians commonly assess healing through a combination of palpation and patient pain ratings, leading to uncertainty in the assessment of healing extent. This results in longer casting times, premature uncastings, and risk for further injury and treatment. Measuring healing extent takes the ambiguity and variability out of fracture healing evaluation providing an unprecedented quality of care.

This diagnostic technique requires radiation exposure to produce the images. There is a biological risk associated with radiation exposure, however pCT (Peripheral Computed Tomography) imaging produces significantly lower radiation exposure in comparison to normal CT imaging. In terms of the health impact that our design will make, we anticipate that use of the device will result in improved recovery for patients with distal radius fractures. For instance, the device can allow for earlier identification of healing complications and can prevent premature cast removal. Premature cast removal often leads to re-injury requiring further radiographic evaluation, casting times, and surgery, all of which are negative outcomes and lead to further treatment-associated risk for patients. Improving treatment monitoring with this device may also reduce the overall radiation and extended care required to correct healing complications.

FDA approval, regulation, and documentation

For use in the US, the device needs to comply with FDA standards. This device is a Class II Risk medical device because it has moderate risk associated with it. Safety and effectiveness should be demonstrated prior to market release. As an orthopedic device, it is regulated by the FDA CFR Title 21 Subchapter H Medical Devices Part 888 Orthopedic Devices Subpart B Diagnostic Devices. After clinical trials and before clinical use, the device needs to file a 510(K). This device is not “Substantially Equivalent” to any other devices currently or previously available and thus is a “New” device. Premarket testing and validation should be guided by the appropriate FDA guidance document: Center for Devices and Radiological Health Standard Operating Procedure (SOP) Level 1, immediately in Effect Guidance Documents on Premarket Data Issues.

Manufacturability

Ease of manufacturability via standard processes. To make our device reproducible, we selected 3D printing as the manufacturing technique for the prototype because it is easily accessible. Benefits that 3D printing offers in comparison to injection molding include: quicker manufacturing time and lower production costs. We also considered injection molding but decided

not to pursue this manufacturing option due to time constraints. The final version of the device is recommended to be manufactured using injection molding with carbon fiber reinforcement. This offers a good balance of low cost, ease of processing, high strength, rigidity, and toughness.

CAD drawings were created of the design throughout the development process. Complete component and assembly drawings were created and are provided in Appendix T. The device can be readily reproduced by using SolidWorks and prepared for machining using standard CAM programs such as Esprit to manufacture needed fixtures and/or the device. Accessory components such as threaded rod, washers, nuts, and bolts are readily available and low-cost.

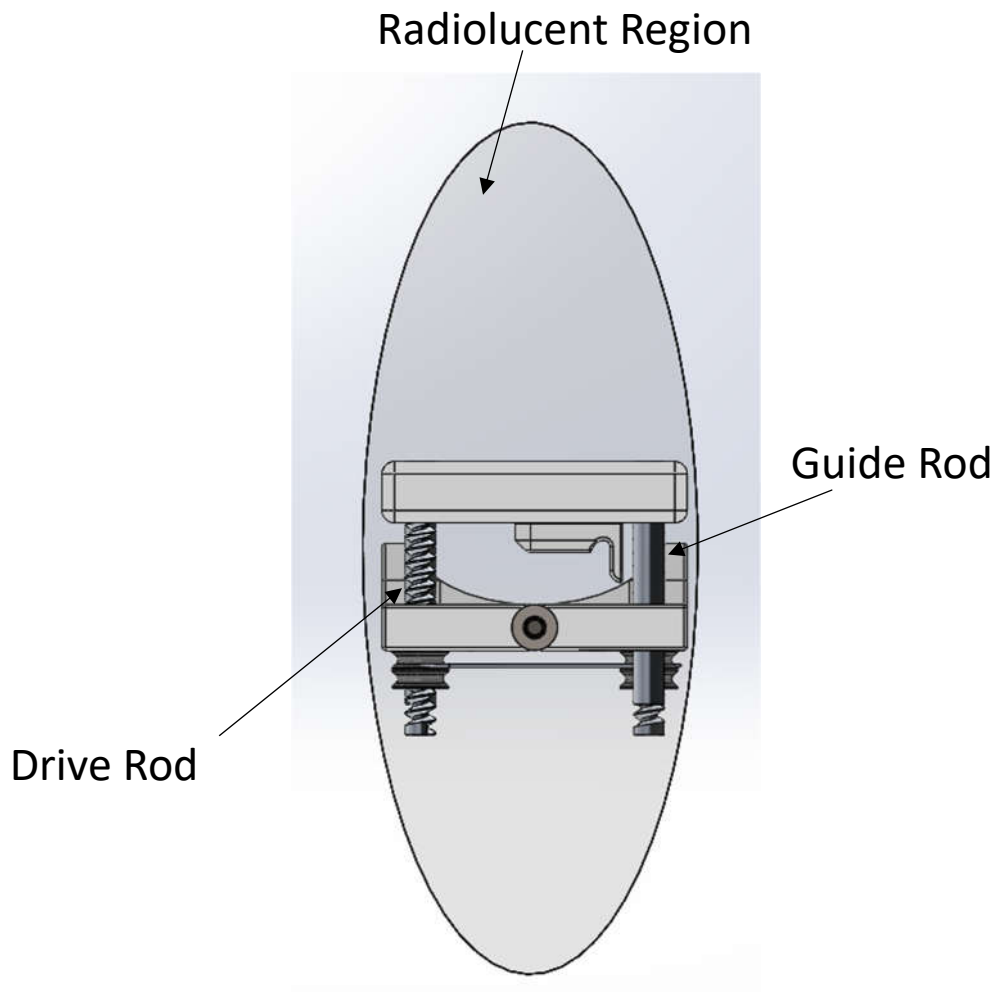
Sustainability

Sustainability covers material, financial, and usage considerations for the device. The material utilized is glass-fiber reinforced onyx for 3D printing. An environmental advantage that this plastic offers is that it is more sustainable in comparison to traditional plastics, which are petroleum based. Due to its superior processability with glass fiber and availability, glass fiber filled nylon is used in the prototype. Nylon is recyclable and low cost, and glass fiber is inert to the environment during post processing. Nylon is not ideal for the clinical setting due to its tendency to absorb moisture. Material properties and design considerations ensure that the device is safe for users and provides good ease of use.

Chapter 7 : Final Design and Validation

7.1 Overview of Final Design

The final design loads the distal radius in a three-point bending model. It consists of a base for the arm to rest upon and a piece driven by a screw drive mechanism to apply a force to the top of the wrist. Figures 7.1 a through d below, show several views of the CAD model generated in Solidworks for the final design. The major parts of the device are numbered and have in depth explanations.



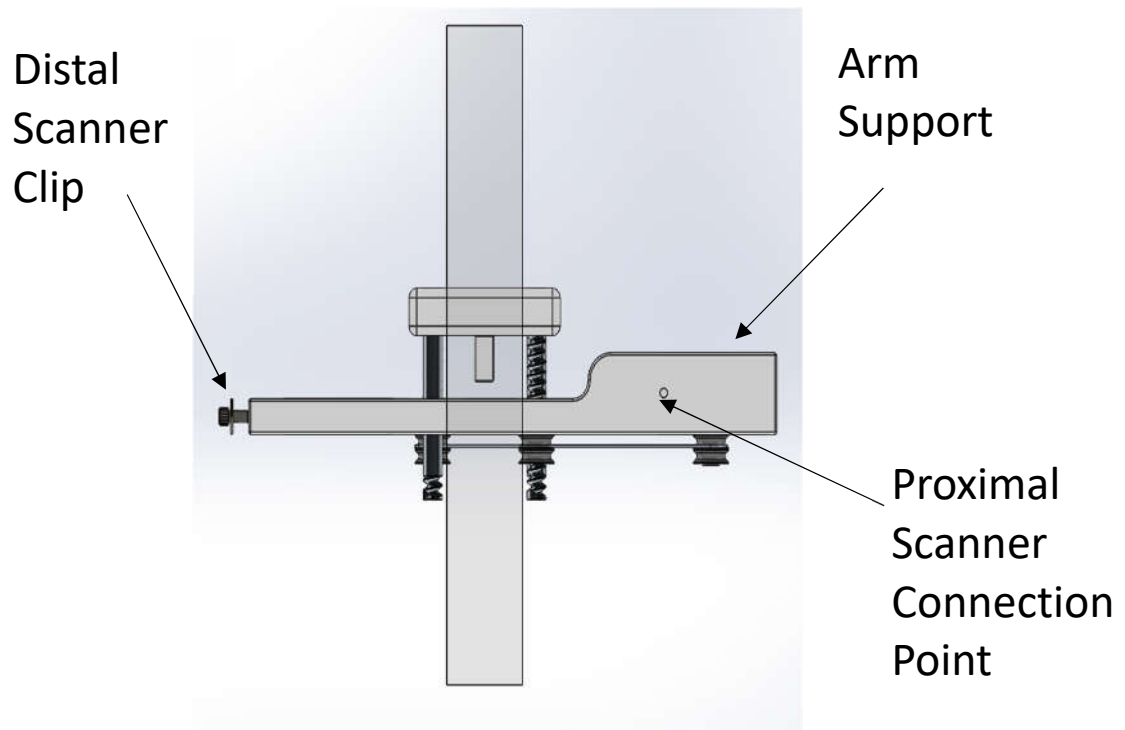


Figure 7.1 (a) Top image displaying the front plane view of the device. (b) Bottom image displaying the right view.

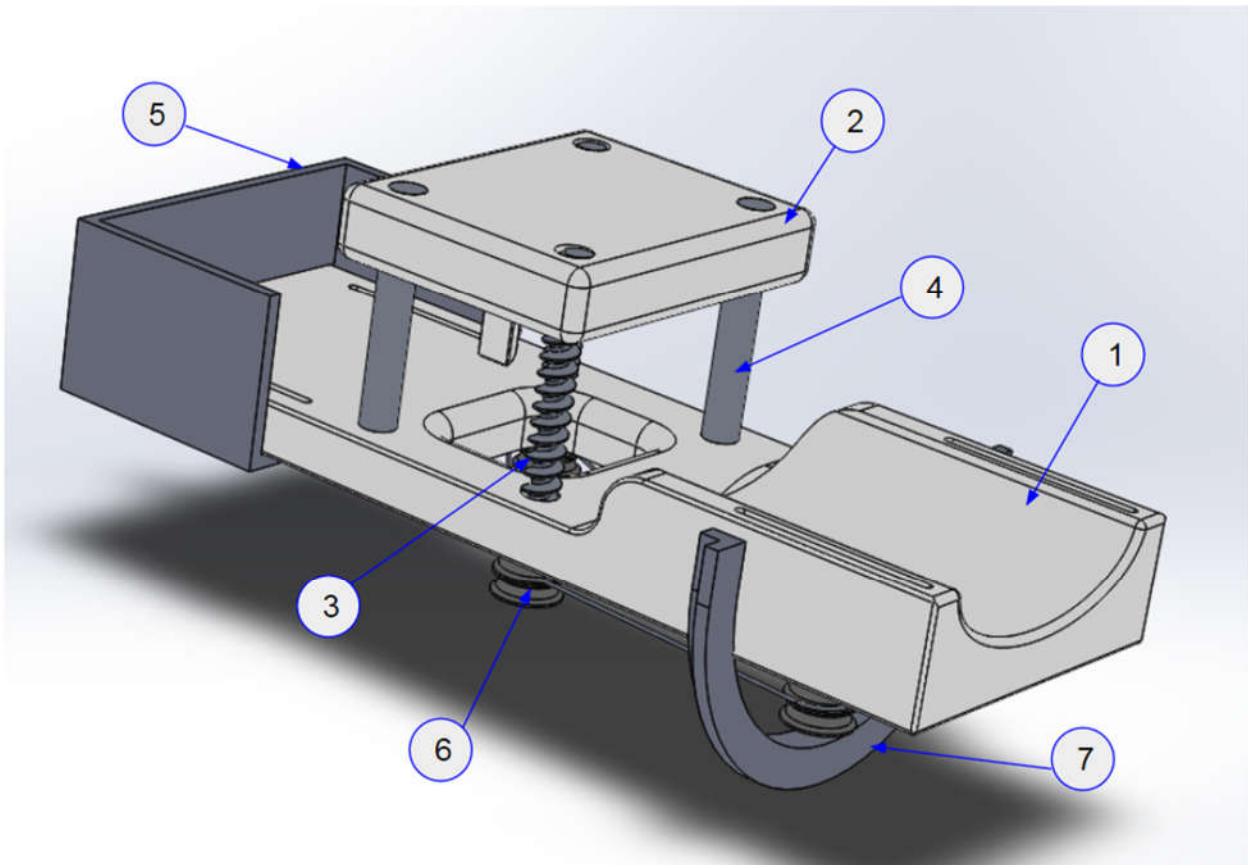


Figure 2 (c) device with the major parts numbered

Figure 7.1 (c) Image shows isometric view of the device with the major parts numbered. (b) image shows the front plane view of the device. (c) image shows the right plane view of the device. (d) Bottom image shows the bottom of the device with major parts numbered.

The parts of the design are:

1. **Base:** This provides a rigid, comfortable support for the arm, as shown and labeled in Figure 7.2. The cutout in the middle allows for the distal radius to be unsupported so that it can properly be loaded in 3-point bending to produce the necessary displacement of the bone. The base consists of the imaging section, the forearm rest, and the hand rest. The sections were printed separately due to space constraints in the printer and were attached using a glue. The forearm and hand rests are padded with a medium density closed-cell foam which is curved to fit the natural curves of the arm and hand. The arm support can be fitted with different thicknesses of padding from the standard SCANCO forearm cast to allow for it to be adjustable for varied arm sizes. The forearm and arm supports contain slots on the side, and hook and loop straps can be fed through the slots to help keep the patient's arm still and secure during the scan. On the distal end of the device is a screw

and washer which connects into the end of the machine. The proximal end contains a ring which sits on the two screws near the outside port of the machine.

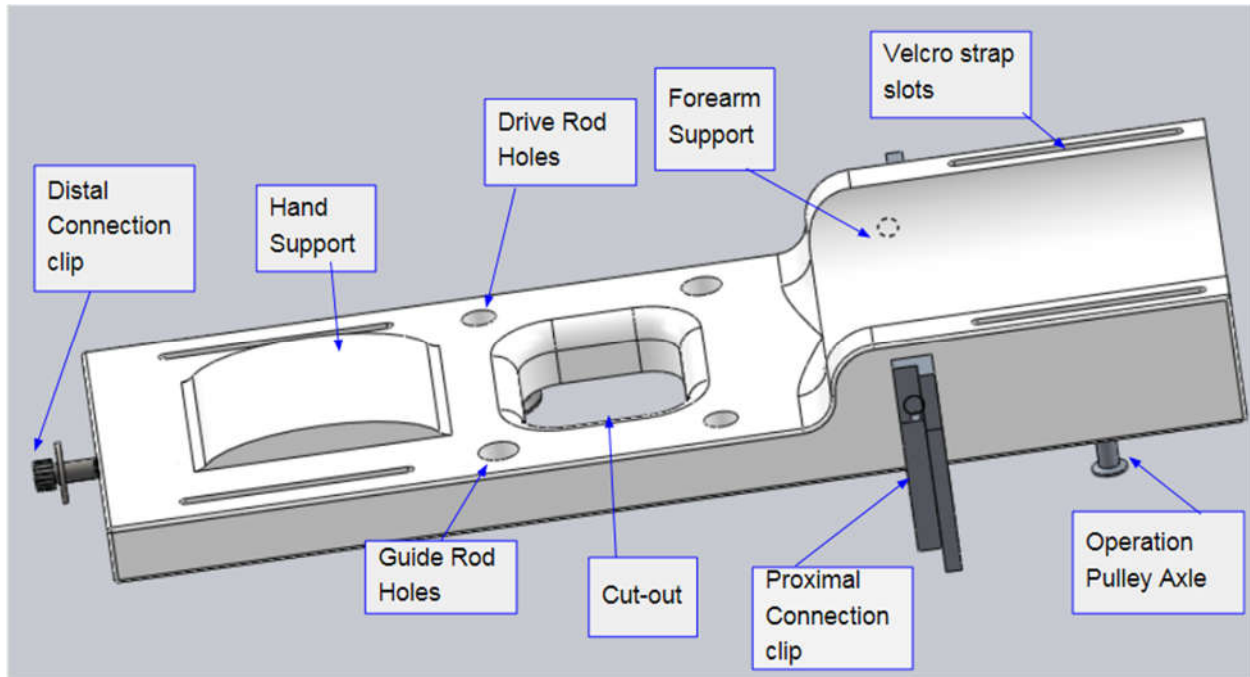


Figure 7.2 Isometric view of the base as a subassembly with associated parts

2. **Pressure Point:** This piece contains a lightly padded protruding surface, which applies the force to the wrist. The side of the piece contains a longer protrusion to line up with the styloid process on the side of the distal radius to allow for the arm to be properly lined up under the pressure point in a repeatable fashion. The pressure point is attached to a rectangular support, which contains threaded holes to allow for the movement up and down based on the turning of the screws. This piece is shown in Figure 7.3, below.

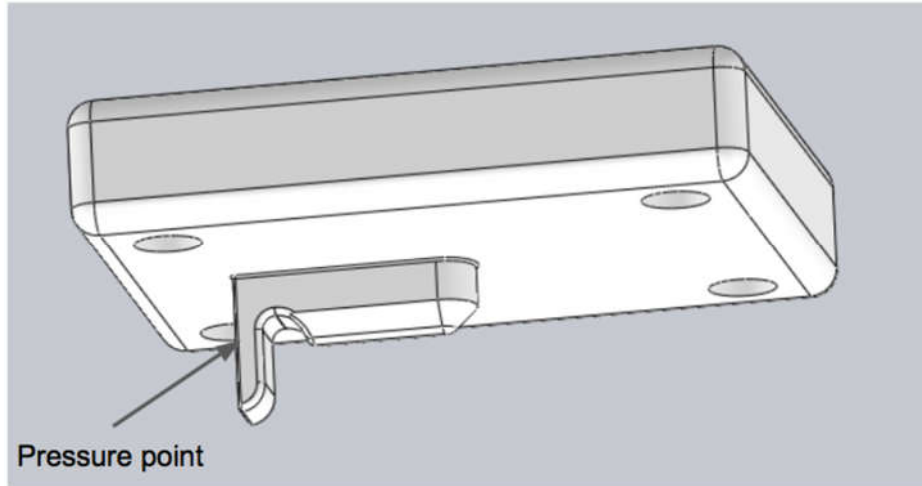


Figure 7.3 Diagram of the pressure point piece

3. *Screw drive*: Two steel $\frac{1}{2}$ - 20 inch threaded rods, 5.5 inches in length are used to drive the device. The threaded rods are fixed diagonally around the cutout into the base, but allow for rotation. The rods are to be threaded in the middle portion only where the pressure point piece must be driven up and down. The rods are retained using threaded nuts on the bottom of the device. Because the rods are made from standard metal materials, they are placed outside of the imaging region. This way, they could be readily available for purchase and would not require custom machining. In the case that localized stresses around the rods are excessive for the plastic, metallic inserts can be placed to bear the load. A rod with 200 threads per inch was chosen because preliminary testing showed that 13 threads per inch did not allow for enough fine force adjustment as maximum force was reached before a 180 degree turn of the rods. 220 threads per inch was the highest thread count commercially available. The rods are fixed, allowing for rotation into both the base and top support pieces. The pressure point piece is threaded onto the rod so that when the rod is turned the piece is driven downward to apply the force.
4. *Guide rods*: These $\frac{1}{2}$ in diameter non-threaded rods are Delrin and 5.5 inches in length. They are fixed into the top and base pieces. The pressure point piece moves in the z direction along them.
5. *Hand Guard*: This piece slides on around the end of the part to protect the hand in the case of any contact with the inside of the scanner.

6. *Push- pull pulley system:* The device is operable by a push-pull pulley system on the bottom of the base, as shown in Figure 7.4 below.

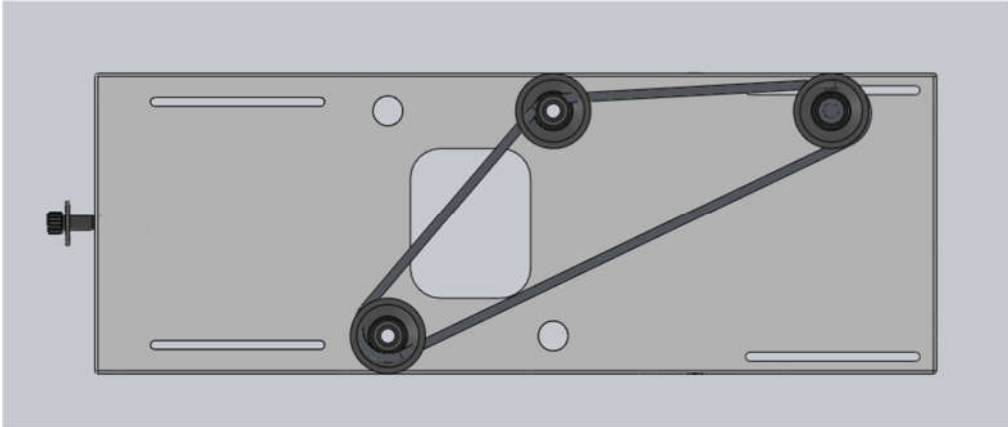


Figure 7.4 Bottom View of base piece detailing pulley system

On the bottom of each threaded rod is a rotatable pulley. The proximal end of the bottom of the base also contains a pulley. One nylon cord wraps around each of the pulleys. When the proximal pulley is turned, both drive rods rotate with the same strength. The cord is made from nylon because it is radiolucent allowing for it to not interfere with imaging as the cords pass under the imaging section. Nylon is strong and does not stretch as the pulley is operated. The pulley system is further discussed in Section 7.3.

7. *Proximal Connection*: This semi-circular structure rests on positioning posts outside the scanner opening. It supports the proximal end of the device for stillness and allows axial rotation and alignment in the scanner.
8. *Force Measurement system*: On the unthreaded portion of one of the drive rods, a strain gauge is placed, as shown in Figure 7.5a. This measures the tension in the rod and can be doubled to account for the other rod, as shown in the diagram in Figure 7.5b.

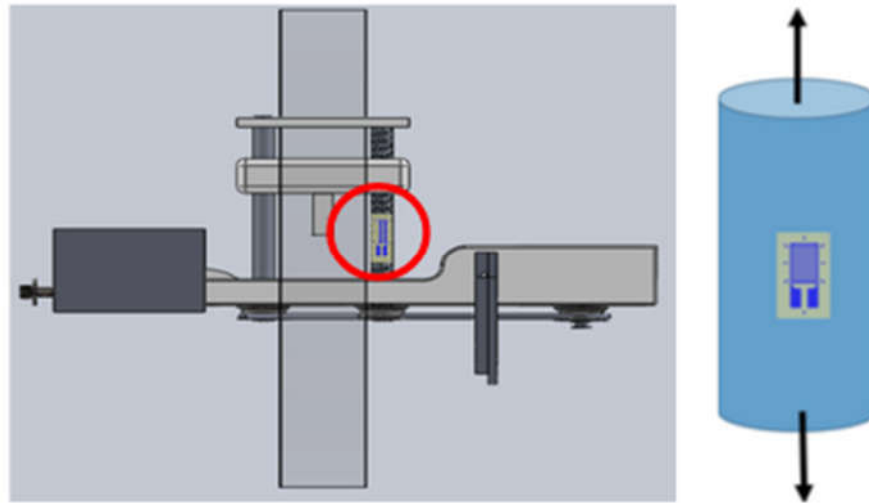


Figure 7.5 (a) The left image shows the position of the strain gauge on the device, as highlighted by the red circle. (b) the right image details the strain gauge on the unthreaded portion of the rod and the tension forces which it will measure.

The blue cylinder is a close-up view of the unthreaded portion of the rod and the arrows represent the tension forces on the rod, which the strain gauge measures. The strain gauge connected through a signal conditioning and amplifying circuit and Arduino DAQ system filter and amplify the resistive signal and convert it to a force output. This provides real-time feedback for the force present in the mechanism and applied to the patient.

7.2 Device Manufacturing

The loading region of the base, pressure point piece and top piece of the device was manufactured via 3D printing in Ara Nazarian's lab using Onyx, a filament made of glass fiber and nylon. This printer allows for the fiber to be laid in a 45-degree mesh, which increases the strength of the part. The team selected this manufacturing technique because the material allows for increased strength while maintaining radiolucency. This technique is also readily available and time efficient. Figure 7.6 displays the completed version of the device that was fabricated via 3D printing.

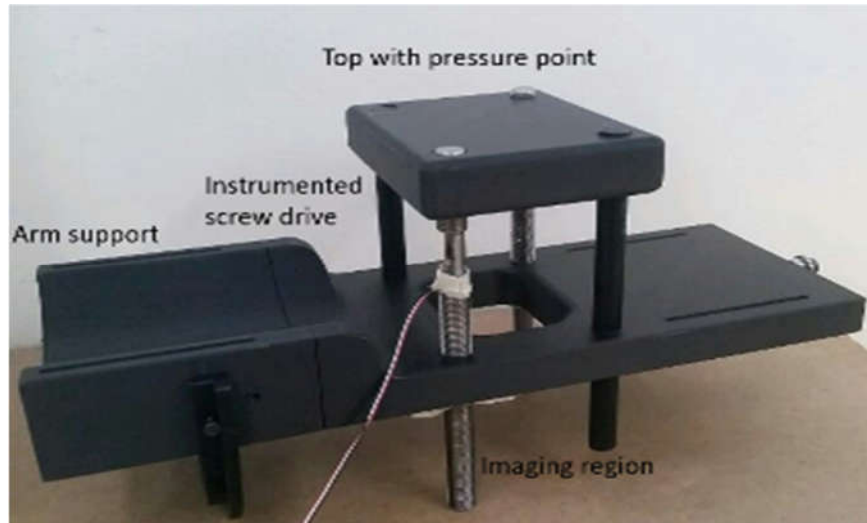


Figure 7.6 Completed version of the device that was fabricated via 3D printing

7.3 Device Operation

The device is operated by turning the rod on the side of the proximal end of the base. This connects via a short gear train to a push pull pulley system. As the proximal pulley is turned, one side of the cord is pushed towards the distal pulley, and the other side is pulled back causing rotation in the distal pulleys. As the distal pulleys are rotated together, the pressure point piece is moved linearly downwards, applying a compressive force to the sagittal surface of the wrist. As the compressive force is applied to the wrist, the heel of the hand and distal end of the forearm experience opposing reaction forces from the base piece, causing the 3-point bending. A CT image is then taken with the device in the loaded state so that the displacement of the bone can be seen. Once a visible displacement is achieved, the force used to reach this displacement allows the calculation of bending modulus which indicates the category of fracture healing. These ranges were determined through calculation of the stiffness of the bone with the given displacement and applied force and are presented previously.

The device measures mechanism force through use of a simple strain gauge instrumentation. A portion of the proximal drive rod is machined to accommodate a strain gauge. The strain gauge is connected to an amplifying and conditioning circuit. The output for this circuit can be read manually using a strain gauge or automatic disquisition can be accomplished using an Arduino Uno or other DAQ system. Code for the Arduino is provided in Appendix N. Calibration performed in the Instron machine generates a curve fit to correlate strain gauge reading to rod force. The mechanism force is twice that in the guide rod.

The instrumentation uses a 120 Ohm resistor from Miro-Measurements and a Stone and Webster signal conditioning and amplifying unit set in $\frac{1}{4}$ bridge configuration. Information on

settings and operation procedure can be found in Appendix S. Additionally, a standard multimeter, wires, electrical solder and connectors are used.

7.4 Future Recommendations to Improve the Design

Due to time constraints on this project, we have several recommendations for future work to improve the device. One major recommendation is to manufacture the device out of carbon fiber reinforced polycarbonate through injection molding. Due to lead times of injection molding through outside companies being a minimum of 4-6 weeks, this was not feasible for this project. An injection molded part would significantly increase the strength because the carbon fiber reinforcement in these plastics are in webs as opposed to the short-chopped fibers of 3D printing filaments. Increasing the strength through injection molding would also allow for a reduction in the amount of material in the imaging section through honeycombing. Honeycombing is not recommended for 3D printed parts because it would likely decrease the strength significantly due to the layered nature of the prints. Honeycombing to reduce material volume for injection molded parts was previously discussed in Chapter 4.

Some other design aspects which could be incorporated into a future design include a quick release system and a better force adjustment knob. A quick release system would allow for the loading to be immediately released back to zero instead of having to slowly decrease the load by turning the pulley in the opposite direction. A better force adjustment knob would potentially be located on the side of the device instead of the bottom for an easier reach for the physician. Several improvements could be made to the instrumentation and force measurement system of the device. Placing strain gauges on both rods would give a more accurate force reading. Using wireless strain gauges would allow for both rods to be instrumented, for the device to be easier to set up, and less space consuming. The instrumentation could be kept further away from the scanner allowing a more comfortable space for the patient.

7.5 Design Validation

Validation testing of the final 20 TPI drive mechanism was performed in the same manner as the initial 13 TPI model. The force equation was fitted to the data to provide force feedback. Figure 7.7 shows the calibration rod for the increased resolution drive mechanism. Significant improvement in force resolution was achieved, however more is desirable.

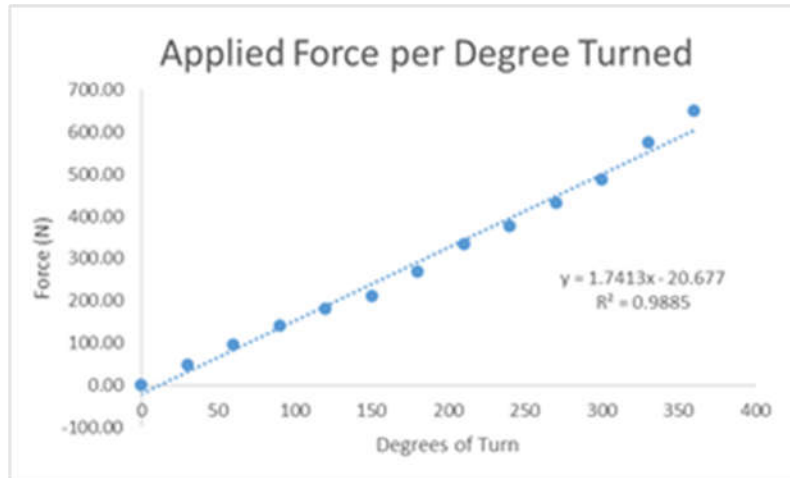


Figure 7.3 Graph displaying the applied force per degree turned

Validation testing using avian specimens with the device in the CT scanner were performed. The goals of these tests were to demonstrate sufficient radiolucency, image clarity, positioning, and displacement of bones in the device. Protocols can be found in Chapter 5. Two separate trials were attempted with avian specimens. All relevant biosafety practices were followed. The first trials imaged both a calibration phantom and an avian specimen in the device. Sufficient radiolucency was determined in these tests as shown in Figure 7.8, below.

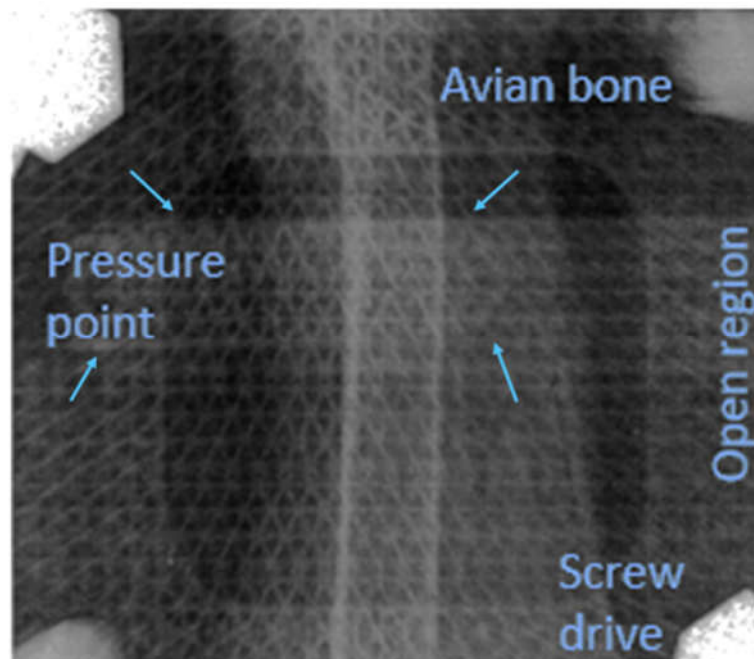


Figure 7-4 Validation testing using avian specimens

The first trials also placed a cut in the distal trabecular region of the avian specimen and imaged it loaded and unloaded. Results from this testing were inconclusive because the specimen was next to, not under the pressure point, resulting in no bending. Similarly, the second set of

tests were performed with another specimen with a cut in it. Due to a problem with the instrumentation setup, the forces applied were significantly higher than intended and the bone cracked completely during the first loading before it could be imaged. The metaphyseal region of this bone was then attempted to be imaged in loaded and unloaded states. Deflection was not demonstrated as review of the images showed that the bone had rotated about the long axis, so like regions were not able to be compared in bending. Better fixation methods are necessary for future testing to stabilize the bone. Additionally, biological equivalent phantoms can be used to perform this testing as well. The problem of rotation and positioning is not anticipated to be present in human applications. Biosafety considerations required the specimens to be encased in plastic, preventing ease of visualization, and making the setup internally slippery. In living humans, these considerations are not present, and higher precision is easily obtainable in positioning. Additionally, radio markers can be taped to anatomical markers, and other anatomical markers typically used in HR-pQCT scans can be used to perform alignment in the images. Figure 7.9a shows the avian specimen positioned and loaded in the device and Figure 7.9b displays the device loaded into the CT scanner.



Figure 7-5 (a) shows the specimen loaded in the device (b) shows the device loaded into the CT scanner

Figure 7.10a shows a reconstructed 3D model of the bone after processing in Mimics software. Figure 7.10b shows a reconstructed image of the flesh and bone loaded by the pressure point in the device after processing with Mimics software.

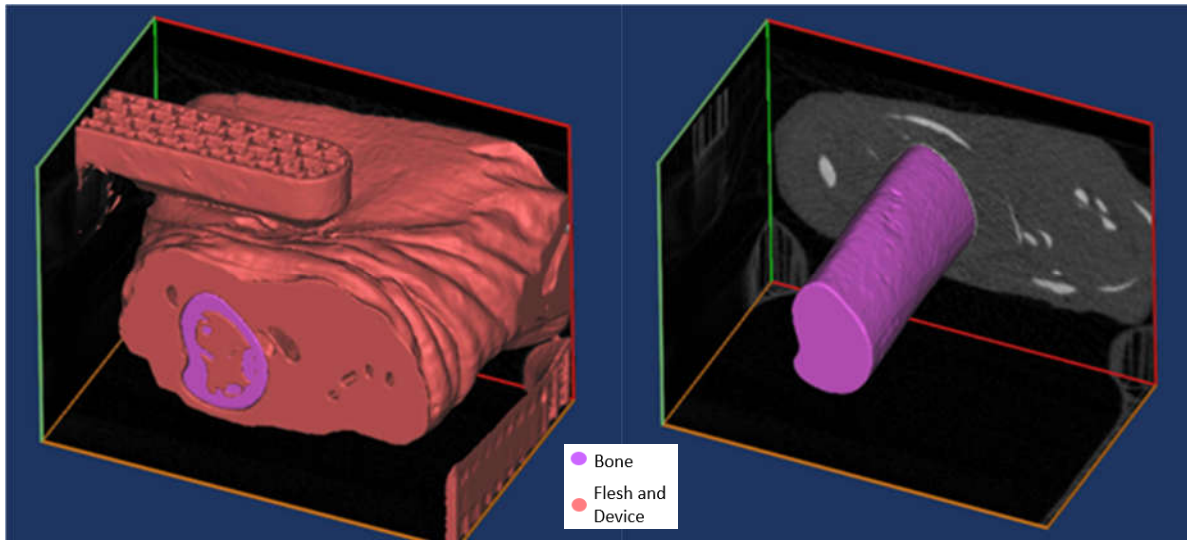


Figure 7-6 (a) shows the specimen loaded in the device (b) shows the device loaded into the CT scanner

These images can be processed to separate regions of different radio density and thus select material types. It is possible to perform direct spatial measurements in Mimics or to create input files for finite element analysis. Both techniques are used in current research to quantify mechanical properties of bone in vivo. In this case, deflection was not demonstrated, however it would be clear with softer materials such as healing bone.

Above are presented the validation tests performed with the final device and their results. All main project objectives were met and presented.

Chapter 8 Conclusion and Recommendations

Through final validation testing, it was found that the final device design is able to produce all mechanical forces and provide all instrumentation needed quantify the extent of strength recovery in distal radius fractures, meeting the project objectives. Validation testing proved that the device was able to withstand more than a sufficient amount of force to obtain a visible and safe displacement in the CT scanner. Material selection and stress analysis of the device allowed for it to be rigid enough to resist deformation under the necessary force levels. The comfort level of the device, measure on the Self-Assessed pain scale was tolerable enough for a patient to remain still. Further clinical trials are needed to assess discomfort changes in injured individuals. Testing inside the CT scanner proved that the device is radiolucent, and compatible with the CT scanner. Removal and reattachment of the pressure point piece allows for right/ left compatibility. The device was manufactured via 3D printing with glass fiber reinforcements, a material which allows for the device to be cleanable by a disinfectant wipe down.

Despite not being able to measure the bone displacements in the images due to limitations and variables in the avian bone testing, this device is sufficiently advanced to provide further validation with better test specimens. Future steps for this device include the design changes proposed in Section 7.4, improvements to manufacturing, further work on automation and image processing, along with continued work on validation testing, preclinical and clinical testing.

The device was manufactured via mark-forge 3d printing in onyx with glass fiber reinforcement due to time and material constraints. Future work on the device could manufacture via injection molding in carbon fiber reinforced polycarbonate. Polycarbonate is strong and would allow for a complete carbon fiber web to maintain strength and better dimensional stability over time. For the device to reach the market, injection molding would be a cheap and easy way to produce it in large numbers.

The device could be automated to increase ease of use for doctors and technicians. Automation of the load application would make the device operation simpler for the technician to activate to various force levels quickly, simply and from a further distance away. This could also include a better user interface for the instrumentations, which automatically displays the force as determined via calibration. This would be much simpler than reading the millivolts off of the voltmeter and converting to Newtons. Automation of the image process through a machine learning algorithm could more rapidly process the images, measure bone displacement and calculate the callus strength at the given force. This would greatly reduce the time and labor

necessary for image processing and calculations to allow for patients and doctors to get near real-time diagnoses.

Due to the time constraints on the project, further validation testing is necessary for the final design. Avian bone testing could be continued with efforts taken to reduce the difficulties and variables encountered in testing. A mark could be placed on the bone to help ensure accurate alignment in the scanner. Cutting partial fractures less far across the bone could reduce the potential for the bone to fully break. Dissecting back some of the soft tissue of the avian leg would help the bone to fit properly into the device and be more representative of a human arm geometry.

Further IRB approved testing with human subjects would better assess the comfort and sizing of the device. The proposed protocol for this procedure can be found in Appendix K. Testing on uninjured human cadaver arms can also better validate fit, scanning ability and displacement production.

After these improvements and further validations testing are made, the device can move into the clinical trials stage. This will allow for testing on alive, and healing fractured wrists to be done. This will fully validate the displacement production, and ability to quantify the strength recovery of the distal radius. FDA approval for the device will also be necessary for use in live humans. After successful clinical trials the device can be implemented in the clinical space in the hopes of better informing fracture treatment and decreasing the need for surgery. The device can also be used to research and better understand how distal radius fracture healing occurs, particularly in osteoporotic elderly women. This can then be used to better inform treatment of other fractures and bone injuries in this populations.

Citations

- [1] Meena, S., Sharma, P., Sambharia, A. K., & Dawar, A. (2014). Fractures of Distal Radius: An Overview. *Journal of Family Medicine and Primary Care*, 3(4), 325–332.
- [2] Habeebullah, A., Vasiljevic, A., & Abdulla, M. (2015). Evidence-based review of Colles' fracture. *Trauma*, 17(3), 191-200.
- [3] Cooney, W. 3., Dobyns, J. H., & Linscheid, R. L. (1980). *Complications of Colles' fractures. J Bone Joint Surg Am*, 62(4), 613-619.
- [4] Nellans, K. W., Kowalski, E., & Chung, K. C. (2012). The Epidemiology of Distal Radius Fractures. *Hand Clinics*, 28(2), 113–125.
- [5] Shah, H. M., & Chung, K. C. (2008). Robert William Smith: His Life and His Contributions to Medicine. *The Journal of Hand Surgery*, 33(6), 948-951.
- [6] Epidemiology. (2015). Retrieved September, 2016, from <https://www.iofbonehealth.org/epidemiology>
- [7] Kakarlapudi, T. , et. al(2000). The cost of treatment of distal radial fractures. *Injury*, 31(4), 229-232.
- [8] Elvin, M. (2009, June 22). Distal Radius Fractures of the Wrist: Avoiding Complications with Proper Diagnosis and Treatment. Retrieved September 27, 2016, from https://www.hss.edu/conditions_distal-radius-fractures-of-the-wrist.asp
- [9] Nyary, T., & Scammell, B. E. (2015). *Principles of bone and joint injuries and their healing. Surgery (Oxford)*, 33(1), 7-14.
- [10] Liporace, F. A., et al (2009). Distal radius fractures. *Journal of orthopaedic trauma*, 23(10), 739-748.
- [11] Walsh, C. R. (2013). Wrist fractures in adults. *Nursing*, 43(4), 38-45.
- [12] Distal Radius Fractures (Broken Wrist). (2013, March). Retrieved September, 2016, from <http://orthoinfo.aaos.org/topic.cfm?topic=A00412>
- [13] Wolfe, S. (2009). Distal Radius Fractures of the Wrist: Avoiding Complications with Proper Diagnosis and Treatment. Retrieved September, 2016, from https://www.hss.edu/conditions_distal-radius-fractures-of-the-wrist.asp
- [14] Orthopedic Teaching. (2014). Retrieved from <http://ortho-teaching.feinberg.northwestern.edu/cases/wrist/case4/index.html>
- [15] Gaillard, F. (n.d.). Smith fracture. Retrieved September, 2016, from <https://radiopaedia.org/articles/smith-fracture>
- [16] Porrino, Jr, J. (2015, October 20). Distal Radial Fracture Imaging. Retrieved September, 2016, from <http://emedicine.medscape.com/article/398406-overview>

- [17] Henry MH. Distal radius fractures: current concepts. *J Hand Surg Am.* 2008 Sep. 33(7):1215-27.
- [18] Samir, B. (n.d.). Distal radial fracture with ulnocarpal dislocation | Radiology Case | Radiopaedia.org. Retrieved 2016, from <https://radiopaedia.org/cases/distal-radial-fracture-with-ulnocarpal-dislocation>
- [19] Martínez-Díez, J. (2014). Complex Fractures of the Distal Radius. *Complex Fractures of the Limbs*, 29-35.
- [20] Diaz-Garcia, R. J., & Chung, K. C. (2012). Common Myths and Evidence in the Management of Distal Radius Fractures. *Hand Clinics*, 28(2), 127–133.
- [21] Bone Remodeling and Repair. (n.d.). Retrieved September, 2016, from <https://www.boundless.com/biology/textbooks/boundless-biology-textbook/the-musculoskeletal-system-38/bone-216/bone-remodeling-and-repair-819-12062/>
- [22] White III, A. A., Punjabi, M. M., & Southwick, W. O. (1977). The Four Biomechanical Stages of Fracture Repair. *The Journal of Joint and Bone Surgery*, 59A, 188-192.
- [23] A Closer Look At The Potential Of Bone Lengthening Distraction Osteogenesis. (2016, May). Retrieved October, 2016, from <http://www.podiatrytoday.com/closer-look-potential-bone-lengthening-distraction-osteogenesis>
- [24] Romo, E., et al. (2008). Modeling distraction osteogenesis: Analysis of the distraction rate. *Biomechanics and Modeling in Mechanobiology*, 8(4), 323-335.
- [25] Computed Tomography (CT). (2014). Retrieved October, 2016, from <http://www.fda.gov/Radiation-EmittingProducts/RadiationEmittingProductsandProcedures/MedicalImaging/MedicalX-Rays/ucm115317.htm>
- [26] Ogbole, G. (2011). Radiation dose in paediatric computed tomography: Risks and benefits. *Annals of Ibadan Postgraduate Medicine*, 8(2).
- [27] Systems & Solutions: XtremeCT. (n.d.). Retrieved September, 2016, from <http://www.scanco.ch/en/systems-solutions/clinical-microct/xtremect.html>
- [28] LaBarbera, J. (1999). U.S. Patent No. 6,885,550. Washington, DC: U.S.
- [29] Morgan, E. F. (2009). Micro-computed tomography assessment of fracture healing: Relationships among callus structure, composition, and mechanical function. *Bone*, 44(2), 335-344.
- [30] Nellans, K. W., Kowalski, E., & Chung, K. C. (2012). The Epidemiology of Distal Radius Fractures. *Hand Clinics*, 28(2), 113–125.
- [31] Littlewood, R. (n.d.). The Benefits and Risks of The Ilizarov Technique For Limb Reconstruction. Retrieved September 28, 2016.

- [32] Krebs, E. E., Carey, T. S., & Weinberger, M. (2007). Accuracy of the Pain Numeric Rating Scale as a Screening Test in Primary Care. *Journal of General Internal Medicine*, 22(10), 1453-1458.
- [33] Chen, E. J. (1996). Young's modulus measurements of soft tissues with application to elasticity imaging. *IEEE Transactions on Ultrasonics, Ferroelectrics and Frequency Control*, 43(1), 191-194.
- [34] Romo, E., et al. (2008). Modeling distraction osteogenesis: Analysis of the distraction rate. *Biomechanics and Modeling in Mechanobiology*, 8(4), 323-335.
- [35] Radiolucent Structural Materials for Medical Applications. (2001, June 1). Retrieved October 01, 2016, from <http://www.mddionline.com/article/radiolucent-structural-materials-medical-applications>
- [36] Nellans, K. W., Kowalski, E., & Chung, K. C. (2012). The Epidemiology of Distal Radius Fractures. *Hand Clinics*, 28(2), 113–125.
- [37] Gaillard, F. (n.d.). Smith fracture. Retrieved September, 2016, from <https://radiopaedia.org/articles/smith-fracture>
- [38] Advantages and Disadvantages of Different Types of Gears. (2012). Retrieved October 03, 2016, from http://www.green-mechanic.com/2014/05/advantages-and-disadvantages-of_7.html
- [39] Kong, S., Sharif, K., Evans, H., & Snidle, R. Elastohydrodynamics of a Worm Gear Contact. *ASME. J. Tribol.* 2000;123(2):268-275.
- [40] Rack and Pinion. (n.d.). Retrieved December, 2016, from <http://etc.usf.edu/clipart/187000/187076/187076-rack-and-pinion.htm>[Text Wrapping Break]
- [41] About Smalley Wave Springs. (2016). Retrieved October 04, 2016, from <http://www.smalley.com/about-smalley-wave-springs>
- [42] Pavani, P., Prafulla, B., Rao, R. P., & Srikanth, S. (2014). Design, Modeling and Structural Analysis of Wave Springs. *Procedia Materials Science*, 6, 988-995.[Text Wrapping Break]
- [43] Pulley. (n.d.). Retrieved November, 2016, from http://etc.usf.edu/clipart/49900/49929/49929_pulley-f1-2.htm
- [44] Advantages & Disadvantages of Pulleys. (n.d.). Retrieved October 6, 2016, from <http://pulleymanufacturer.com/advantages-disadvantages-of-pulley.htm>
- [45] Pugh Matrix. (n.d.). Retrieved September 29, 2016, from <http://www.whatissixsigma.net/pugh-matrix/>
- [46] First Class Lever. (n.d.). Retrieved December, 2016, from http://etc.usf.edu/clipart/20000/20054/classonelevr_20054.htm[Text Wrapping Break]
- [47] Hammond, F. L., Smith, M. J., & Wood, R. J. (2014). Printing Strain Gauges on Surgical Instruments for Force Measurement. *Journal of Medical Devices*, 8(3).[Text Wrapping Break]

- [48] Load Cell: Introduction to Load Cells. (n.d.). Retrieved November, 2016, from <http://www.omega.com/prodinfo/loadcells.html>[Text Wrapping Break]
- [49] Lebosse, C., Renaud, P., Bayle, B., & Mathelin, M. (2011). Modeling and Evaluation of Low-Cost Force Sensors. *IEEE Transactions on Robotics*, 27(4), 815-822.
- [50] Load Cell Vs. Force Sensor. (n.d.). Retrieved November, 2016, from https://www.tekscan.com/resources/ebook/load-cell-vs-force-sensor-2?utm_expid=98649966-8.vk4qMKfbSuGZAFxmCki0NQ.1&utm_referrer=https%3A%2F%2Fwww.google.com%2F
- [51] Economical Beam Bending Load Cells. (n.d.). Retrieved November, 2016, from <http://www.omega.com/pptst/LCEA.html>
- [52] Chung, K.C. and S.V. Spilson, The frequency and epidemiology of hand and forearm fractures in the United States. *J Hand Surg Am*, 2001. 26(5): p. 908-15.
- [53] Rho, J. Y. (1993). Young's modulus of trabecular and cortical bone material: Ultrasonic and microtensile measurements. *Journal of Biomechanics*, 26(2), 111-119.
- [54] Gibson, L. J., & Ashby, M. F. (1999). *Cellular solids: structure and properties*. Cambridge university press.
- [55] Christensen, R. M. (2000). Mechanics of cellular and other low-density materials. *International Journal of Solids and Structures*, 37(1), 93-104.
- [56] Gibson, L. J., Ashby, M. F., Schajer, G. S., & Robertson, C. I. (1982, July). The mechanics of two-dimensional cellular materials. In *Proceedings of the Royal Society of London A: Mathematical, Physical and Engineering Sciences* (Vol. 382, No. 1782, pp. 25-42). The Royal Society.
- [57] United States Bone and Joint Initiative: The Burden of Musculoskeletal Diseases in the United States (BMUS). (2014). Retrieved January, 2017, from <http://www.boneandjointburden.org>
- [58] McKay, S. D., MacDermid, J. C., Roth, J. H., & Richards, R. S. (2001). Assessment of complications of distal radius fractures and development of a complication checklist. *The Journal of hand surgery*, 26(5), 916-922.
- [59] Knight, C., Zeng, C., Zhang, C., Wang, B. (2012). Recycling of woven carbon-fibre-reinforced polymer composites using supercritical water. *Journal of Environmental Technology*, 33(4).
- [60] Corn Starch Plastic – The 7 Advantages and Disadvantages of its Use. (n.d.). Retrieved January, 2017, from <http://www.bionomicfuel.com/corn-starch-plastic-the-advantages-and-disadvantages/>

Appendix

The appendix is split into eleven sections including:

- A. Summary of spending
- B. Criteria for evaluating the different loading types
- C. Tension Design Matrix Rubric
- D. Bending Design Matrix Rubric
- E. Testing Results for the elbow gripping mechanisms
- F. Experimental Testing for the hand gripping mechanisms
- H. Results of the Load Cell Linearity Tests

- I. Arduino Code

- J. Subject Data Sheet and Procedure - Fracture Healing MQP Device Comfort & Ergonomics Study
- L. IRB Flyer
- M. Avian Testing

- N. Matlab Code used for Prototype Force Testing Graphs
- O. Pressure Sensitive Film Testing
- P. Results of Pressure Sensitive Film Testing
- Q. Results of Comfort Testing with the Bending Design
- R. Bill of Materials for the Updated Bending Design Prototype
- S. Strain Gauge and instrumentation Setup and Use
- T. Engineering Drawings of Device and Components

A. Summary of spending

The team has spent \$146.38 for project items. The athletic tape and velcro were utilized for selecting the best hand gripping mechanism. Similarly, the blood pressure cuff, elbow brace, and dial twist were used to compare potential elbow gripping mechanisms, and the Thermomorph plastic pellets were implemented into the design to create a bony contact inset for the elbow. Furthermore, the load cells were purchased earlier in the term to determine the amount of force that is being applied to the bone. Meanwhile, the multimeter was used to measure the voltage that takes place in the load cell when a mechanical load is applied to a fracture. The team has been able to obtain an Arduino Circuit board and the Futek Load Cell for free via Professor Troy's Lab.

Table A.1: Amount that the team has spent

Category	Object	Vendor	Price
----------	--------	--------	-------

Accessories	Lab Notebook	WPI	\$6
	Wrist	SawBones (website)	\$31.67
	Hanging Weights	WPI	Free
Initial Prototype			
	Blood Pressure Cuff	Amazon	\$11.95
	Mueller Adjustable Elbow Support	Amazon	\$11.69
	Dial Twist	Full Source	\$10.74
	Thermomorph Moldable Plastic Pellets	Amazon	\$18.95
	Multimeter	Amazon	\$6.95
	Load Cell Strain Gauge	Amazon	\$8.28
	50 kg Beam Load Cell	Amazon	\$13.99
	OP- AMP Weighing Sensor	Amazon	\$8.99
	Steel screws for the load cell	Barrows Hardware Store	\$2.17
	Wood and metal screws	Home Depot	\$15.00
			\$146.38

B. Criteria for evaluating the different loading types

1. Ability to apply a repeatable force

Rationale: For a device to apply a known force the same way every time, the loading type should be both reproducible and reliable.

- A score of 1: This loading type is neither reliable nor reproducible. Variation will likely be seen between uses.
- A score of 2: This loading type is moderately reliable and reproducible. It will apply the same known force to the same location most times.
- A score of 3: This loading type is highly reliable and reproducible. It will provide the same force to the same location as anticipated just almost every time.

2. Ability to apply a non-damaging force

Rationale: It is crucial that the loading type does not damage or delay healing of the patient. Furthermore, the loading type needs to be able to support complete healing of the distal radius fracture.

- A score of 1: This loading type is unable to apply a non-damaging force to the patient. The loading type will likely result in further injury to the patient or will deter the healing process.
- A score of 2: This loading type is somewhat able to apply a non-damaging force to the patient, and it will apply a non-damaging force to the patient most of the time.
- A score of 3: This loading type can apply a non-damaging force to patient at all time. Furthermore, this loading type will be able to support complete and quicker fracture healing.

3. Ability to open the healing fracture

Rationale: It is crucial that the loading type is able to sufficiently open up the healing fracture to produce a detectable displacement. This displacement will allow the team to evaluate the amount that the fracture has healed.

- A score of 1: This loading type is unable to open the healing fracture, and unable to produce a detectable displacement
- A score of 2: This loading type is adequate in its ability to open the healing fracture and in its ability to produce a detectable displacement. Additionally, the loading type would be able to open the healing fracture most of the time.
- A score of 3: This loading type can open the healing fracture and produce a detectable displacement almost all of the time.

C. Tension Design Matrix Rubric

1. Loading Reliability & Reproducibility

Weight: 4

Rationale: For a device to apply a known force the same way every time, the loading mechanism must be both reproducible and reliable.

- A score of 1: This device is neither reliable nor reproducible. Variation will likely be seen between uses. Large numbers of moving parts will decrease reliability of a design.
- A score of 2: This design is somewhat reliable and reproducible. It will apply the same known force to the same location most times.
- A score of 3: This device is highly reliable and reproducible. It will provide the same force to the same location as anticipated just almost every time.

2. Space Constraints

Weight: 4

Rationale: The device must fit inside the scanner opening in order to be used within the CT scanner. The displacement of the fracture ends will be unmeasurable without the CT scanner.

- A score of 1: This design will not fit within the necessary constraints on dimensions unless altered in some way.
- A score of 2: This design is bulky, but will still fit within the constraints
- A score of 3: This design will fit without difficulty or alterations.

3. Range of Force

Weight: 3

Rationale: The device needs to be able to apply a wide range of forces in order to determine which range the healing fracture is in. The device will also need to be able to apply these forces which are in the correct range of force.

- A score of 1: This device will likely not be able to cover the entire force range, or will not allow for variability to encompass the necessary range of forces.
- A score of 2: This device will be able to provide most of the range of force necessary for early and intermediate fracture healing stages.
- A score of 3: This device will expand beyond the necessary force range for a healing fracture.

4. Ease of Use

Weight: 3

Rationale: Physicians/technicians need to be able to operate the device without too much difficulty, and to learn how to use the device in a reasonable amount of time.

- A score of 1: This device could potentially require a trained specialist to run, or will take a long duration of time for physicians/ technicians to learn and operate.
- A score of 2: This device will take physicians/ technicians an amount of time to learn that is comparable to other technologies they use already. It will not require a trained specialist.
- A score of 3: This device will not take a lot of time to learn, and will not require much physician/technician input to operate.

5. Fine Adjustment

Weight: 2

Rationale: In the tension loading design, it is not crucial that the device has good fine adjustment because of the magnitude and large range of forces provided.

- A score of 1: This device will likely not have good fine adjustment at all. It may be difficult to apply very specific forces.
- A score of 2: This device has moderate fine adjustment abilities.
- A score of 3: This device has good fine adjustment and will allow for specific forces to be achieved.

6. Rigidity

Weight: 2

Rationale: The device must be somewhat rigid in order to allow force application through very compliant soft tissue. The device must also be rigid enough to remain stable and motionless during the loading to prevent motion artifact on the scanner image.

- A score of 1: This device is not very rigid and will likely deflect or distort during loading.
- A score of 2: This device is relatively rigid enough to provide a stable platform for the arm to be placed during loading.

- A score of 3: This device is very rigid which promotes good stability and no movement.

7. Cast Compatibility

Weight: 1

Rationale: This criteria is considered as a “nice to have” and not a “must have” for a successful design. While

it would be beneficial, it is not necessary for the device to successfully function.

- A score of 1: This device will not be cast compatible
- A score of 2: This device could be cast compatible depending upon certain design specifications, or will have partial function on a casted arm.
- A score of 3: This device can fully function on a casted arm.

8. Cost Effectiveness

Weight: 1

Rationale: Due to outside funding, in addition to WPI’s departmental project funding, a higher cost to produce the device is not a large strain on the project.

- A score of 1: This device will exceed the school budget and use the outside funding.
- A score of 2: This device will total a price within the school budget.
- A score of 3: This device will total a price within $\frac{3}{4}$ of the school budget.

D. Bending Design Matrix Rubric

1. Loading Reliability & Reproducibility

Weight: 4

Rationale: For a device to apply a known force the same way every time, the loading mechanism must be both reproducible and reliable.

- A score of 1: This device is neither reliable nor reproducible. Variation will likely be seen between uses. Large numbers of moving parts will decrease reliability of a design.
- A score of 2: This design is somewhat reliable and reproducible. It will apply the same known force to the same location most times.

- A score of 3: This device is highly reliable and reproducible. It will provide the same force to the same location as anticipated just almost every time.

2. Space Constraints

Weight: 4

Rationale: The device must fit inside the scanner opening in order to be used within the CT scanner. The displacement of the fracture ends will be unmeasurable without the CT scanner.

- A score of 1: This design will not fit within the necessary constraints on dimensions unless altered in some way.
- A score of 2: This design is bulky, but will still fit within the constraints
- A score of 3: This design will fit without difficulty or alterations.

3. Range of Force

Weight: 3

Rationale: The device needs to be able to apply a wide range of forces in order to determine which range the healing fracture is in. The device will also need to be able to apply these forces which are in the correct range of force.

- A score of 1: This device will likely not be able to cover the entire force range, or will not allow for variability to encompass the necessary range of forces.
- A score of 2: This device will be able to provide most of the range of force necessary for early and intermediate fracture healing stages.
- A score of 3: This device will expand beyond the necessary force range for a healing fracture.

4. Ease of use

Weight: 3

Rationale: Physicians/technicians need to be able to operate the device without too much difficulty, and to learn how to use the device in a reasonable amount of time.

- A score of 1: This device could potentially require a trained specialist to run, or will take a long duration of time for physicians/ technicians to learn and operate.
- A score of 2: This device will take physicians/ technicians an amount of time to learn that is comparable to other technologies they use already. It will not require a trained specialist.

- A score of 3: This device will not take a lot of time to learn, and will not require much physician/technician input to operate.

5. Ergonomics

Weight: 3

Rationale: The device needs to be comfortable to the patient, and this is an area that can be optimized and improved upon in Magdalena's design. Furthermore, it is crucial that the device does not cause pain or discomfort to the patient.

- A score of 1: This device would be uncomfortable, and can cause pain to the patient.
- A score of 2: This device is sufficiently comfortable to the patient, and would likely not cause pain.
- A score of 3: This device is quite comfortable, and the design will not cause pain or discomfort to the patient.

6. Fine Adjustment

Weight: 2

Rationale: For the bending design, it is not as crucial that the device has good fine adjustment abilities because of the magnitude and large range of forces provided.

- A score of 1: This device will likely not have good fine adjustment at all. It may be difficult to apply very specific forces.
- A score of 2: This device has moderate fine adjustment abilities.
- A score of 3: This device has good fine adjustment and will allow for specific forces to be achieved.

7. Rigidity

Weight: 2

Rationale: The device must be somewhat rigid in order to allow force application through very compliant soft tissue. The device must also be rigid enough to remain stable and motionless during the loading to prevent motion artifact on the scanner image.

- A score of 1: This device is not very rigid and will likely deflect or distort during loading.
- A score of 2: This device is relatively rigid enough to provide a stable platform for the arm to be placed during loading.
- A score of 3: This device is very rigid which promotes good stability and no movement.

8. Radiolucency

Weight: 1

Rationale: The design needs to be transparent to X-rays so that the displacement that occurs in the healing fracture can be determined. This design requirement was rated a 1 because only a portion of the device needs to be radiolucent.

- A score of 1: The device is not transparent to X-rays and a Technician/Physician cannot determine the displacement that occurs in the healing fracture.
- A score of 2: The device is mostly transparent to X-rays, and a Technician can determine how much the healing fracture has opened.
- A score of 3: The device is completely radiolucent.

9. Cost Effectiveness

Weight: 1

Rationale: Due to outside funding, in addition to WPI's departmental project funding, a higher cost to produce the device is not a large strain on the project.

- A score of 1: This device will exceed the school budget and use the outside funding.
- A score of 2: This device will total a price within the school budget.
- A score of 3: This device will total a price within $\frac{3}{4}$ of the school budget.

E. Testing Results for the elbow gripping mechanisms

Tables A.2 - A.4 displays results for experimental testing of the elbow gripping mechanisms. A pattern that was noticed during testing is that the blood pressure cuff had a higher slip in comparison to the other options, and the bony contact brace was able to withstand greater mechanical forces.

Table A.2: Experimental data for the elbow brace

Trial Number	Subject Name	Mechanism Used	Hand (L/R)	Mass (g)	Maximum Slip (mm)	Discomfort Level (1-10)
1	Ahmed	Brace with tape	R	50 g		2
				400 g		2
				600 g	Slight slip of 2 mm	3

				800 g	2.13 mm	3
				1000 g	2.43 mm	3
				1200 g	2.54 mm	3
				1550 g (15.1 N)	2.74 mm	3
				2100 g	3.68 mm	4
				2600 g (25.4 N)	5.57 mm	5
2	Hannah	Brace with tape	R	50 g		1.5
				400 g		1.5
				600 g	1.47 mm	1.5
				800 g	1.55 mm	1.5
				1000 g	1.60 mm	2
				1200 g	1.81 mm	2
				1550 g (15.1 N)	2.78 mm	3
				2100 g	3.77 mm	4
				2600 g	4.10 mm	4.5
				3200 g (31.4 N)	4.35 mm	5
3	Jennifer	Brace with tape	R	200 g		1
				400 g		1

				600 g		1
				800 g		1
				1000 g		1
				1200 g		1
				1550 g (15.1 N)	0.78 mm	1
				2100 g	1.28 mm	1
				2600 g	1.49 mm	1
				3200 g (31.4 N)	2.02 mm	2
				3700 g	2.30 mm	2 (slightly worse)
				4200 g	2.61 mm	2
				4700 g	2.77 mm	3
				5200 g	3.05 mm	4
				5700 g	3.42 mm	5

Table A.3: Experimental data for the blood pressure cuff

Trial Number	Subject Name	Mechanism Used	Hand (L/R)	Mass (g)	Maximum Slip (mm)	Discomfort Level (1-10)
4	Ahmed	BP cuff	R	200 g & 46 mmHg		1
				400 g		1
				600 g	1.2mm	1
				800 g	5.8mm	2

				1000 g	5.58 mm	2
				1200 g	5.81 mm	2
				1550 g (15.1 N)	5.57 mm	3
				2100 g	6.98 mm	3.5
				2600 g	7.18 mm	4
				3200 g	9.04 mm	4.5
				3700 g	9.77 mm	5 (loss of circulation was noted)
5	Hannah	BP Cuff	R	200 g & 35 mm Hg		1
				400 g		1
				600 g		1
				800 g		2
				1000 g	1.62 mm	2
				1200 g	1.74 mm	3
				1550 g	2.88 mm	3
				2100 g	3.08 mm	4
				2600 g	9.85 mm	5
6	Jennifer	BP Cuff	R	200 g & 50 mmHg		1
				400 g		1

				600 g		1
				800 g		1
				1000 g	1.67 mm	1
				1200 g	2.15 mm	1
				1550 g	2.96 mm	2
				2100 g	3.92 mm	3
				2600	5.14 mm	4
				3100 g	5.72 mm	4
				3600 g	6.25 mm	4
				4100 g	6.45 mm	4
				4600 g	7.05 mm	5 (Loss of circulation)

Table A.4: Experimental data for the bony contact brace

Trial Number	Subject Name	Mechanism Used	Hand (L/R)	Mass (g)	Maximum Slip (mm)	Discomfort Level (1-10)
7	Ahmed	Bony Contacts for the Elbow	R	200 g		1
				400 g		1
				600 g		1
				800 g		1
				1000 g		1

				1200 g		1
				1550 g	1.52 mm	2
				2100 g	2.02 mm	3
				2600 g	1.82 mm	3
				3100 g	2.32 mm	4
				3600 g	4.1 mm	5
8	Hannah	Bony Contacts for the Elbow	R	200 g		1
				400 g		1
				600 g		1
				800 g		1
				1000 g		1
				1200 g		1
				1550 g	1.6 mm	2
				2100 g	1.82 mm	3
				2600 g	2.15 mm	3
				3100 g	3.01 mm (plastic part seems to be slipping)	4
				3600 g	4.43 mm	4
				4100 g	9.51 mm	5

9	Jennifer	Bony Contacts for the Elbow	R	200 g		
				400 g		
				600 g		
				800 g		
				1000 g		
				1200 g		
				1550 g		
				2100 g		
				2600 g		
				3100 g		
				3600 g		
				4100 g		

F. Experimental Testing for the hand gripping mechanisms

Table A.5 displays experimental data for the athletic tape finger brace.

Table A.5: Experimental data for the athletic tape finger brace

Trial Number	Subject Name	Mechanism Used	Hand (L/R)	Mass (g)	Maximum Slip (mm)	Discomfort Level (1-10)
1	Hannah		R	200 g		1
				400 g		1

				600 g		1
				800 g		1
				1000 g		1
				1200 g		1
				1550 g	Slip inside the fingers	1
				2100 g	Pulling more towards thumbs (0.92 mm)	1
				2600 g	1.60 mm	2
				3100 g	1.86 mm	2
				3600 g	2.98 mm	3
				4100 g	Serious slip inside fingers and thumb (4.13 mm)	3
				4600 g	4.70 mm	4
				5100 g	4.85 mm	4
				5600 g	4.85 mm	5

G. Experimental images for the elbow gripping mechanisms

Figures A.1-A.3 depict images for testing the elbow brace, blood pressure cuff, and bony contact brace. In these experimental tests, the team tested each elbow gripping component on a team member.



**1) Elbow
Brace**



**2) Blood Pressure
Cuff**



**3) Bony Contact
Brace**

Figure A.1: Experimental images for testing the elbow brace, blood pressure cuff, and bony contact brace on Ahmed



**1) Elbow
Brace**



**2) Blood
Pressure
Cuff**



**3) Bony
Contact
Brace**

Figure A.2: Experimental images for testing the elbow brace, blood pressure cuff, and bony contact brace on Hannah



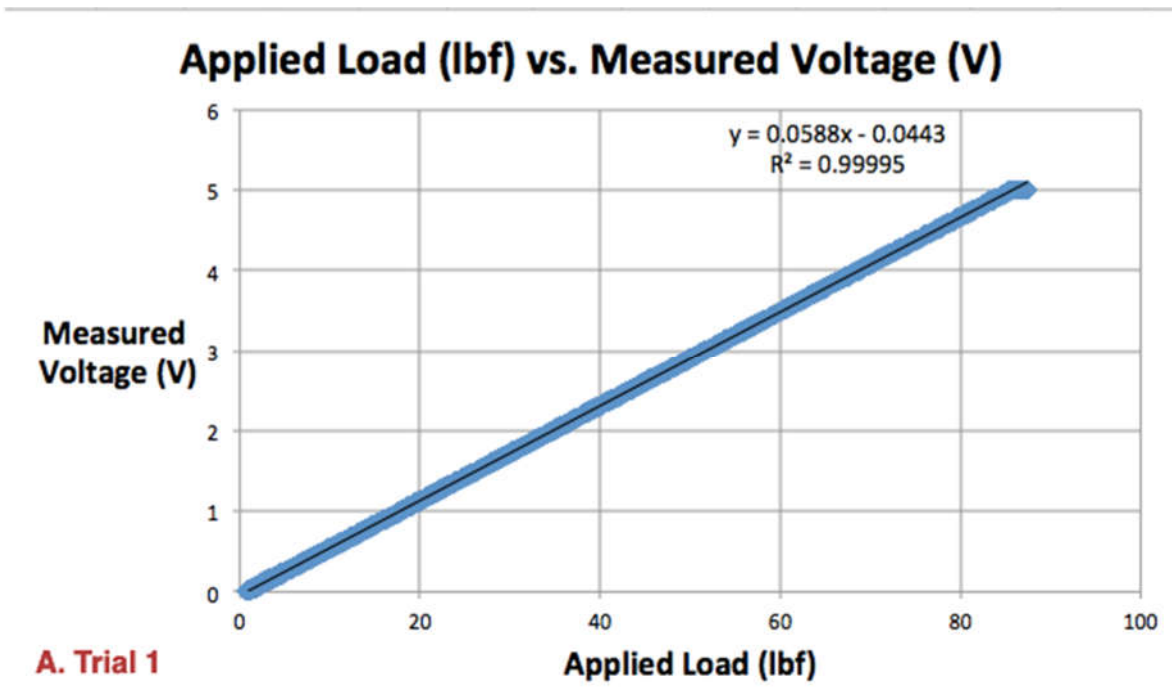
1) Elbow
Brace

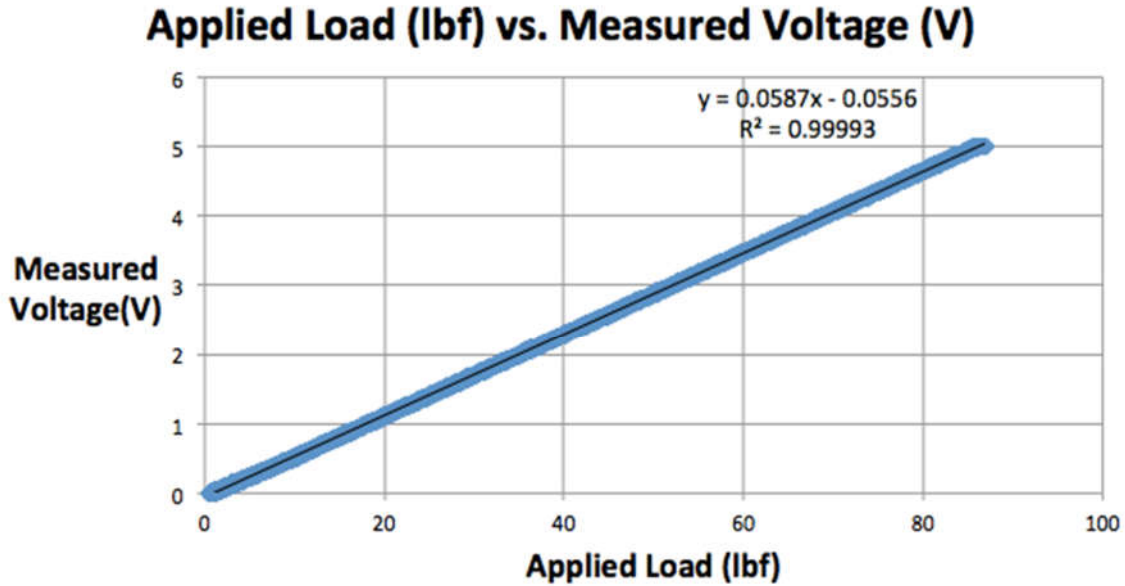
2) Blood
Pressure
Cuff

Figure A.3: Experimental images for testing the elbow brace, blood pressure cuff, and bony contact brace on Jennifer

H. Results of the Load Cell Linearity Tests

The results of the Load Cell Linearity tests for all of the trials are indicated in Figure A. 4





B. Trial 2

Figure A. 4: Results of the Load Cell Linearity Test for Trials 1 and 2.

I. Arduino Code

/*

Code was adapted from: AnalogReadSerial

Reads an analog input on pin 0, prints the result to the serial monitor.

Attach the center pin of a potentiometer to pin A0, and the outside pins to +5V and ground.

Supplies 5 V of power and reads output voltage drop in the serial monitor.

*/

// the setup routine runs once when you press reset:

```
void setup() {
```

```
  // initialize serial communication at 9600 bits per second:
```

```
  Serial.begin(9600);
```

```
  // analogReference(INTERNAL); //Delete for full range
```

```
  while (!Serial) {
```

```
    ; // wait for serial port to connect. Needed for native USB port only
```

```
  }
```

```
}
```



```

// the loop routine runs over and over again forever:
void loop() {
  // read the input on analog pin 0:
  int sensorValue = analogRead(A5); //set to input pin
  sensorValue = map(sensorValue, 0, 1023, 0.000, 5000); // maps sensor value from 0 to 5 volts
  // print out the value you read:
  Serial.println(sensorValue);
  delay(100);    // delay in between reads for stability
}

```

J. Subject Data Sheet and Procedure - Fracture Healing MQP Device Comfort & Ergonomics Study

Subject information:

Study ID	
Age	
Biological Sex	

Subject Anatomical Measurements:

Wrist circumference		Wrist diameter	
Hand length		Hand thickness	
Hand width			
Forearm circumference		Forearm diameter	
Upper arm circumference		Upper arm diameter	
Forearm length		Distal radius width	

Testing Data:

Force level: N/lb	Pain level during loading	Pain level after loading	Comments:
50/11.2			
100/22.5			
150/33.7			

200/45.0			
250/56.2			
300/67.4			
350/78.7			
400/90.0			
450/101.2			
500/112.4			
550/123.6			
Post-procedural pain level:			

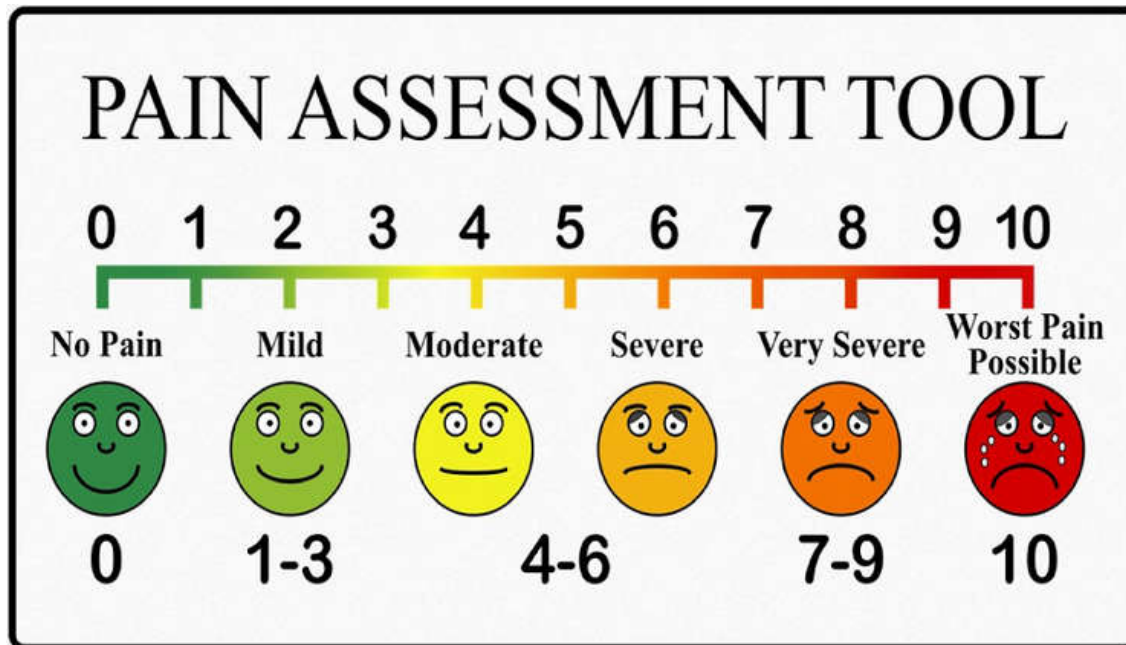
Subject feedback on experience:

Procedure

Before Test:

The subject will be given an initial questionnaire to fill out and will be asked to provide gender, age, height, and weight. The subject will then be given an overview of the self-assessed pain scale.

The self-assessed pain scale is a rating of 1-10 used for a person to describe the level of pain or discomfort that they are experiencing. This is used by doctors to determine how much pain a patient is feeling. On this scale, a 1 is the lowest and is comparable to a small papercut. Meanwhile, a 10 is the highest and is comparable to an unbearable amount of pain.



During this test you will be asked to place your arm inside this device. The intended use of this device is to measure how well a wrist fracture is healing. We are focusing on evaluating how comfortable the device is for the patient.

Preparation:

1. You will be asked to self-report biological sex and age.
2. The following measurements may be taken:
 - a. wrist circumference
 - b. forearm circumference (at any point(s) on the forearm)
 - c. hand size
 - d. elbow circumference
 - e. upper arm circumference
 - f. width of the distal radius, as assessed by palpation
 - g. forearm length

Initial Test:

1. We will place your arm inside an arm-holder that is being tested.
2. You will be asked to rate your discomfort level on a scale of 1 to 10. You may be asked to provide additional detail.

Loaded Test:

3. *A small amount of weight (11 lbs) will be placed across your wrist. And you will be asked to rate your discomfort level again.*
4. *Weight will be increased by 11 pounds. Each time it is increased, we will ask you about your discomfort.*
5. *You can ask to stop any time if you want to. Otherwise, the test will stop when you report a discomfort level of 5 or a weight of 123 pounds is reached.*

Final Questions:

We will ask you for your overall opinion on the comfort of the device and procedure. We will also ask you to share any specific feedback you may have on The pain you experience during this study, as previously mentioned, will not exceed your rating of 5 on the self-assessed pain scale from 1 to 10. If, at any moment, you wish to cease the experiment you should request to do so and we will decrease the force to zero and remove your arm immediately. The pain levels experienced during this study should subside immediately or shortly after the force is removed. Again, the pain levels are not high enough to cause any lasting damage or injury to you.

After this explanation is read, we will take and record measurements of the subject. These dimensions will be done using common measuring devices: calipers, rulers, or tape measures. Dimensions measured will be:

- a. Wrist circumference and diameter
- b. Hand dimensions
- c. Forearm circumference and diameter at any point along the forearm
- d. Elbow dimensions
- e. Upper arm circumference and diameter
- f. Full arm and arm segment(s) length(s)
- g. Width of the distal radius, which will be measured by palpating between the radius and ulna

Experimental Test:

The subject will be asked to place his/her arm inside the device. We will first ask the subject to evaluate how comfortable the device is without applying any force using a rating on the self-assessed pain scale from 1-10 along with any comments on the comfort or ergonomics of the device. All subject responses will be recorded.

Then, we will apply a force to the subject's wrist using the device in 50 N (approximately 11 lbs)

increments up to 550 N (approximately 123 lb), which will be held for no more than one minute. The subject will be asked to evaluate his/her discomfort level during and after the load application. The force will be increased in increments and the subject will be asked to rate his/her discomfort level at each force. At each force the subject will be given a maximum time of 30 seconds to decide upon a discomfort rating so that the force is not prolonged. The force will not return to zero in between loadings, and will increase consistently. The testing will stop when one of the following criteria is reached:

- a. We reach the maximum necessary force of 550 N.
- b. Subject reports a discomfort level of 5
- c. Subject requests the experiment to be stopped

After the Test:

Following completion of the test, we will ask the subject to give any general opinions on the device relating to patient comfort. We will ask the subject to elaborate upon discomfort levels and point out any specifics on the type of pain and the exact location of pain. We will ask them to give a discomfort level for any pain they are feeling following the procedure

K. Informed Consent Agreement for Participation in a Research Study

Investigator: Karen Troy, Ph.D.

Contact Information: ktroy@wpi.edu

Title of Research Study: Fracture Healing MQP

Sponsor: Center for Advanced Orthopedic Studies: Beth Israel Deaconess Medical Center

Introduction:

You are being asked to participate in a research study. Before you agree, however, you must be fully informed about the purpose of the study, the procedures to be followed, and any benefits, risks, or discomfort that you may experience as a result of your participation. This form presents information about the study so that you may make a fully informed decision regarding your participation.

Purpose of the study:

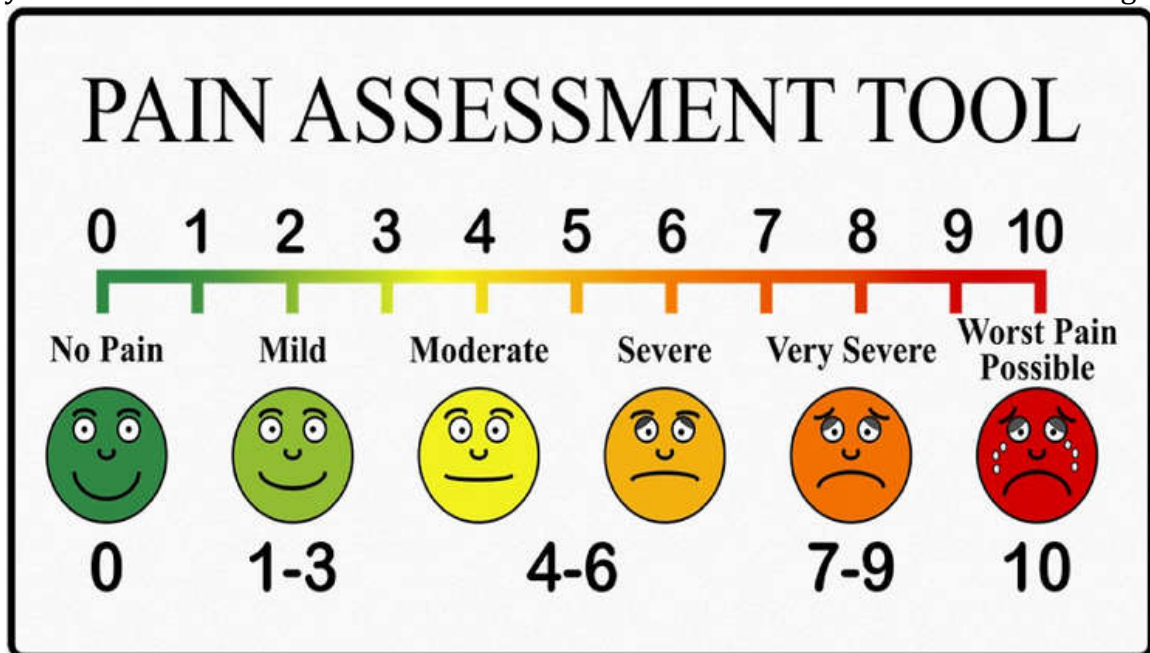
This Major Qualifying Project (MQP) Project Team is developing a device which will measure the extent of bone healing in wrist fractures. This study will evaluate patient comfort and ergonomics before, during, and after force applications.

Procedures to be followed:

Preparation:

1. You will be asked to self-report biological sex and age on a paper and pencil survey.
2. The following measurements will be taken:
 - a. wrist circumference
 - b. forearm circumference (at any point(s) on the forearm)
 - c. hand size
 - d. elbow circumference
 - e. upper arm circumference
 - f. width of the distal radius, as assessed by palpation
 - g. forearm length

The self-assessed pain scale subject seen in the picture below, will be explained to you. This is what we will use to for discomfort ratings.



Initial Test:

1. We will place your arm inside an arm-holder that is being tested.
2. You will be asked to rate your discomfort level on a scale of 1 to 10. You may be asked to provide additional detail.

Loaded Test:

3. A small amount of weight (11 lbs) will be placed across your wrist. And you will be asked to rate your discomfort level again.
4. Weight will be increased by 11 pounds. Each time it is increased, we will ask you about your discomfort.
5. You can ask to stop any time if you want to. Otherwise, the test will stop when you report a discomfort level of 5 or a weight of 123 pounds is reached.

Final Questions:

We will ask you for your overall opinion on the comfort of the device and procedure. We will also ask you to share any specific feedback you may have on

Risks to study participants:

You can expect some discomfort, but it will not have any major or lasting damage on your arm. You may experience some minor redness, soreness, or bruising in the area following the procedure, which should go away after a maximum time of a few hours or days. If you are concerned about your well-being, you are encouraged to see your healthcare provider. Keep in mind that you can ask to stop the test at any time you want to.

Benefits to research participants and others:

There are no direct benefits or compensation for your participation in this study. The information gathered will benefit the body of scientific knowledge and contribute to the development of a medical device that may improve wrist fracture treatment and recovery in the future. This project serves as the capstone project of undergraduate Engineering students and aids us in our degree completion. Thank you for helping us with our project.

Record keeping and confidentiality:

We will record your age and biological sex as provided by you prior to the start of the experiment. Additionally, we will record measurements of your arm, as detailed in the procedure. Your discomfort assessments will be recorded, along with general observations of the experiment from both the subject and the investigators.

All recording will be done on one paper and pencil survey per person. These will be saved on the investigator's password-protected laptop as well as in the team lab notebook and will be kept by the project advisor, Karen Troy, Ph.D., after completion of the project and until analysis is complete.

Your name will be recorded but not released. Confidentiality of any health concerns will be maintained. Subjects will be assigned study identifiers and the key will be maintained in a password protected file. Records of your participation in this study will be held confidential so far as permitted by law. However, the study investigators, the sponsor or its designee and, under certain circumstances, the Worcester Polytechnic Institute Institutional Review Board (WPI IRB) will be able to inspect and have access to confidential data that identify you by name. Any publication or presentation of the data will not identify you.

Compensation or treatment in the event of injury:

This research provides only minimal risk to the subject, but in the event of any injury or harm, you do not give up any of your legal rights by signing this statement.

Cost/Payment:

There are no anticipated costs to you for this study. Compensation is not provided. Snacks or refreshment may be offered to thank you for your participation.

For more information about this research or about the rights of research participants,

or in case of research-related injury, contact:

Primary Investigator (Faculty Advisor): Karen Troy, Ph.D, Tel. 508-831-6093, Email: ktroy@wpi.edu)

Student team:

Jennifer Golden, Tel. 508-463-5825, Email: jlgolden@wpi.edu

Ahmed Hakim, Tel. 508-981-7114, Email: afhakim@wpi.edu

Hannah Sattler, Tel. 603-285-1669, Email: hesattler@wpi.edu

IRB Chair (Professor Kent Rissmiller, Tel. 508-831-5019, Email: kjr@wpi.edu) University Compliance Officer (Jon Bartelson, Tel. 508-831-5725, Email: jonb@wpi.edu)

Your participation in this research is voluntary:

Your refusal to participate will not result in any penalty to you or any loss of benefits to which you may otherwise be entitled. You may decide to stop participating in the research at any time without penalty or loss of other benefits. The project investigators retain the right to cancel or postpone the experimental procedures at any time they see fit.

By signing below, you acknowledge that you have been informed about and consent to be a participant in the study described above. Make sure that your questions are answered to your satisfaction before signing. You are entitled to retain a copy of this consent agreement.

Study Participant Signature

Date: _____

Study Participant Name (Please print)

Signature of Person who explained this study

Date: _____

Additional clauses to add to Consent Agreements, as appropriate:

An additional cost to the subject that may result from participation in this research includes time, as it will take approximately 10-15 minutes to perform the experimental tests.

Significant new findings or information, developed during the course of the research, may alter the subject's willingness to participate in the study. Any such findings will be promptly communicated to all research participants.

Should a participant wish to withdraw from the study after it has begun, the subject can contact any member of the team listed above. There will be no consequences for early withdrawal for the subject. The subject may wish to withdraw from the study at any point in time.

Special Exceptions:

Under certain circumstances, an IRB may approve a consent procedure which differs from some of the elements of informed consent set forth above. Before doing so, however, the IRB must make findings regarding the research justification for different procedures (i.e. a waiver of some of the informed consent requirements must be necessary for the research is to be "practicably carried out.") The IRB must also find that the research involves "no more than minimal risk to the subjects." Other requirements are found at 45 C.F.R. §46.116.

L. IRB Flyer



WPI



Research Subjects Wanted!

This research is conducted by the Fracture Healing MQP Team in the second floor of Goddard Hall.

Recruiting NOW
Through MAR 2017



Medical Device Ergonomics Study

Are you a **healthy** adult between the ages of **18 -65** years. Would you like to participate in a research study to determine the **ergonomics of a device** that measures how much a distal radius fracture has healed?

For more details about this study, please contact fracturemqp@wpi.edu. The members of the Fracture Healing MQP team include: Jennifer Golden, Hannah Sattler, and Ahmed Hakim

Snacks will be provided!

M. Avian Testing

The goal of this test is to evaluate the localized forces/pressures applied by the device loading region to the arm.

Force Measurement Procedure

1. Position arm in the device.
2. Place sheet pressure sensors under the arm at the distal and proximal cutout edges.
3. Place sheet sensors between the top of the arm and the pressure point.
4. Verify that sensor connection and acquisition is active by wiggling arm against sensors.
5. Slowly apply loading to the arm by tightening the drive rods. Turn rods by the same increment each time.

6. Provide calibration curve analysis to correlate rotational drive distance with patient experienced force/pressure .
7. Repeat above a minimum of three times.
8. Use information in later testing to determine forces applied.

Displacement Procedure

The avian test will be completed in Room 1040 (CT imaging room) of Gateway Park. During the test, we will apply a force of up to 550 N (~ 123 lbs). Based on calculations, we expect that this will produce a displacement of up to 165 microns (0.165 mm), which is equivalent to 2 voxels in the HR-pQCT scanner. The steps for avian testing are shown below.

All relevant biohazardous materials safety procedures will be followed.

Specimen preparation:

Allow frozen specimen to come to room temperature in a Saline bath for _ Hours.

1. Wrap specimen in sealed plastic to prevent contamination.
2. Position specimen in device, under the force application piece, so that the articular end of the distal radius is supported by the distal edge of the device cutout and the pressure point is over common fracture region. Use safety gloves.
3. Tighten device just until the non-loading contact is achieved with upper and lower surfaces of the arm.
4. Insert the device onto the connection clips of the CT scanner.
5. Insert the device into the scanner.
6. Verify positioning of device and specimen using scout scan.
7. Take unloaded High Resolution (HR) image of specimen.
8. Retract and apply force increment
 - a. Apply a force of 50 N (~ 11 lbs) to the avian bone and increase the weight up to 550 N (~ 123 lbs); utilize increments of 50 N (~ 11 lbs).
9. Reinsert the device.
10. Verify positioning of the imaging region. Care should be taken to achieve maximum region of overlap.
11. Take loaded HR image of specimen.
12. Determine the displacement of the loaded cadaver arm by using the MicroCT software.

Clarity Procedure

1. Take a high resolution image of the cadaver arm in the clear specimen tray without the device for a baseline image.
2. Perform a HR non loading contact image as specified above.
3. Take care to provide high accuracy in repositioning.
4. Repeat this procedure for a broken cadaver arm.
5. Perform standard HR-pQCT analysis on both HR scans.
6. Determine percent variation for parameters between device and deviceless image.
7. Describe relevant observations in images.

Standard X-ray compatibility evaluation

1. Turn device onto side in scanner, repeat displacement test using only scout scans.
2. Evaluate bone position in scout images .
3. Measure bone displacement in scout images.
4. Present data for displacement and force in 2d image.
5. Provide recommendation concerning applicability of this method in standard 2D radiographs.

Repositioning error: repeatability can be as 60 %

If we can leave the arm in the machine, that will help with repeatability

N. Matlab Code used for Prototype Force Testing Graphs

```
%% Prototype Screw Force Testing
clear; close all; clc;
%% Load Arduino Data and convert mV to Force

ArduinomV1 = csvread('Run 1.csv');
Force1 = (ArduinomV1 - 412.15)/1.2392;

ArmV2 = csvread('Run 2.csv');
F2 = (ArmV2 - 412.15)/1.2392;

ArmV3 = csvread('Run 3.csv');
F3 = (ArmV3 - 412.15)/1.2392;

ArmV4 = csvread('Run 4.csv');
```

```

F4 = (ArmV4 - 412.15)/1.2392;

ArmV5 = csvread('Run 5.csv');
F5 = (ArmV5 - 412.15)/1.2392;
%% Create Time Vector
t1 = linspace(0,(length(ArduinomV1)-1),length(ArduinomV1));
time1 = t1';

t2 = linspace(0,(length(ArmV2)-1),length(ArmV2));
time2 = t2';
t3 = linspace(0,(length(ArmV3)-1),length(ArmV3));
time3 = t3';
t4 = linspace(0,(length(ArmV4)-1),length(ArmV4));
time4 = t4';
t5 = linspace(0,(length(ArmV5)-1),length(ArmV5));
time5 = t5';
%% Plot Force versus Time
figure
plot (time1, Force1)
hold on
xlabel ('Time (ms)')
ylabel ('Force (N)')
title ('Force vs. Time')
hold off

% Plot force versus time for all runs
figure
hold on
plot (time1, Force1);
plot (time2, F2);
plot (time3, F3);
plot (time4, F4);
plot (time5, F5);
xlabel ('Time (ms)')
ylabel ('Force (N)')
title ('Force vs. Time for all 5 Runs')
hold off

%% Create vector of each Screw setting

ScrewTurn1 = ones (200,1);
ScrewTurn2 = repmat(2,200,1);
ScrewTurn3 = repmat(3,200,1);
ScrewTurn4 = repmat(4,200,1);
ScrewTurn5 = repmat(5,200,1);
ScrewTurn6 = repmat(6,200,1);
ScrewTurn7 = repmat(7,200,1);
ScrewTurn8 = repmat(8,60,1);

ScrewTurn =

```

```
[ScrewTurn1;ScrewTurn2;ScrewTurn3;ScrewTurn4;ScrewTurn5;ScrewTurn6;ScrewTurn7;ScrewTurn8];
```

```
%% Create vector of Force when stopped at each setting only
```

```
% for run 1
```

```
ForceHold1 = Force1(1:200);  
ForceHold2 = Force1(400:599);  
ForceHold3 = Force1(800:999);  
ForceHold4 = Force1(1200:1399);  
ForceHold5 = Force1(1550:1749);  
ForceHold6 = Force1(1900:2099);  
ForceHold7 = Force1(2400:2599);  
ForceHold8 = Force1(2850:2909);
```

```
ForceHoldr1 =
```

```
[ForceHold1;ForceHold2;ForceHold3;ForceHold4;ForceHold5;ForceHold6;ForceHold7;ForceHold8];
```

```
% for run 2
```

```
FH1_r2 = F2(1:200);  
FH2_r2 = F2(300:499);  
FH3_r2 = F2(600:799);  
FH4_r2 = F2(900:1099);  
FH5_r2 = F2(1350:1549);  
FH6_r2 = F2(1700:1899);  
FH7_r2 = F2(2080:2279);  
FH8_r2 = F2(2430:2489);
```

```
FH_r2 = [FH1_r2;FH2_r2;FH3_r2;FH4_r2;FH5_r2;FH6_r2;FH7_r2;FH8_r2];
```

```
% for run 3
```

```
FH1_r3 = F3(1:200);  
FH2_r3 = F3(260:459);  
FH3_r3 = F3(520:719);  
FH4_r3 = F3(800:999);  
FH5_r3 = F3(1150:1349);  
FH6_r3 = F3(1750:1949);  
FH7_r3 = F3(2100:2299);  
FH8_r3 = F3(2450:2509);
```

```
FH_r3 = [FH1_r3;FH2_r3;FH3_r3;FH4_r3;FH5_r3;FH6_r3;FH7_r3;FH8_r3];
```

```
% for run 4
```

```
FH1_r4 = F4(1:200);  
FH2_r4 = F4(300:499);  
FH3_r4 = F4(600:799);  
FH4_r4 = F4(900:1099);  
FH5_r4 = F4(1200:1399);  
FH6_r4 = F4(1550:1749);
```

```

FH7_r4 = F4(1900:2099);
FH8_r4 = F4(2230:2289);

FH_r4 = [FH1_r4;FH2_r4;FH3_r4;FH4_r4;FH5_r4;FH6_r4;FH7_r4;FH8_r4];

% for run 5
FH1_r5 = F5(1:200);
FH2_r5 = F5(300:499);
FH3_r5 = F5(600:799);
FH4_r5 = F5(950:1149);
FH5_r5 = F5(1250:1449);
FH6_r5 = F5(1600:1799);
FH7_r5 = F5(1950:2149);
FH8_r5 = F5(2300:2359);

FH_r5 = [FH1_r5;FH2_r5;FH3_r5;FH4_r5;FH5_r5;FH6_r5;FH7_r5;FH8_r5];

%% PLOT Force at each Screw setting

figure
hold on
plot(ScrewTurn, ForceHoldr1);
xlabel('Screw Turn');
ylabel ('Force(N)');
title ('Screw Setting versus Force')
hold off
figure
scatter(ScrewTurn, ForceHoldr1);
xlabel('Screw Turn');
ylabel ('Force(N)');
title ('Screw Setting versus Force')

% plot all 5 runs

figure
hold on
plot (ScrewTurn, ForceHoldr1,'b');
plot (ScrewTurn, FH_r2,'r');
plot (ScrewTurn, FH_r3,'m');
plot (ScrewTurn, FH_r4,'c');
plot (ScrewTurn, FH_r5,'k');
xlabel('Screw Turn');
ylabel ('Force(N)');
title ('Screw Setting versus Force for all 5 Runs')
legend ('Run 1', 'Run 2', 'Run 3', 'Run 4', 'Run5');
hold off

figure
hold on
scatter(ScrewTurn, ForceHoldr1,'b');
scatter (ScrewTurn, FH_r2,'r');

```

```

scatter (ScrewTurn, FH_r3,'m');
scatter (ScrewTurn, FH_r4,'c');
scatter (ScrewTurn, FH_r5,'k');
xlabel('Screw Turn');
ylabel ('Force(N)');
title ('Screw Setting versus Force for all 5 Runs')
legend ('Run 1', 'Run 2', 'Run 3', 'Run 4', 'Run5');
hold off

%% Find ave force at each screw setting and plot scatterplot, and trendline

AveFcolr1 =[mean(ForceHold1);mean(ForceHold2);mean(ForceHold3)

mean(ForceHold4);mean(ForceHold5);mean(ForceHold6);mean(ForceHold7);mean(ForceHold8
)];
AveFr1 = AveFcolr1';
ScrewSet = [1:8];

figure
hold on
plot(ScrewSet,AveFr1, '*');
xlabel('Screw Setting');
ylabel('Average Force');
title('Ave Force at each Screw setting');
hold off

% Linear trendline does not fit
%run1line = polyfit(ScrewSet, AveFr1,1);
%plot(run1line(1)*ScrewSet + run1line(2));

% Find average force for each run

AveFcolr2 =
[mean(FH1_r2);mean(FH2_r2);mean(FH3_r2);mean(FH4_r2);mean(FH5_r2);mean(FH6_r2);me
an(FH7_r2);mean(FH8_r2)];
AveFr2 = AveFcolr2';

AveFcolr3 =
[mean(FH1_r3);mean(FH2_r3);mean(FH3_r3);mean(FH4_r3);mean(FH5_r3);mean(FH6_r3);me
an(FH7_r3);mean(FH8_r3)];
AveFr3 = AveFcolr3';

AveFcolr4 =
[mean(FH1_r4);mean(FH2_r4);mean(FH3_r4);mean(FH4_r4);mean(FH5_r4);mean(FH6_r4);me
an(FH7_r4);mean(FH8_r4)];
AveFr4 = AveFcolr4';

AveFcolr5 =
[mean(FH1_r5);mean(FH2_r5);mean(FH3_r5);mean(FH4_r5);mean(FH5_r5);mean(FH6_r5);me

```



```

an(FH7_r5);mean(FH8_r5)];
AveFr5 = AveFcolr5';

% plot screw setting versus average force for each ru

figure
hold on
plot(ScrewSet,AveFr1,'*b');
plot(ScrewSet,AveFr2,'*r');
plot(ScrewSet,AveFr3,'*m');
plot(ScrewSet,AveFr4,'*c');
plot(ScrewSet,AveFr5,'*k');
xlabel('Screw Setting');
ylabel('Average Force');
title('Ave Force at each Screw setting for all 5 Runs');
legend ('Run 1', 'Run 2', 'Run 3', 'Run 4', 'Run5');
hold off

%% Curve fitting
cf_r1_ave = cftool(ScrewSet, AveFr1);
cf_r2_ave =cftool(ScrewSet, AveFr2);
cf_r3_ave =cftool(ScrewSet, AveFr3);
cf_r4_ave =cftool(ScrewSet, AveFr4);
cf_r5_ave =cftool(ScrewSet, AveFr5);

cf_r1 = cftool(ScrewTurn, ForceHoldr1);
cf_r2 =cftool(ScrewTurn, FH_r2);
cf_r3 =cftool(ScrewTurn, FH_r3);
cf_r4 =cftool(ScrewTurn, FH_r4);
cf_r5 =cftool(ScrewTurn, FH_r5);

%% Plot by degrees and distance downward

deg = [0;15;30;45;60;75;90;105];

figure
hold on
plot(deg,AveFr1,'*b');
plot(deg,AveFr2,'*r');
plot(deg,AveFr3,'*m');
plot(deg,AveFr4,'*c');
plot(deg,AveFr5,'*k');
xlabel('Degrees of Turn');
ylabel('Average Force');
title('Ave Force vs. Degrees of Turn for all 5 Runs');
legend ('Run 1', 'Run 2', 'Run 3', 'Run 4', 'Run5');
hold off

dist = deg*((1/11)/24);

```

```

figure
hold on
plot(dist,AveFr1,'*b');
plot(dist,AveFr2,'*r');
plot(dist,AveFr3,'*m');
plot(dist,AveFr4,'*c');
plot(dist,AveFr5,'*k');
xlabel('Linear Distance Traveled (in)');
ylabel('Average Force');
title('Ave Force vs. Distance traveled Downward for all 5 Runs');
legend ('Run 1', 'Run 2', 'Run 3', 'Run 4', 'Run5');
hold off

```

```

%% Wwithout screw settings 1-4 & for only runs 3-5
short_F_r3 =[FH5_r3; FH6_r3; FH7_r3];
short_F_r4 =[FH5_r4; FH6_r4; FH7_r4];
short_F_r5 =[FH5_r5; FH6_r5; FH7_r5];

```

```

short_screwset = [ScrewTurn5;ScrewTurn6;ScrewTurn7];

```

```

figure
hold on
plot(short_screwset, short_F_r3,'*m')
plot(short_screwset, short_F_r4,'*c')
plot(short_screwset, short_F_r5,'*k')
xlabel('Screw Setting');
ylabel('Average Force');
title('Force at each Screw Setting for 3 Runs');
legend ('Run 3', 'Run 4', 'Run5');
hold off

```

```

%% combined

```

```

short_F_r345 =[FH5_r3; FH6_r3; FH7_r3;FH5_r4; FH6_r4; FH7_r4;FH5_r5; FH6_r5;
FH7_r5];

```

```

short_screwset_comb = [short_screwset;short_screwset;short_screwset;];
Screw_short = [5;6;7];

```

```

figure
hold on
plot(short_screwset_comb, short_F_r345,'*')
xlabel('Screw Setting');
ylabel('Average Force (N)');
title('Force at each Screw Setting');

```

```

trencline = polyfit(short_screwset_comb, short_F_r345,1);
plot (trencline(2)*Screw_short+trencline(1),Screw_short )

```

```

cftool(short_screwset_comb, short_F_r345);

```

O. Pressure Sensitive Film Testing

Goal: The goal of this test is to assess the pressure that will be applied to a patient's arm surface by the fracture strength measurement device. This will be accomplished by placing team member's arms in the device with film between the arm and any contacting surfaces with the device, applying a specific loading level, and then determining the pressure experienced by the arm at various positions.

Procedure

- 1) *Calibrate film:* Record images, and select reference colors, and corresponding forces.
 - a. Choose a flat object with known surface area
 - b. Calculate the amount of weight needed to increase the pressure on that object by 50 psi increments
 - c. Cut strip of film using a ruler to guide a boxcutter. Cut deeply to cut the film fully in one pass. Avoid pressing on the ruler to avoid activating the film.
 - d. Place object gently on film.
 - e. Gently place first weight increment on object, being careful not to contact the film elsewhere. Allow weight to sit for 30 seconds
 - f. Remove weight and object gently
 - g. Record position of each calibration spot and the corresponding pressure
 - h. Repeat, but add the number of weight increments needed for each successive measure, choosing a separate spot on the film to place each trial's object
 - i. When testing is finished, as soon as possible, scotch tape all trials, with handwritten identifying label, onto a single piece of white paper with the calibration portion on the same sheet. Scan and photocopy this paper in COLOR at the HIGHEST DPI RESOLUTION available so as not to lose data to degradation
 - j. Avoid wrinkling the paper, folding, vibrations, accidental touches, recutting. Keep in a cool dry place away from light and vibrations and air.
 - k. During later force application, allow loading to sit for 30 seconds, the same time as the calibration, as well.

2) *Apply the padding:* Apply padding to device around contact surface of the loading region.

3) *Tape the pressure point:* Tape the pressure point to the top of the loading device

- Apply foam padding over pressure point

4) *Apply the film:* Apply the film to the distal and proximal regions of inside of the wrist where they will contact the edges of the bottom of loading device using scotch tape.

- Apply film to region on back of wrist where pressure point will be applied

5) *Take photographs:* Photograph the film positions with a scale bar

6) *Arm insertion:* Gently insert the arm into test fixture

7) *Tighten the test fixture:* tighten down test fixture until visual contact of pressure point is observed with the top of the wrist

Loading levels in terms of complete force exerted by device will be 50 N intervals starting with 0 N increasing to pain rating of 5 or 450 N, whichever comes first.

8) *Tighten the loading device:* Tighten the loading device to first force measurement interval

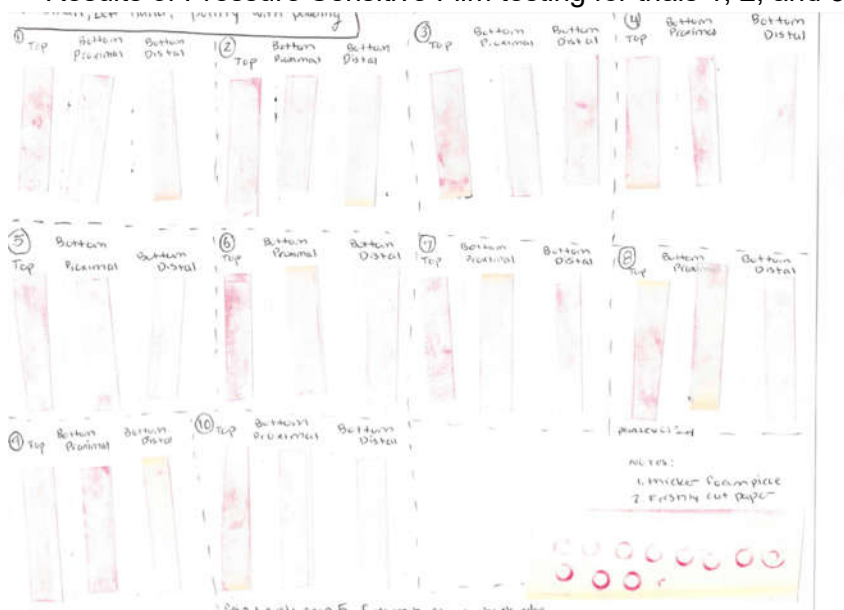
- Apply static force for 30 seconds
- Unload arm

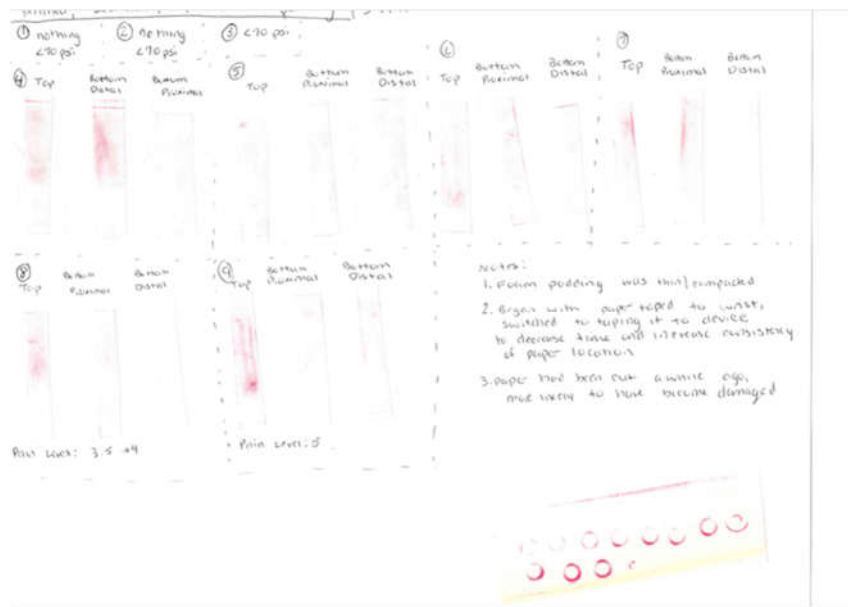
9) *Record pressure color:* Remove arm, without removing film from arm, photograph film with color reference, record pressure color

10) *Repeat procedures 6-9:* Replace arm in device, load to next force level, repeat above

P. Results of Pressure Sensitive Film Testing

Results of Pressure Sensitive Film testing for trials 1, 2, and 3, respectively.

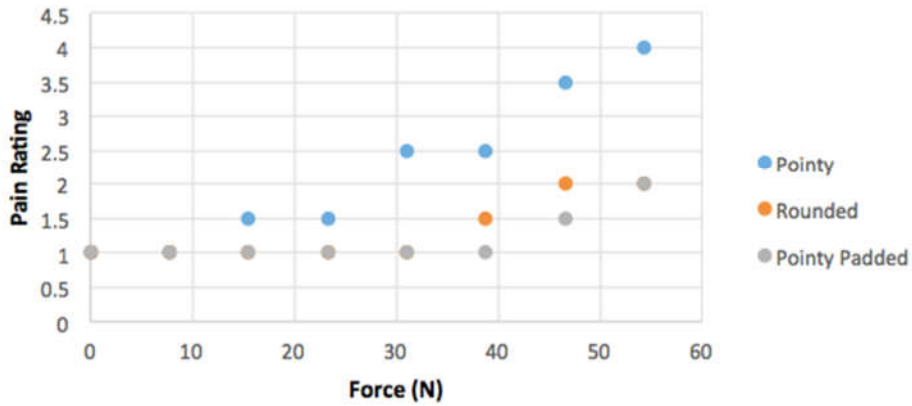




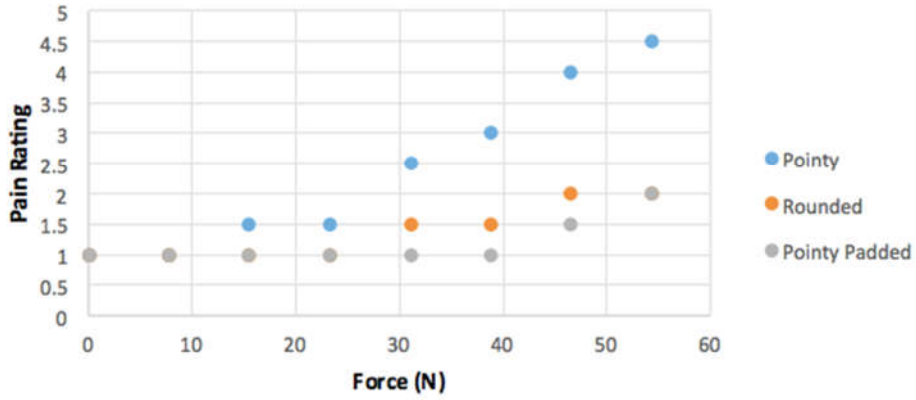
Q. Results of Comfort Testing with the Bending Design

Results of comfort testing performed on each member of the team.

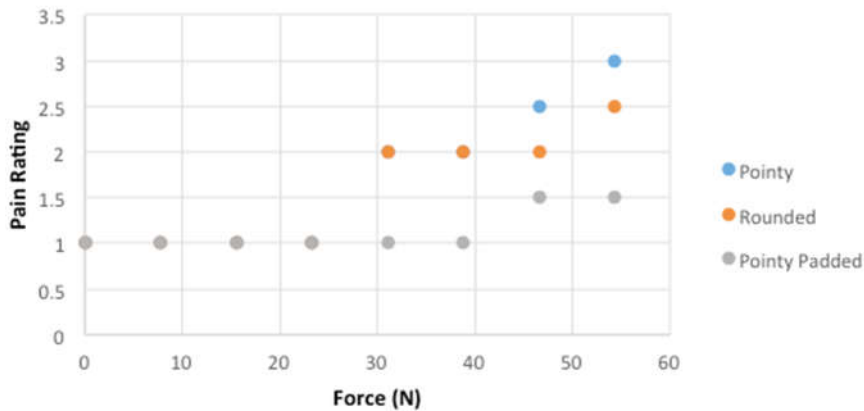
Pain Rating at Various Forces for Ahmed



Pain Rating at Various Forces for Jennifer



Pain Rating at Various Forces for Hannah



R. Bill of Materials for the Updated Bending Design Prototype

Item	Cost (\$)	Count
Onyx Filament	94.5	2 spools
Glass Fiber Reinforcement	200	As needed
Threaded 1/2"-20 steel rod	6	2 X 1 feet
1/2" delrin rod	1.51	2 ft
Brass nuts	5.41	5 pack
Hook and loop straps	7.48	NA
Fishing line	3.00	NA
Foam	0.99	2 sheets
Assorted screws and washers, lab supplies	0	NA
Total	421.89	NA

S. Strain Gauge and instrumentation Setup and Use

Materials:

Strain gauge
Signal conditioning unit
Scotch tape
Soldering supplies
Wire- 3 strand, individually insulated
Super glue

Rod preparation:

Machine a flat surface on the threaded rod that is at least $\frac{3}{4}$ " long and $\frac{3}{8}$ " wide, with the long region parallel to the long axis of the rod
Clean flat region with acetone
Apply scotch tape to the exposed metal side of the strain gauge
Lay tape and strain gauge down on flat, clean, rod region
Pull tape up partially, place drop of superglue on rod
Press gauge and tape down spreading the glue fully under the gauge
Allow glue to dry for at least 10 minutes
Pull tape up at sharp angle slowly to make sure gauge doesn't pull up, remove tape fully if glue has set

Take tricolor wire and separate wires at ends. Strip wire ends
On one end solder white and black wires together. Tinn all wire ends with solder.
Apply small solder spots to contacts of strain gauge

Tape wire to rod

Solder connected wire ends to gauge contacts: red to one, black and white to the other

Cover gauge and wire ends entirely in hot glue to protect it

Instrumentation setup:

Connect triple separated end of gratin gauge wire to instrumentation bridge

Connect bridge to back of conditioning unit

Connect power cable to back of conditioning unit

Connect power cable to wall outlet

Connect output cable to back of conditioning unit at 10 V output port

Connect output cable to voltmeter

*Instrument should be in quarter bridge setup

Turn on conditioning unit - press power button in

Set gain to 100- press 100 button in under Gain

Turn Excitation on - put switch in on position (up)

Set Excitation knob to 10

Set trim to point up

Set Gain to 1.9

Tune Conditioner:

* Allow unit to warm up for 15 minutes. Until this time readings will be unstable

Under Auto Bal st switch to reset, then to on

Wait for lights under output to go on and then off

Under CAL hold A in up position - this replaces the strain gauge with a shunt resistor of 100 ohm nominal resistance

Look at voltmeter. Set voltmeter to 2000mV setting

Adjust Gain knob until voltmeter reads 0000

Perform finest adjustments with trim knob

Verify gauge function by loading the rod and looking for response on voltmeter: positive in tension, negative in compression.

*under this setup, 1 V = 1000 micro strains. Gauge is intended for steel.

Signal Acquisition:

Arduino code has been altered to output two readings as of 3/25/17

Connect red from signal output to A1 port on arduino, and black to ground

In serial output monitor on Arduino, strain gauge readings are in second column, after the comma.

Calibration:**Verification:**

Perform tensile and compressive testing on arduino

Generate calibration curves and equation -- preliminary data indicates device is linear

Validation:

Perform testing for button load cell in mechanism calibration, calibrate strain gauge to force through button load cell calibration.

T. Engineering Drawings of Device and Components

6

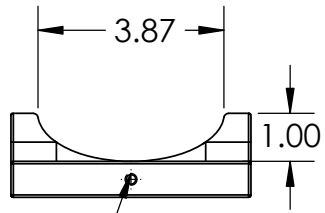
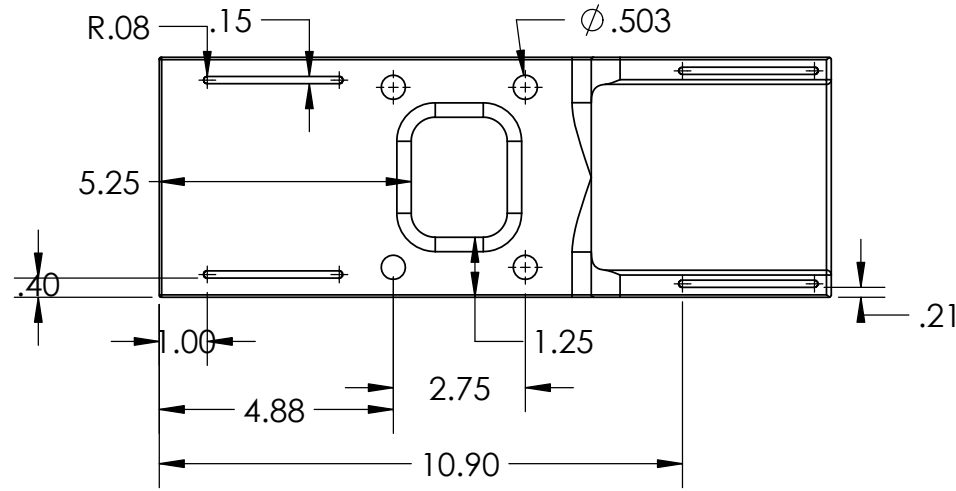
5

4

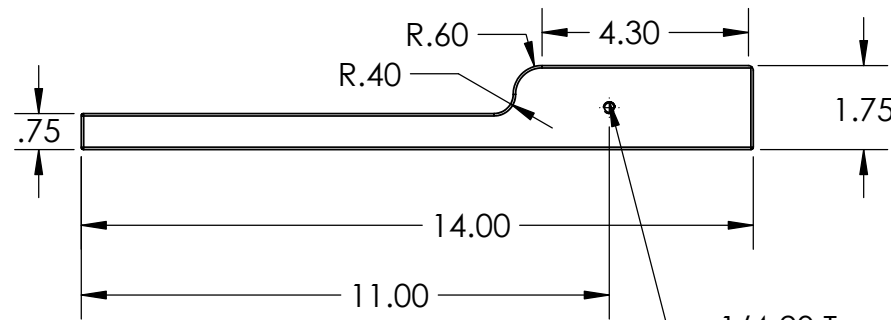
3

2

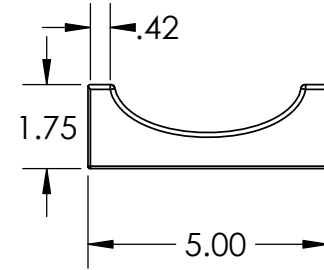
1



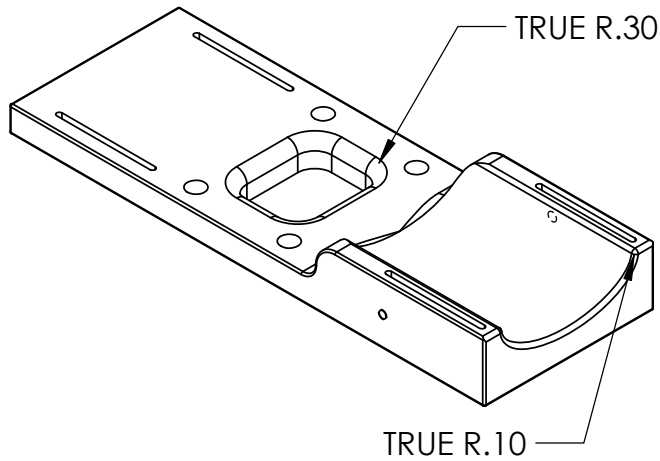
1/4-20 Tapped Hole



1/4-20 Tapped Hole



ISOMETRIC VIEW



UNLESS OTHERWISE SPECIFIED: DIMENSIONS ARE IN INCHES SURFACE FINISH: TOLERANCES: LINEAR: ANGULAR:		FINISH:		DEBURR AND BREAK SHARP EDGES		DO NOT SCALE DRAWING		REVISION	
						All fillets 0.5 unless otherwise specified			
						TITLE: Complete base			
						DWG NO. 3		A4	
						SCALE:1:4		SHEET 1 OF 1	

6

5

4

3

2

1

6

5

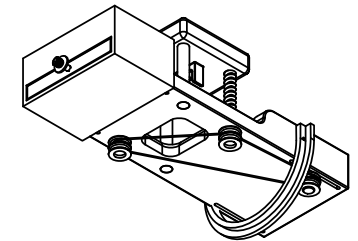
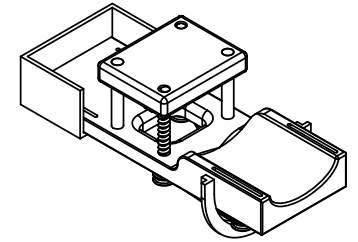
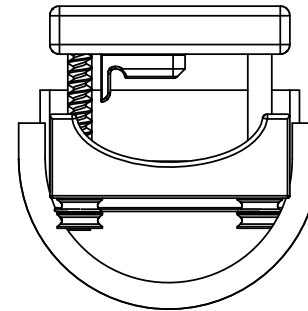
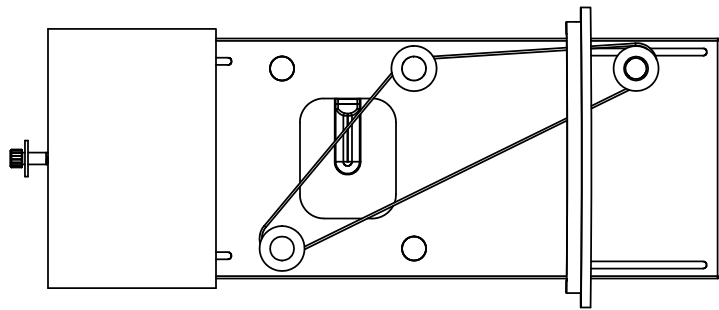
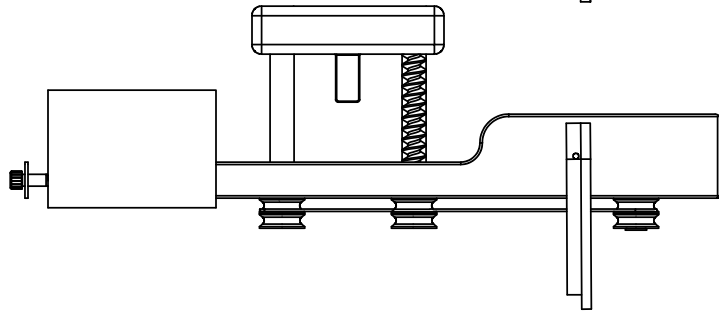
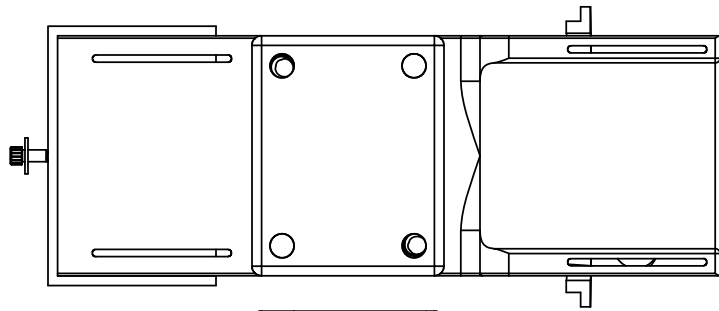
4

3

2

1

Isometric top and bottom views



SCALE 1 : 8

UNLESS OTHERWISE SPECIFIED: DIMENSIONS ARE IN INCHES SURFACE FINISH: NATURAL TOLERANCES: LINEAR: +/- 0.01 ANGULAR: +/- 1 DEG				DEBURR AND BREAK SHARP EDGES		DO NOT SCALE DRAWING		REVISION: INITIAL RELEASE					
						TITLE: Fracture Measurement Device Assembly							
DRAWN		NAME		SIGNATURE						DATE			
CHK'D										4/24/17			
APPV'D													
MFG													
Q.A								MATERIAL: SEE COMPONENTS					
						DWG NO.		1					
						SCALE:1:4		SHEET 1 OF 1					
								A4					

6

5

4

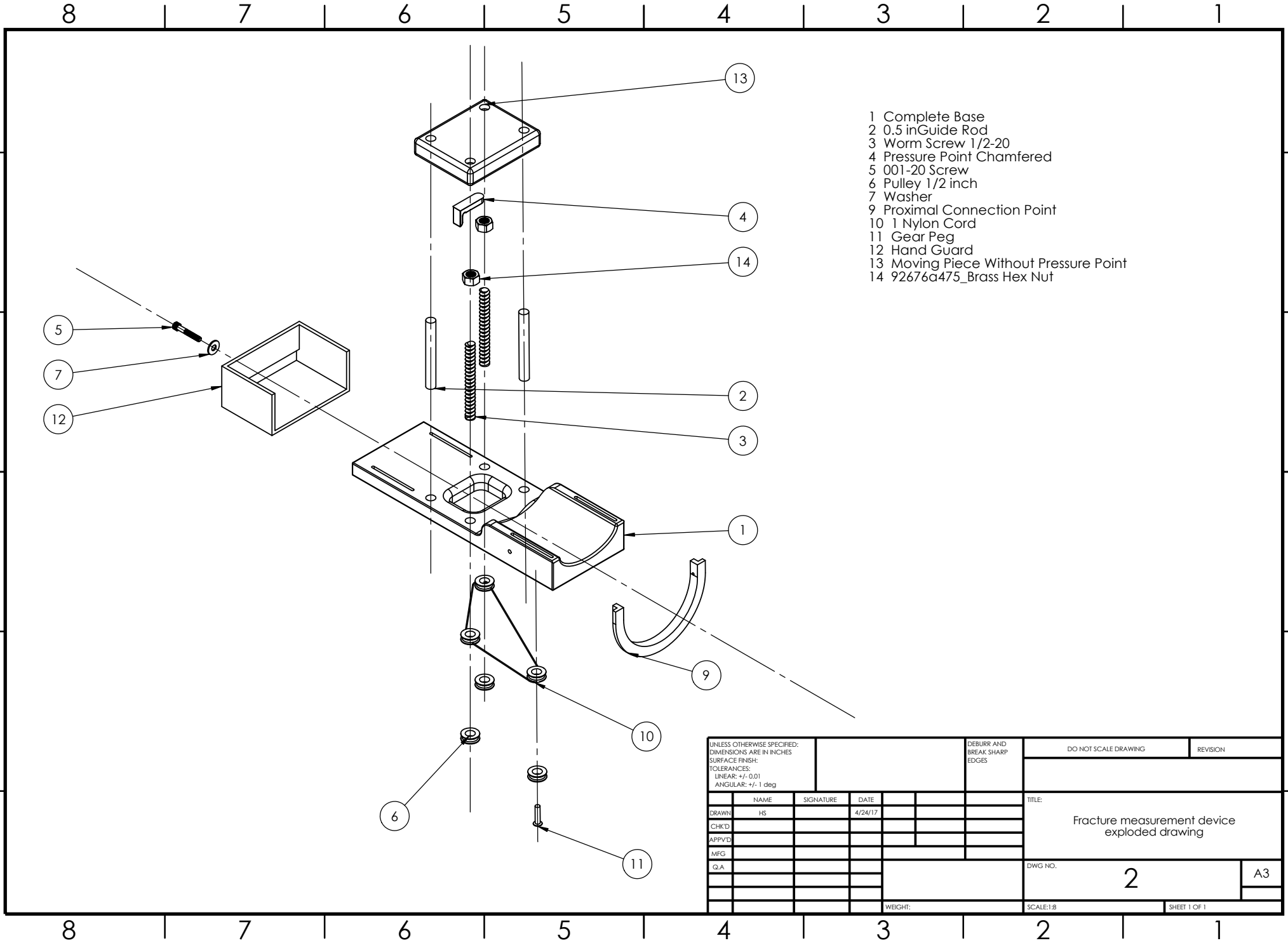
3

2

1

- 1 Complete Base
- 2 0.5 in Guide Rod
- 3 Worm Screw 1/2-20
- 4 Pressure Point Chamfered
- 5 001-20 Screw
- 6 Pulley 1/2 inch
- 7 Washer
- 9 Proximal Connection Point
- 10 1 Nylon Cord
- 11 Gear Peg
- 12 Hand Guard
- 13 Moving Piece Without Pressure Point
- 14 92676a475_Brass Hex Nut

UNLESS OTHERWISE SPECIFIED: DIMENSIONS ARE IN INCHES SURFACE FINISH: TOLERANCES: LINEAR: +/- 0.01 ANGULAR: +/- 1 deg			DEBURR AND BREAK SHARP EDGES		DO NOT SCALE DRAWING		REVISION	
DRAWN: HS			SIGNATURE:		DATE: 4/24/17		TITLE: Fracture measurement device exploded drawing	
CHK'D:			MFG:		G.A.:		DWG NO. 2	
WEIGHT:			SCALE: 1:8		SHEET 1 OF 1			



6

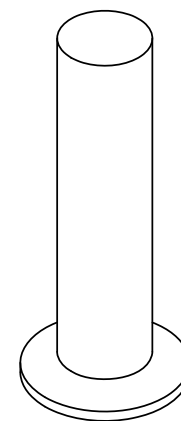
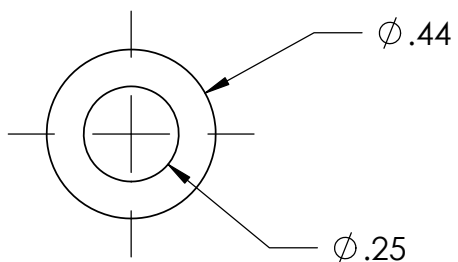
5

4

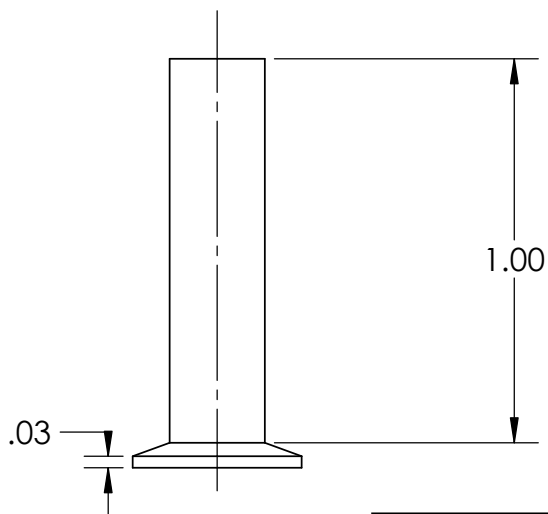
3

2

1



ISOMETRIC VIEW



UNLESS OTHERWISE SPECIFIED: DIMENSIONS ARE IN INCHES SURFACE FINISH: TOLERANCES: LINEAR: ANGULAR:			FINISH:		DEBURR AND BREAK SHARP EDGES		DO NOT SCALE DRAWING		REVISION		
							TITLE: <h1>gear peg</h1>				
	NAME	SIGNATURE	DATE								
DRAWN	JG		4/24/2017								
CHK'D											
APPV'D											
MFG							DWG NO.		8		
Q.A				MATERIAL:				A4			
							WEIGHT:		SCALE:2:1		
									SHEET 1 OF 1		

6

5

4

3

2

1

6

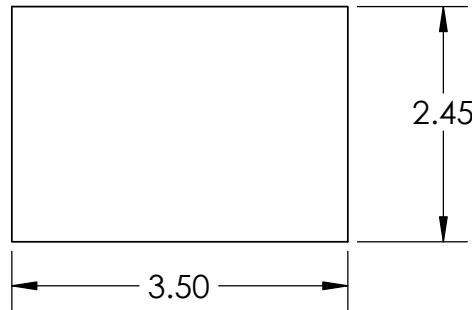
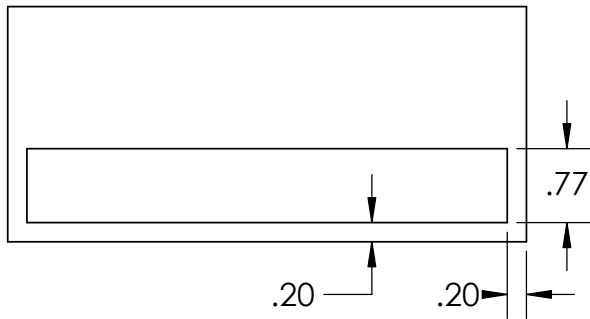
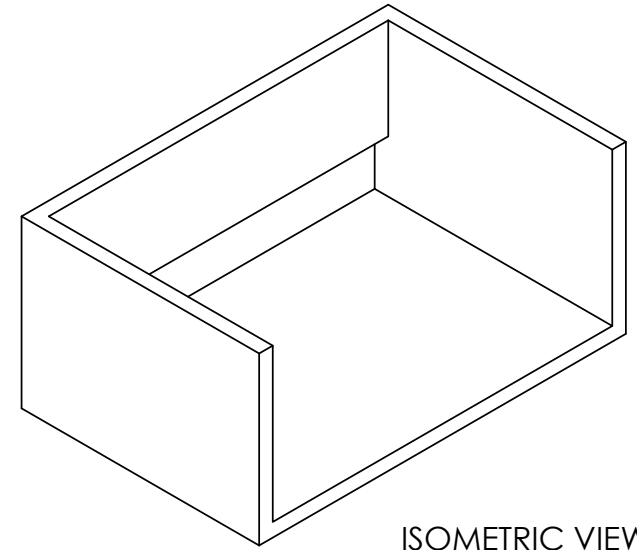
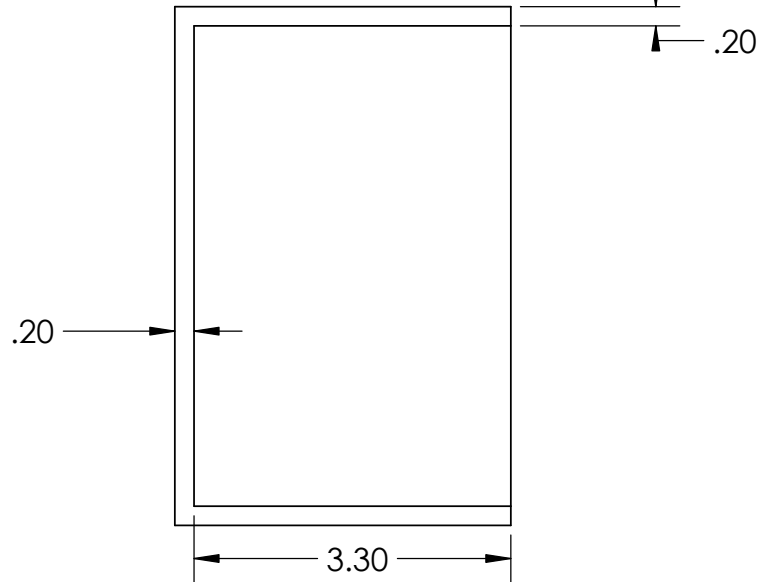
5

4

3

2

1



UNLESS OTHERWISE SPECIFIED: DIMENSIONS ARE IN INCHES SURFACE FINISH: TOLERANCES: LINEAR: ANGULAR:			FINISH:		DEBURR AND BREAK SHARP EDGES		DO NOT SCALE DRAWING		REVISION						
							TITLE: <h1>hand guard</h1>								
DRAWN	NAME	SIGNATURE	DATE												
CHK'D															
APPV'D															
MFG															
Q.A															
					MATERIAL:		DWG NO.		A4						
							7								
					WEIGHT:		SCALE:1:2		SHEET 1 OF 1						

6

5

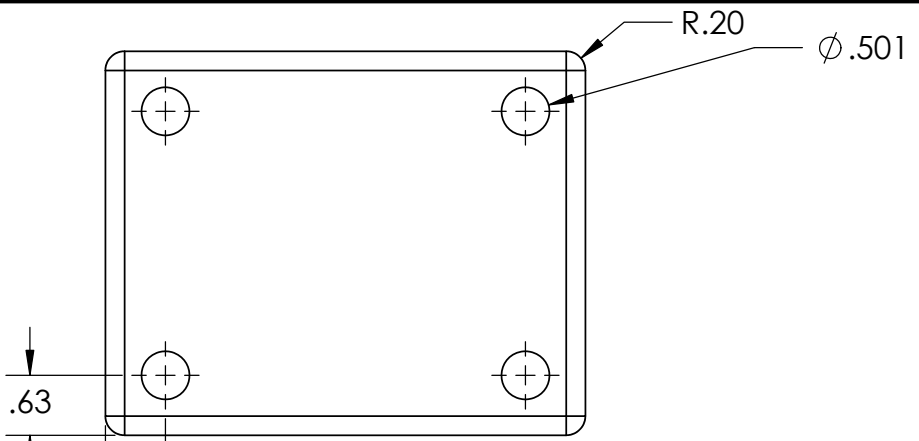
4

3

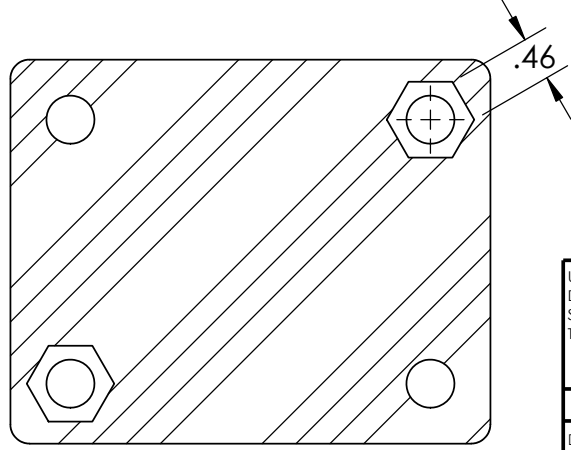
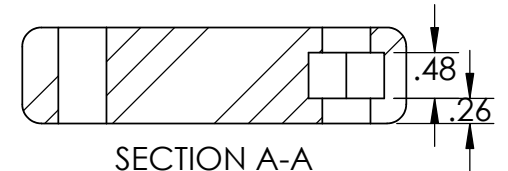
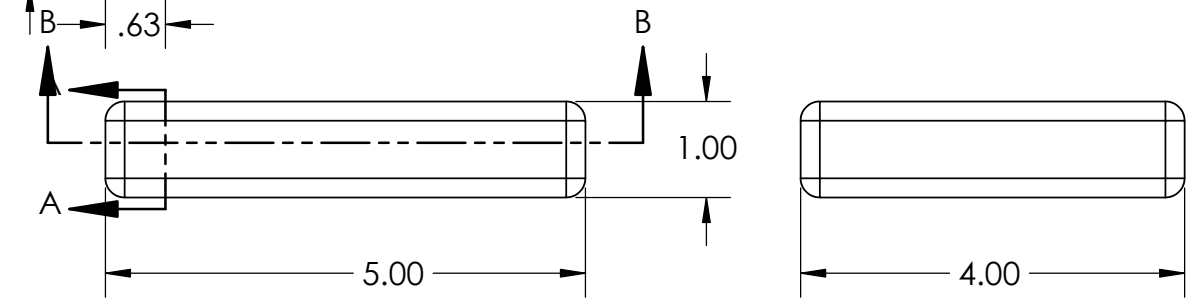
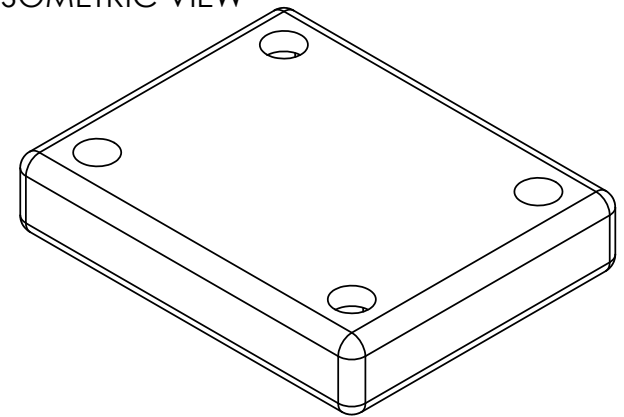
2

1

6 5 4 3 2 1



ISOMETRIC VIEW



SECTION B-B

UNLESS OTHERWISE SPECIFIED: DIMENSIONS ARE IN INCHES SURFACE FINISH: TOLERANCES: LINEAR: ANGULAR:		FINISH:		DEBURR AND BREAK SHARP EDGES		DO NOT SCALE DRAWING		REVISION	
NAME	SIGNATURE	DATE				TITLE: Moving Piece without pressure point			
DRAWN JG		4/24/2017							
CHK'D									
APPV'D									
MFG									
Q.A				MATERIAL:		DWG NO. 4		A4	
				WEIGHT:		SCALE:1:2		SHEET 1 OF 1	

6 5 4 3 2 1

6

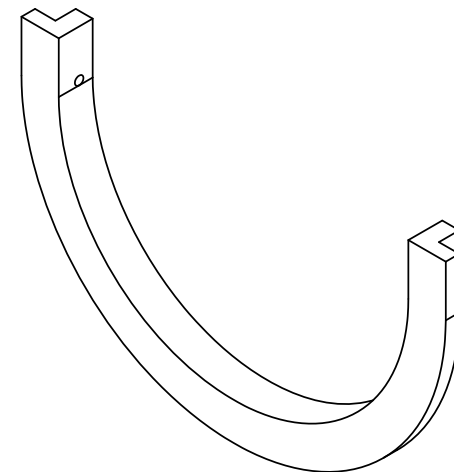
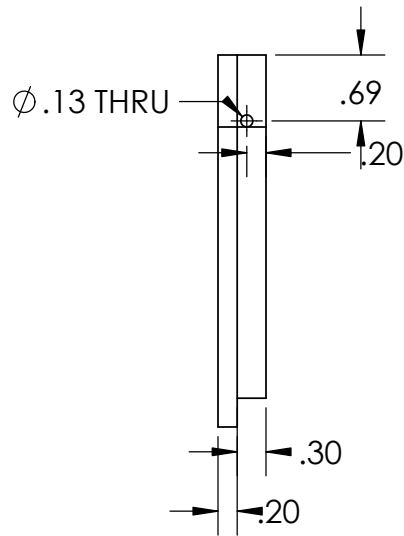
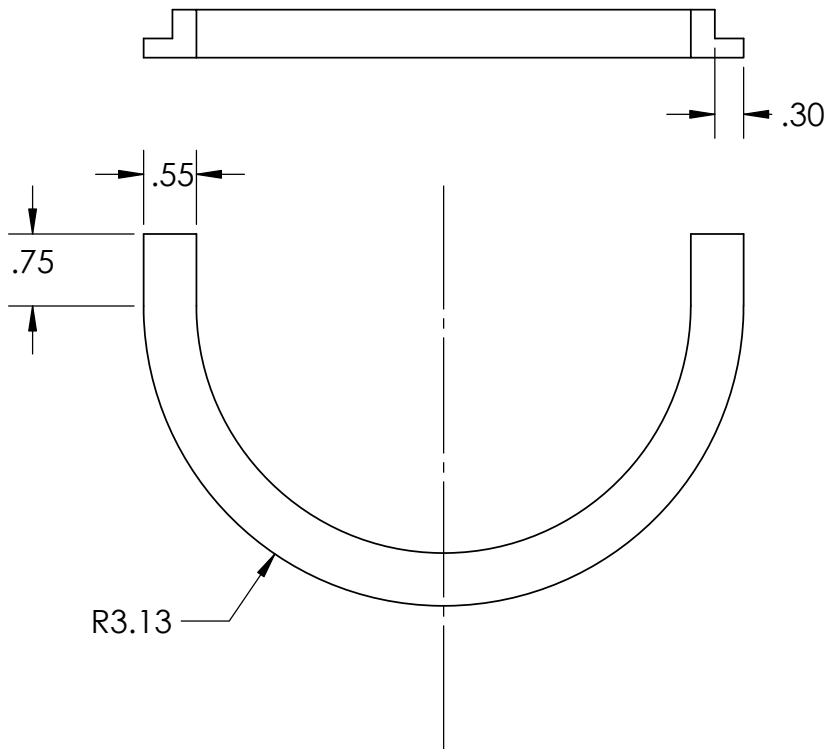
5

4

3

2

1



ISOMETRIC VIEW

UNLESS OTHERWISE SPECIFIED: DIMENSIONS ARE IN INCHES SURFACE FINISH: TOLERANCES: LINEAR: ANGULAR:			FINISH:			DEBURR AND BREAK SHARP EDGES		DO NOT SCALE DRAWING		REVISION	
								TITLE: proximal connection point			
						MATERIAL:		DWG NO. 6		A4	
						WEIGHT:		SCALE:1:2		SHEET 1 OF 1	

6

5

4

3

2

1

6

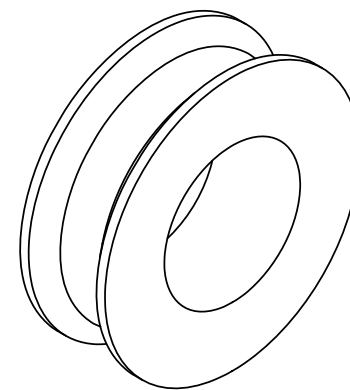
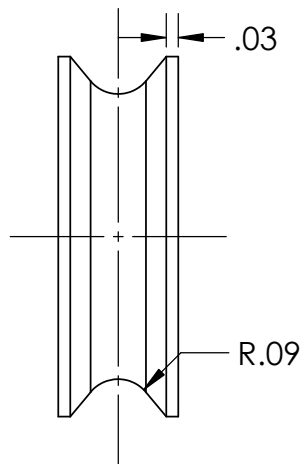
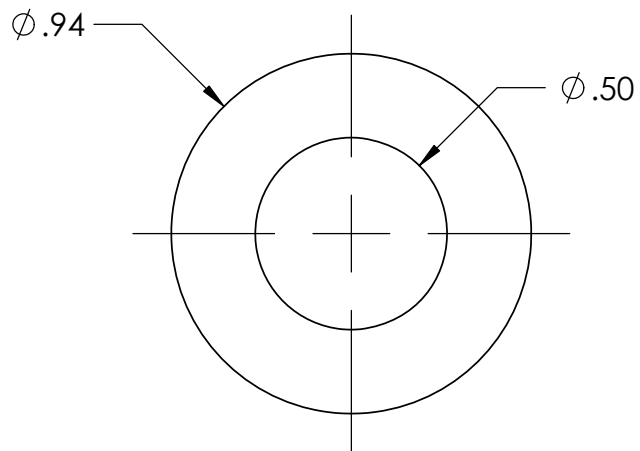
5

4

3

2

1



ISOMETRIC VIEW

UNLESS OTHERWISE SPECIFIED: DIMENSIONS ARE IN INCHES SURFACE FINISH: TOLERANCES: LINEAR: ANGULAR:			FINISH:		DEBURR AND BREAK SHARP EDGES		DO NOT SCALE DRAWING		REVISION		
	NAME	SIGNATURE	DATE				TITLE: Pulley half inch				
DRAWN	JG		4/24/2017				DWG NO. 9				
CHK'D											
APPV'D							A4				
MFG											
Q.A					MATERIAL:		SCALE:2:1				
					WEIGHT:		SHEET 1 OF 1				

6

5

4

3

2

1